UNIVERSITY COLLEGE LONDON

New laboratory edge illumination x-ray phase contrast imaging set-ups

---

Gibril Kerefa Nyakeh Kallon

Department of Medical Physics and Biomedical Engineering

December 2016

A thesis submitted for the degree of Doctor of Philosophy

I, Gibril Kallon confirm that the work presented in this thesis is my own. Where information has been derived from other sources, I confirm that this has been indicated in the thesis.

Signature………………………………..

Abstract

Edge illumination (EI) is an X-ray phase contrast imaging technique which has demonstrated its potential for real-world translation. The set-up consists of two periodic masks, which are aligned with each other along the beam axis. The masks are then offset to make the set-up sensitive to X-ray refraction. Despite its promise, some of EI's weaknesses must be addressed before it can be further adapted to real-world applications. For example, mask alignment conditions can be further relaxed by using a much more simplified set-up. Additionally, the current set-up must be made sensitive to refraction along two directions simultaneously, in order to match the sensitivity of the current attenuation-based X-ray imaging methods.

This thesis describes the most recent developments to the EI method which aim to tackle the aforementioned issues. To achieve this, three separate experiments have been performed.

The first was a study of the factors affecting EI refraction sensitivity. A flexible phase retrieval algorithm was first introduced, and was shown to produce quantitatively accurate results. This was also used to study the system's sensitivity under various conditions.

Next, a single-mask EI set-up was built in the laboratory and was modelled using a wave optics computer simulation. This was then used to study the sensitivity of the single-mask method and extrapolate its value for different set-ups, while benchmarking it against the "standard" double-mask EI set-up.

Finally, a two-directionally sensitive set-up is implemented in the laboratory using a novel mask design. A separate Monte Carlo simulation was used to study the alignment of the set-up, and a new, “two-directional” phase retrieval algorithm was developed.

In the future, these developments can be combined into a single optimised EI set-up, which shares the cumulative benefits from all the aspects of the research undertaken here.

Acknowledgements

I would first and foremost like to thank Professor Alessandro Olivo for providing me with the opportunity to undertake this exciting Ph.D. project. His infectious enthusiasm, immense knowledge, patience and sense of humour have been invaluable to me at every turn; and in particular while writing this thesis.

In a similar vein, I also wish to thank my second supervisor, Dr. Paul C. Diemoz, for his continued advice and careful attention to detail. In the lab, I am particularly grateful to Dr. Marco Endrizzi for familiarizing me with the plethora of motors and detectors that I would use extensively during the course of my work, and for always being available to discuss ideas. Likewise, special thanks can also be given to Dr. Fabio A. Vittoria and Dr. Thomas P. Millard, firstly for introducing me to their computer models, and then for our numerous stimulating discussions.

I have been very fortunate to work alongside a number of friendly scientists within the Department of Medical Physics and Biomedical Engineering at UCL. Indeed, there have been too many to name individually, however, my fellow PhD students within the Advanced X-ray Imaging group, Anna Zamir-Fordham and Dario Basta deserve a special mention, along with Chiaki Crews and Anna Nikopoulou. We have shared our momentary disappointments, roaring successes and of course, basketball.

From the bottom of my heart, I would also like to thank my Muslim brothers at UCL, past and present, who made me feel at home when I was lost, introduced me to the joys of Charity Week and for teaching me how to smile when times were darkest. With equal sincerity, I extend this same gratitude to my closest friends, David Johnson, Andrew Tamara and Amahl McLaughlin for enduring my long absences, and for always being there when I eventually returned. I am also extremely grateful, once more, to Dr. Fabio Vittoria, for his warmth and friendship, and for sharing with me his culture. I am similarly grateful to his wife, Mariele, and to their families, who made me feel like a native in Modugno, despite my feeble attempts at speaking Italian. In addition, I would like to thank the McNally family for their kindness, and for providing me with many dead insect samples, one of which was studied in this thesis.

This work would not be possible without the love and support of my family. Although my aunts, uncles and cousins are too numerous to mention individually, I hope we can all agree that Foday Jalloh and Uncle Mohammed Wurie Jalloh deserve special praise for being there in the early years, and my Uncles, Dr. Abdul Rahim, Alusine and Alhassan Jalloh for being there in the latter, with sage wisdom and the most uplifting words. I would also like to thank Modi Mouctar for his words of encouragement, and I must not forget Aunty Hassatu and Uncle Abdul Kamara, who introduced me to this beautiful city of London, and their children Ahmed and Amidu Kamara, who are my pillars of joy.

My greatest appreciations, love and respect are reserved for my mother and father, Neneh and Baaba. Their love and support for me during these many years of study can never be repaid in words or deeds.

Lastly, I would like to thank God for giving me the strength to endure the trying times, and the peace to appreciate the better ones, and for surrounding me with the best people from all over the world, who have walked alongside me on this path, from Sierra Leone to the UK.

Contents

List of publications

D.Basta, M. Endrizzi, F. A. Vittoria, **G. K. N. Kallon**, T. P. Millard, P. C. Diemoz, A. Olivo, Note: Design and realization of a portable edge illumination X-ray phase contrast imaging system, 2015, *Review of Scientific Instruments*, 86(9).

M. Endrizzi, F.A. Vittoria, **G. Kallon**, D. Basta, P.C. Diemoz, A. Vincenzi, P. Delogu, R. Bellazzini, A. Olivo, Achromatic approach to phase-based multi-modal imaging with conventional X-ray sources, 2015, *Optics Express*, 23(12), p.16473.

F.A. Vittoria, **G.K.N. Kallon**, D. Basta, P.C. Diemoz, I.K. Robinson, A. Olivo, M. Endrizzi, Beam tracking approach for single-shot retrieval of absorption, refraction, and dark-field signals with laboratory x-ray sources, 2015, *Applied Physics Letters*, 106(22), p.224102.

G. K. Kallon, M. Wesolowski, F. A. Vittoria, M. Endrizzi, D. Basta, T. P. Millard, P.C. Diemoz, and A. Olivo. A laboratory based edge-illumination x-ray phase-contrast imaging setup with two-directional sensitivity, 2015, *Applied Physics Letters*, 107(20),

A. Astolfo, M. Endrizzi, **G. Kallon**, T. Millard, F.A. Vittoria, & A. Olivo, A first investigation of accuracy, precision and sensitivity of phase-based x-ray dark-field imaging, (2016) Journal of Physics D: Applied Physics, 49 (48), 485501-1-485501-7.

G.K. Kallon, P.C. Diemoz, F.A. Vittoria, D.Basta, M.Endrizzi, A. Olivo, Comparing signal intensity and refraction sensitivity of double and single mask edge illumination x-ray phase contrast imaging.*(in preparation)*

Conference papers

P. C. Diemoz, M. Endrizzi, F. A. Vittoria, C. K. Hagen, **G. Kallon**, D. Basta, M. Marenzana, P. Delogu, A. Vincenzi, L. De Ruvo, G. Spandre, A. Brez, R. Bellazzini, A. Olivo, Laboratory implementation of edge illumination X-ray phase-contrast imaging with energy-resolved detectors", *Proc. SPIE 9412, Medical Imaging 2015: Physics of Medical Imaging*.

M. Endrizzi , F.A. Vittoria, P.C. Diemoz, **G.K. Kallon**, D. Basta, A. Zamir A, C.K. Hagen, U.H. Wagner, C. Rau, I.K. Robinson, A. Olivo, Simple and robust synchrotron and laboratory solutions for high-resolution multimodal X-ray phase-based imaging. X-Ray Microscopy Conference 2016, Oxford UK, 15th to 19th August 2016. *PROCEEDING: Journal of Physics: Conference Series (JPCS)* under review

List of figures

List of abbreviations

ABI-	Analyser based imaging
A-Se-	Amorphous Selenium
DPI-	Differential Phase Imaging
EI-	Edge Illumination
EM-	Electromagnetic
ERF-	edge response function
FSP-	Free space propagation
FWHM-	Full Width Half Maximum
GI-	Grating Interferometry
IC-	Illumination curve
IPF-	Illuminated pixel fraction
LSF-	Line spread function
PSF-	Point spread function
RC-	Rocking Curve
ROI-	Region of Interest
SM-EI-	Single-mask Edge Illumination
SPR-	Scatter-to-Primary Ratio
USAXS-	Ultra-small angle X-ray Scattering
XPCI-	X-ray phase contrast imaging

بسم الله الرحمن الرحيم

“In the name of God, the beneficent, the Merciful,”

Thesis Outline

In the first chapter, the discovery of X-rays and the physical interactions which govern conventional attenuation-based imaging will be outlined. This will be followed by a description of the underlying interactions that give rise to phase contrast effects. Finally, numerous benefits of phase contrast signals will also be given, and the motivations for carrying out this work will be explained.

In chapter 2, a literature review of phase contrast imaging techniques will be presented; this will discuss the historical development of several X-ray phase contrast imaging (XPCI) approaches, and eventually introduce the edge illumination (EI) method, which is the focus of this work.

In chapter 3, the materials and methods, such as the source and detectors used in the experimental work, will be described. In addition, two software packages, which are used to model the EI set-up, will be introduced. They are based on a ray-tracing Monte Carlo approach and a wave optics approach, respectively.

In chapter 4, the refraction sensitivity of the EI method will be examined. An algorithm is introduced which can extract the phase contrast signal, and it is shown to produce quantitatively accurate results when tested against simple objects i.e. wires. Images are then acquired of a biological sample to evaluate the practical significance of the sensitivity on the level of image detail that can be detected.

In chapter 5, one of the masks of the edge illumination set-up will be removed, thereby constructing a more simplified single-mask set-up. The resulting relationship between the pixel point spread function and the refraction sensitivity will be examined. In addition, simulations will be performed in order to study the changes in sensitivity, which occur as a result of this new design. This method will also be shown to be quantitative, though it can be prone to errors if transmission through the mask is not negligible.

In chapter 6, a new edge illumination set-up, which is sensitive to refractions signals along two orthogonal directions simultaneously, will be presented. Monte Carlo simulations are used to demonstrate how two-directional refraction sensitivity may be achieved, as well as to develop mechanisms to simplify the experimental alignment of the masks. Moreover, a novel phase retrieval algorithm is derived specifically for this set-up. It leads to the separation and evaluation of absorption, refraction and other related signals in the vertical and horizontal direction, respectively.

Chapter 1 X-ray interaction with matter

1.1 Overview

In this chapter, the fundamental physical interactions of X-rays with matter, which are relevant to this work, are described. In particular, mechanisms that govern attenuation-based X-ray imaging and its phase contrast counterpart are outlined. Finally, the motivation for imaging with phase sensitive set-ups is briefly discussed. These methods exploit the small deviations experienced by X-rays as they traverse matter to generate new, and often enhanced, sources of contrast. Ultimately, this leads to the production of radiographic images with vastly different contrast mechanisms, as well as systems possessing various advantages and disadvantages.

1.2 Conventional X-ray imaging

In 1895, Wilhelm Conrad Roentgen, a German physicist, was working with partially evacuated cathode ray tubes. In his dark room he noticed that even through heavy, black cardboard shielding, a fluorescent screen at some distance from his tube was glowing. Since the electrons could not escape the tube and he knew that his set-up was opaque to ultra-violet and visible light, Roentgen postulated that a previously unobserved form of radiation was responsible for the effect. He named the radiation “X”-rays, after the “x” used to indicate an unknown in mathematics. In his initial investigations he attempted to block the X-rays using sheets of paper, wood and aluminium, but failed. However, he discovered that the intensity of the X-rays incident on the screen reduced proportionally with the thickness and density of the materials placed before it, until it was almost completely obscured by lead coated glass. Finally, he swapped the fluorescent screen, which he had been using to detect the rays, for photographic plates and developed the first X-ray image.

The method's application to medicine was immediately apparent to Roentgen and the larger scientific community when he published his findings at the end of 1895. In the publication, he included the image of his wife's hand, taken in his lab, where her flesh appears as a translucent outline around her clearly more visible and opaque bones. X-rays were capable of showing the internal structure of objects without the need for invasive surgical procedures. The discovery was significant and the technology was rapidly adopted. The first commercial systems were built only a few months after, and a year later they were being used in specially created medical departments across the world, with one of the first radiology departments being established in Glasgow. In 1901 Roentgen received the first Nobel Prize in physics for his discovery of "Roentgen-rays", but internationally his original name ("X-rays") is still more commonly used.

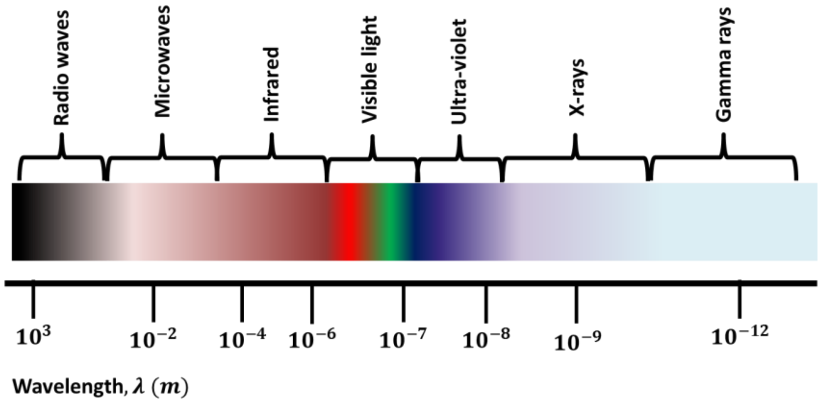

Figure 1-1. The electromagnetic spectrum, shown in order of decreasing wavelength.

X-rays have since been adopted in society for uses ranging from medicine and material testing to security applications [Haase et al. 1997]. Increased research interest has led to a better understanding of the nature of X-rays, and how best to optimise their production and detection. X-rays are now known to be electromagnetic (EM) waves with wavelengths, λ, much smaller than that of visible light, typically $0.1\ \mathrm{nm} \leq \lambda \leq 10\mathrm{nm}$ (Figure 1-1). They can be generated by accelerating/decelerating electrons such that they emit EM waves to produce polychromatic beams containing multiple energies e.g. laboratory X-ray tubes. Alternatively, at synchrotron facilities, crystals can used to select a single energy within this spectrum to produce monochromatic beams.

The current understanding of X-rays enables more detailed and quantitative explanations of Roentgen's early observations. However, it is first important to understand the mechanisms which govern X-ray interaction at the length scales of their wavelengths ($\sim 0.1\ nm$), which is about the size of an atom.

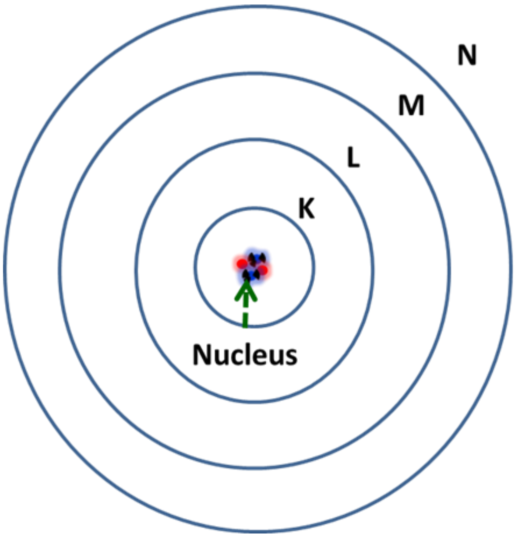

Figure 1-2 A simple model of an atom showing the nucleus and the shells (K, L, M, N).

The simplest model of the atom is one consisting of negatively charged electrons bound in quantized shells around a positively charged nucleus (Figure 1-2). The electrostatic attraction between the electrons and the nucleus governs the “strength” with which electrons are bound. This is called the “binding energy”, i.e. the energy needed to liberate an electron from its shell, which is a quantity that decreases for successive shells as their distance from the nucleus increases. If the energy of the incident X-rays is sufficiently higher than the binding energy of the electron, the latter can effectively be treated as a “free” particle.

When X-rays traverse matter, a number of interactions can occur between their EM fields and the EM fields generated by the atomic electrons of the material. These interactions contribute to the overall attenuation of the primary X-ray beam, leading to a loss in its transmitted intensity. However, such interactions are probabilistic events which depend on the energy of the incident X-rays. Hence, within the diagnostic imaging range, i.e. $5\ keV \leq E \leq 150\ keV,$ some of these interactions can be ignored because they do not contribute to X-ray attenuation; e.g. nuclear interactions and pair production do not take place below 1 MeV. It is also worth mentioning that X-rays can be transmitted through the material without interacting at all.

Within the range of energies used for diagnostic imaging, X-ray attenuation can be attributed to three mechanisms: elastic and inelastic scattering and photoelectric absorption. Among these three physical phenomena, photoelectric absorption and Compton scattering (inelastic) are the largest contributors to the attenuation of the beam, while elastic scattering accounts for only a small percentage of the physical interactions taking place within the object.

Elastic (coherent) scattering occurs when an X-ray photon is scattered off a particle without a corresponding loss of energy. In other words, the energy of the incident X-ray photon is equal to that of the scattered photon. If the scattering target is smaller than the wavelength of the X-rays, e.g. an atom, this is referred to as Rayleigh scattering, but when the interaction occurs with a free charged particle, it is referred to as Thompson scattering [Als-Nielsen & McMorrow 2011]. In reality, Thompson scattering is just a special case of Compton scattering. This latter process is inelastic, which means that the X-ray imparts some of its energy, as well as its momentum, to the electron. In order for this process to take place, the initial energy of the photon must be comparable to or greater than the rest mass of the electron. Finally, photoelectric absorption occurs when X-rays lose all of their energy to atomic electrons.

1.2.1 Photoelectric effect

A photon has the greatest likelihood of liberating a K-shell electron if it has energy comparable to, but slightly above, the binding energy of that electron. Any excess energy possessed by the photon is imparted to the electron as kinetic energy.

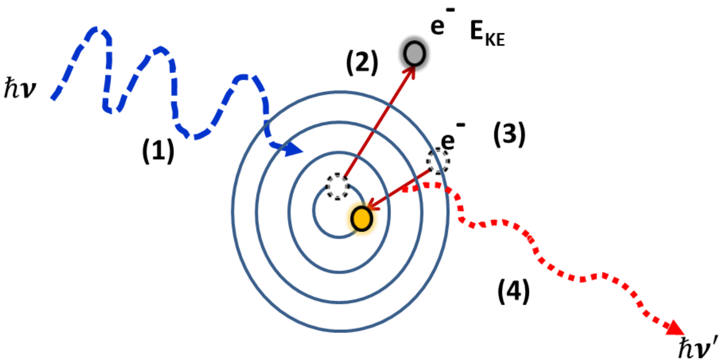

Figure 1-3 The photoelectric effect: (1) Incident photon with energy E=$\hbar$v, (2) electron is ejected, (3) outer-shell electron fills the vacancy, (4) atom emits radiation of a characteristic wavelength.

The kinetic energy of the liberated electron, E_{KE}, is:

$$E_{KE} = \hbar\nu - W, \tag{1-1}$$

where W is the work function (i.e. the binding energy of the electron), $\hbar$ is Planck's constant and ν is the frequency of the incident photon.

As a result of the interaction, there is a hole in the recently vacated shell which makes the atom energetically unstable. This hole can be filled by a cascading outer-shell electron, which results in the emission of radiation with energy that is equal to the difference in energy between the two shells, and is therefore characteristic to the atom. In some cases, this emitted radiation can liberate another electron from the atom, which is known as an Auger electron. The probability of the photoelectric effect occurring decreases rapidly with increasing energy; however, there are sharp increases in its probability near the absorption edges, i.e. the binding energy of the respective shells, as shown in Figure 1-4.

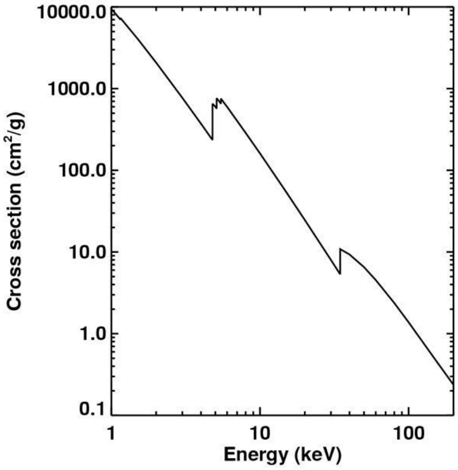

Figure 1-4 Photoelectric cross section in Xenon (Xe).

The photoelectric probability of interaction is represented by the "effective cross-section" of a material as "seen" by the incident photon. In general, it can be expressed as a ratio between the interacting and incident, $\sigma \propto \frac{Interacting\ photons}{Incident\ photons}$. To first approximation, the photoelectric cross-section of interaction, σ_{pe}, possesses the following relationship with respect to energy:

$$\sigma_{pe} \propto \frac{Z^3}{E^3}, \tag{1-2}$$

where Z is the atomic number (number of protons) and E is the energy of the X-rays.

1.2.2 Compton scattering

Compton scattering is an incoherent process, which means that the energy of the incident photon changes as a consequence of the interaction. For simplicity, the incident X-ray is treated as a ray, and the electron is considered as a stationary "rigid" sphere.

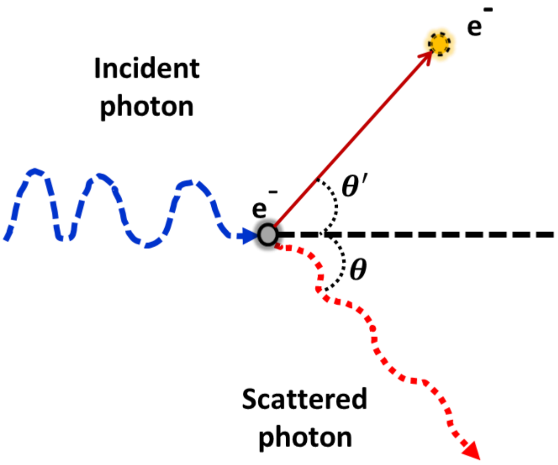

Figure 1-5 Compton scattering: an incident photon imparts some of its momentum to an electron, thereby losing some of its initial energy.

The photon is incident with momentum p_i, and interacts with an electron. After the interaction, the total momentum of the system is:

$$p_i = p_f + p_{el}, \tag{1-3}$$

where p_{el} is the momentum of the electron, and p_f is the final momentum of the photon. The electron and the photon are scattered at angles θ and θ' respectively, and part of the energy of the photon is lost to the electron such that $\lambda' > \lambda$. This interaction occurs with loosely bound electrons in the outer atomic shells, which are considered to be “free” because the energy of the incoming photon vastly exceeds their binding energy. The change in wavelength, $\Delta\lambda$, can be calculated by simultaneously considering conservation of energy and the conservation of momentum in Eqn. (1-3), leading to:

$$\Delta\lambda = \frac{h}{m_0 c}(1 - \cos\theta'), \tag{1-4}$$

where m_0 is the rest mass of the electron and c is the speed of light. A formal calculation of the cross-section of interaction for Compton scattering, σ_C, is beyond the scope of this work, but is expressed by the Klein-Nishina formula [Als-Nielsen & McMorrow 2011]. The Compton scattering cross-section varies with energy and density (ρ) in the following way:

$$\sigma_{Compton} \propto \frac{\rho}{E}. \tag{1-5}$$

Ultimately, the total cross-section of attenuation can be expressed as a sum of the individual cross-sections of each event:

$$\sigma_{tot} = \sigma_{pe} + \sigma_{Compton} + \sigma_{coh}. \tag{1-6}$$

However, contributions from coherent scattering can be neglected when considering certain geometries for attenuation based X-ray imaging. In particular, since the interaction occurs mostly in the forward direction, at very small angles, and is accompanied by a negligible loss in photon energy, it is still possible for these scattered photons to reach the detector. In this case, the elastically scattered photon is not seen as eliminated from the incoming beam, and thus does not contribute to beam attenuation. Furthermore, attenuation based X-ray imaging set-ups have been optimised to reduce the amount of scattering events (coherent and incoherent) detected. Scattered photons contribute to the image noise and introduce additional blurring to the image; therefore, they reduce the signal-to-noise ratio (SNR) of the image, its sharpness, and hence its overall quality.

The ratio between the flux of the scattered photons and the flux of primary beam photons is the scatter-to-primary ratio (SPR). This quantity is used to calculate the amount of scattering present in a given set-up. The SPR can be reduced in a number of ways, for example, by reducing the beam field size, introducing an air gap between the object being interrogated and the detector, or using an anti-scatter grid [Washburn & Johnston 1991]. However, the photoelectric effect and Compton scattering still contribute to the loss of X-ray intensity, and it is evident from the expressions given in Eqns.(1-2) and (1-5) that the former is much more dominant at lower energies, while the latter dominates at higher energies.

To calculate the amount of attenuation an X-ray beam suffers as it passes through matter, consider the homogenous slab shown in

, which possesses a number density of scattering atoms η, and a scattering cross-section σ. The former has units of cm^{-3} while the latter has units of area (cm^{2}). An incident beam of X-rays with intensity I_0, travelling through an infinitesimally thin slice of the slab with thickness dz, emerges with intensity $I - dI = I'$, where dI is the intensity attenuated within the distance dz.

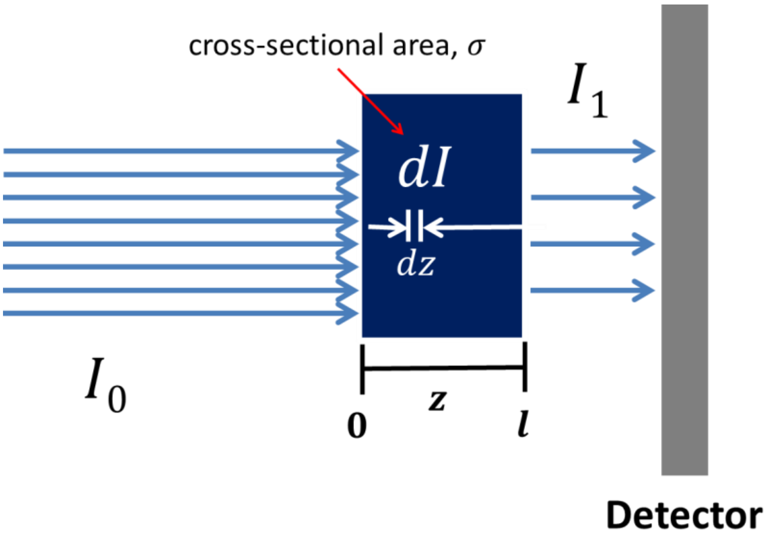

Figure 1-6 A slab of material with atomic number density, η, cross-section of interaction σ and thickness, l.

As previously mentioned, the ratio between the fraction of the beam attenuated by the slab dI, i.e. the interacting events, and the incident beam I, is proportional to the cross-section of interaction. Ultimately, this ratio is an expression of the probability of interaction between the X-rays and the targets within the slab. Hence, it follows that for a beam traversing an infinitesimal distance within the slab dz, with a number density of interacting targets η:

$$\frac{dI}{I} = -\eta\, \sigma\, dz\,. \tag{1-7}$$

The total attenuation caused by the slab can then be obtained by integrating both sides of Eqn. (1-7) between $z = 0$ and $z = l$, and noting that $I_{z=0} = I_0$ and $I_{z=l} = I_1$:

$$\ln\left(\frac{I_1}{I_0}\right) = -\eta\sigma l. \tag{1-8}$$

Taking the exponential of both sides leads to:

$$I_1 = I_0\, e^{-\eta\sigma l}. \tag{1-9}$$

The quantity $\eta\sigma$ can now be redefined as the linear attenuation coefficient μ, which has units of per unit length (cm^{-1}), and it determines the capacity of a given material to attenuate radiation. Therefore, in the diagnostic imaging range, the linear attenuation coefficient is obtained from the total cross-section of interaction mainly from the photoelectric and Compton processes, $\mu = \eta(\sigma_{pe} + \sigma_{Compton} + \cdots)$, since the contributions from coherent scattering can be mostly ignored.

Eq. (1-9) is a form of the Beer-Lambert law. However, in the above calculation the energy dependence of the linear attenuation coefficient was overlooked. The equation can be rewritten more formally for a polychromatic beam:

$$I = I_0 \int e^{-\int \mu(E,z)dz} dE. \tag{1-10}$$

Eqn. (1-10) can be used to explain the loss of intensity suffered by an X-ray beam as it propagates through matter, and forms the basic principles behind image formation.

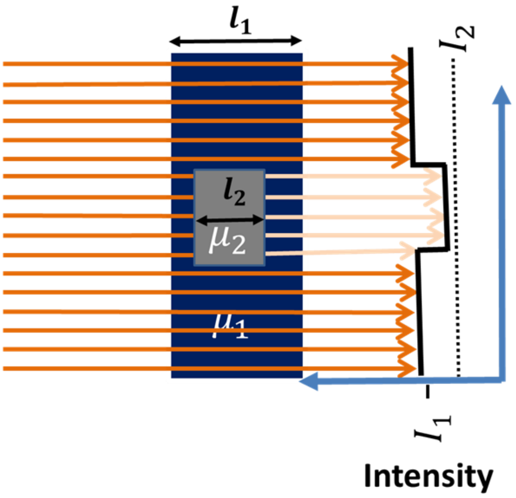

Figure 1-7 X-rays propagating through a material characterised by attenuation coefficient, μ_1, with thickness, l_1, which contains a detail with coefficient μ_2.

For example, consider investigating a detail placed within a slab of absorbing material with linear attenuation coefficient μ_1, as shown in Figure 1-7. If the detail possesses a different linear attenuation coefficient (μ_2) to the background material, then X-rays passing through both the background and the detail will be differently attenuated compared to those passing solely through the background. The difference in attenuation between the detail and its background material is quantified as the subject contrast.

In the absence of scattering, subject contrast can be mathematically defined as:

$$\mathrm{C} = \frac{|I_1 - I_2|}{I_1}, \tag{1-11}$$

where I_1 is the intensity of the X-rays, after they have traversed only one type of material, and I_2 is the intensity of the rays after passing through a detail of a certain thickness and the background material. Using Eqn. (1-10), in this case the intensities can be calculated as:

$$\mathrm{I}_1 = I_0 e^{-\mu_1 l_1}, \tag{1-12}$$

$$\mathrm{I}_2 = I_0 e^{-\mu_1 (l_1 - l_2)}\, e^{-\mu_2 l_2}. \tag{1-13}$$

It is important to note that I_2 in Eqn. (1-13) is the total attenuation of the beam after passing through a thickness $l_1 - l_2$ of the slab, as well as through the detail in the absence of scattering, hence both attenuation coefficients appear within the equation. Following straightforward simplification, contrast can be written as:

$$\mathrm{C} = 1 - e^{(\mu_1 - \mu_2)\, l_2}. \tag{1-14}$$

Eqns. (1-10)-(1-14) show that the ability of an X-ray imaging set-up to detect details can be limited by the contrast of the investigated samples. In a clinical setting, this can be a disadvantage, firstly because it follows that less attenuating objects are less visible in X-ray images. The most famous example would be the radiograph taken by Roentgen of his wife’s hand, where her bones and wedding ring (high Z objects) show up clearly, while the soft tissue surrounding (low Z objects) is barely visible. Secondly, although high attenuation may lead to a greater visibility, it also increases the likelihood of X-rays, which are a form of ionising radiation, to cause more damage within tissue. For example, the early adoption and extensive use of X-rays, before its ionising nature was fully understood, led to numerous cases of radiation burn, sickness and even death among its users.

In time, safety protocols and standards were introduced, which aimed to minimise the dose delivered to healthcare workers and patients. From this arose the principle of using radiation doses which are “as low as reasonably possible” (ALARA), which has been partially responsible for driving the advancement of X-ray imaging, especially in the medical sector. This reduction in dose can be achieved by reducing the two major sources of X-ray attenuation, namely the photoelectric effect and Compton scattering. Knowledge of their cross-sections of interactions, which are shown in Eqns. (1-2) and (1-5), can be used to achieve this goal. For example, if the energy of the X-ray beam is increased, it would lead to a corresponding decrease in the likelihood of interaction, and hence to the attenuation of X-rays. However, as previously mentioned, this reduction in attenuation also makes objects less visible and renders images less clinically useful.

During Roentgen’s initial investigations, he performed numerous experiments to test the refractivity and reflectivity of X-rays. Given the equipment available to him at the time, he concluded that it was not possible to observe either phenomenon [Röntgen 1896]. This has since been known to be inaccurate. Indeed, detecting these refracted photons and extracting the information they provide has been the subject of research within the field X-ray phase contrast imaging (XPCI).

1.3 X-ray Phase Contrast Imaging

Phase contrast effects were first explained by Zernike in the 1930s while he was working with diffraction gratings [Zernike 1942; Zernike 1955]. His early work led to the development of optical phase contrast microscopy. However, phase contrast signals are harder to observe at the X-ray end of the EM spectrum. A classical description of how phase contrast effects are generated can be given by modelling the atomic electrons in the interacting medium as forced harmonic oscillators.

1.3.1 Dispersion

A linear, isotropic and homogenous dielectric medium is placed downstream of an X-ray source. Although EM waves consist of both electric and magnetic fields oscillating orthogonally with respect to each other, for this treatment, the magnetic component can be neglected, since its contribution only becomes important for charged particles moving close to the speed of light [Peatross & Ware 2012]. The electric field $\vec{E}$ can be written as a complex plane wave:

$$\vec{E} = \tilde{E}_0 e^{i(\vec{k}\vec{r}-\omega t)}\,, \tag{1-15}$$

where ω, its angular frequency, is equivalent to $\overbrace{\left\{\frac{2\pi}{\lambda}\right\}}^{k} c$, and the constant phase term, $e^{i\phi}$, is included in the quantity $\tilde{E}_0$. In this model, each electron is independently driven by a force $\vec{F}$ due to the electric field, while the effects of its neighbours are ignored:

$$\vec{F} = q\vec{E}, \tag{1-16}$$

where q is the charge of the electron. As shown in Figure 1-8, the force causes a displacement of the electron cloud, thereby inducing a dipole moment, μ_d:

$$\mu_d = -q\vec{r}, \tag{1-17}$$

where $\vec{r}$ is the displacement of the charge.

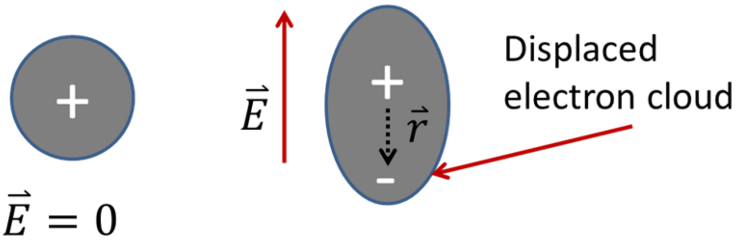

Figure 1-8 Depiction of an unpolarized atom and one polarized by with an applied E field, where the displacement of the electron cloud induces a dipole.

The force in Eqn (1-16) causes the electron to oscillate about its equilibrium position. In this simple interpretation, the motion of the charge only obeys Newton's laws and relativistic effects are neglected. In this model, it is reasonable to propose that the electron is also subject to a restorative force which is proportional to its displacement, $-Cx,$ and a damping factor proportional to the velocity of its oscillation, $-m\gamma v$ [(Als-Nielsen & McMorrow 2011; Feynmann et al. 1964)]. Hence, the classical equation of motion for the electron is:

$$q\vec{E} = \left[\underbrace{m\ddot{x}}_{mass \times acceleration} + \overbrace{m\gamma\dot{x}}^{damping} + \underbrace{Cx}_{\substack{restoring \\ force}}\right], \tag{1-18}$$

where $\ddot{x} \equiv \frac{d^2x}{dt^2},\ \dot{x} \equiv \frac{dx}{dt}, m$ is the mass of the electron and C is a constant term. A trial solution for Eqn. (1-18) exists in the form of $x = \vec{x}e^{i\omega t}$, which also suggests that an electron follows the driving oscillating field. Eqn. (1-18) can be solved by substituting in this trial solution and rearranging:

$$\frac{q\vec{E}}{m}e^{i\omega t} = [(i\omega)^2 + (i\omega)\gamma + \omega_0^2]\,\vec{x}e^{i\omega t}, \tag{1-19}$$

where we have used the relationship, $\omega_0 = \sqrt{\frac{C}{m}}$, and ω_0 is the resonant frequency of the system. An expression for the displacement of the electron can be obtained from Eqn. (1-19):

$$\vec{x} = \frac{q\vec{E}}{m(\omega_0^2 - \omega^2 + i\omega\gamma)}. \tag{1-20}$$

It is now possible to obtain an expression for the dipole moment of the material as a function of the system's physical parameters:

$$\mu_d = -\frac{q^2\vec{E}}{m(\omega_0^2 - \omega^2 + i\omega\gamma)}. \tag{1-21}$$

This expression is true for one induced dipole. However, the medium consists of a number of charges that can be induced to create a dipole moment described by Eqn. (1-21). The average behaviour of the dipoles as a response to the propagating wave leads to the macroscopic properties of the material. For a dielectric material, the creation of multiple dipoles causes polarization: that is a separation of positive and negative charges. Formally, the polarization of a material, $\vec{P}$, is defined as the density of dipoles within the material:

$$\vec{P} = \frac{1}{V}\sum_{V}\mu_d, \tag{1-22}$$

where V is the volume of the medium. This can be rewritten in terms of the number density, N, and the average dipole moment $\langle\mu_d\rangle$:

$$\vec{P} = N\langle\mu_d\rangle. \tag{1-23}$$

The average behaviour of the charges within the material is shown in Figure 1-9. It is important to understand that the polarization is a vector quantity which describes the response of the material to an external electric field. The displacement of charges induces an internal electric field, E_m, which opposes the applied external electric field and causes a reduction in the total electric field shown in Figure 1-9. We can account for this reduction by defining an electric displacement field, D:

$$D = \underbrace{\epsilon_0\vec{E}}_{vacuum\ current} + \underbrace{\vec{P}}_{bound\ charges}, \tag{1-24}$$

where ϵ_0 is the permittivity of free space. The first term is defined as a vacuum current, and it does not involve any motion of charged particles, while the second takes into account the response of the bound charges. Eqn. (1-24) can be rewritten in another form:

$$\vec{D} = \epsilon_0\vec{E} + \epsilon_0\chi_e\vec{E}, \tag{1-25}$$

with:

$$\vec{P} = \epsilon_0\chi_e\vec{E}, \tag{1-26}$$

where the polarization is redefined according to a new quantity, χ_e, the electric susceptibility of the material.

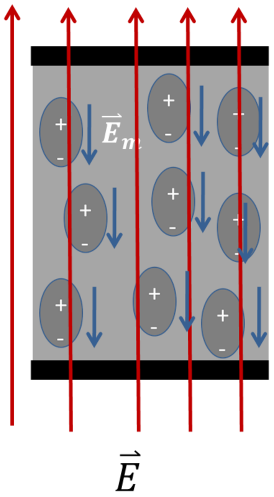

Figure 1-9 Induced dipoles within a dielectric material lead to the creation of an opposing electric field, E_m.

Eqns. (1-25) and Eqn. (1-26) allow us to simplify Eqn. (1-24) as follows:

$$\vec{D} = \epsilon_0 \underbrace{(1 + \chi_e)}_{\epsilon_r}\vec{E}, \tag{1-27}$$

where $\epsilon_r = \frac{\epsilon}{\epsilon_0}$ is the relative permittivity of the material. Finally, we note that the electric susceptibility (χ_e) of the material is a function of the frequency of the incoming radiation and the resonant frequency of the electron by combining Eqns. (1-21), (1-23), and (1-26):

$$\chi_e = \frac{Nq^2}{m\epsilon_0(\omega_0^2 - \omega^2 + i\omega\gamma)}. \tag{1-28}$$

A physical interpretation of this quantity is not intuitive because it is a complex number but, in general, the susceptibility acts as the medium's response function to an electric field:

$$\chi_e = \frac{Nq^2}{m\epsilon_0}\left[\underbrace{\frac{(\omega_0^2 - \omega^2)}{(\omega_0^2 - \omega^2)^2 + \gamma^2\omega^2}}_{real\ part} - i\underbrace{\frac{\gamma\omega}{(\omega_0^2 - \omega^2)^2 + \gamma^2\omega^2}}_{imaginary\ part}\right]. \tag{1-29}$$

However, unlike the definitions for the electric field in Eqn. (1-15) or the expression for the position in Eqn. (1-20), where the imaginary parts are ignored in favour of the physical result, for χ_e, both imaginary and real parts contribute to the behaviour of the medium. This can be understood by considering how a medium with a complex electric susceptibility affects a complex, oscillating electric field. This leads to a complex relative permittivity that is dependent on the frequency of the incoming wave. This frequency dependent behaviour, which relates the speed of a propagating wave within a material to its frequency, is known as dispersion.

1.3.2 The refractive Index

Maxwell's equations allow us to describe EM waves as they propagate through free-space, and can be adapted for propagations through conducting or dielectric media. In free space, the equations can be written as:

$$\nabla.\vec{E} = 0, \tag{1-30}$$

$$\nabla.\vec{B} = 0, \tag{1-31}$$

$$\nabla \times \vec{B} = \mu_0 \epsilon_0 \frac{\partial \vec{E}}{\partial t}, \tag{1-32}$$

$$\nabla \times \vec{E} = -\frac{\partial \vec{B}}{\partial t}. \tag{1-33}$$

The constant μ_0 is the permeability of free space to a magnetic field, $\vec{B}$, and has been ignored in the previous treatment. By taking the curl of Eqn. (1-33) and using Eqn. (1-30), the expression becomes:

$$\nabla \times \left(\nabla \times \vec{E}\right) \equiv \nabla.\underbrace{\left(\nabla.\vec{E}\right)}_{0} - \nabla^2 \vec{E} = -\nabla \times \frac{\partial B}{\partial t}, \tag{1-34}$$

$$\nabla \times \frac{\partial \vec{B}}{\partial t} = \mu_0 \epsilon_0 \frac{\partial^2 \vec{E}}{\partial t^2}. \tag{1-35}$$

Combining these equations leads to an expression in Eqn. (1-36), which resembles the wave equation written in Eqn. (1-37):

$$\nabla^2 \vec{E} - \mu_0 \epsilon_0 \frac{\partial^2 \vec{E}}{\partial t^2} = 0, \tag{1-36}$$

$$\nabla^2 \Psi - \frac{1}{\mathrm{v}^2} \frac{\partial^2 \Psi}{\partial t^2} = 0, \tag{1-37}$$

where Ψ is the wave and v is its speed. By comparing the variables in Eqns. (1-36) and (1-37), a relationship between the speed of the wave and the electric permittivity and magnetic permeability constants, μ and ϵ, can be derived:

$$\mathrm{v} = \frac{1}{\sqrt{\mu\epsilon}}. \tag{1-38}$$

For a wave propagating through a vacuum, $\mu = \mu_0$ and $\epsilon = \epsilon_0$, then $\mathrm{v} = c$, which is the speed of light. Both μ and ϵ are dependent on the properties of a medium, meaning that waves will propagate at different speeds within media possessing different values of μ and ϵ. The ratio of the speeds of a wave in free space and in a material is defined as the refractive index, n:

$$n = \frac{c}{\mathrm{v}}. \tag{1-39}$$

Substituting in Eqn. (1-38) into Eqn. (1-39) and ignoring the magnetic properties of material:

$$n = \pm\sqrt{\epsilon_r}, \tag{1-40}$$

$$n = \pm\sqrt{(1 + \chi_e)}. \tag{1-41}$$

Equations (1-29) and (1-41) lead to the definition of the complex refractive index, n, which can be written in the general form:

$$n = n' + in'', \tag{1-42}$$

where n' is any real number representing the real part of a complex number, n'' is a representation of its imaginary part and the minus sign is enforced by convention. This is expressed in more familiar notation as:

$$n = \underbrace{1 - \delta}_{real\ part} + i\beta. \tag{1-43}$$

The refractive index is a measure of the change of speed experienced by a propagating wave as it passes through different media. However, a direct description for its effect on the wave can be obtained by revisiting Eqn. (1-15) and using Eqn. (1-39) to rewrite the complex electric field (remembering that $\omega = \mathrm{k}c$) as follows:

$$\vec{E} = \tilde{E}_0 e^{i(\frac{\omega n}{c}\Delta r - \omega t)} , \tag{1-44}$$

for a wave going through a medium of thickness $\Delta \mathrm{r}$. When the complex refractive index is placed into Eqn. (1-44), a new expression is obtained:

$$\vec{E} = \tilde{E}_0 \underbrace{e^{i\omega(\frac{n'}{c}\Delta r - t)}}_{wave+phase} \underbrace{e^{-\frac{\omega n''}{c}\Delta r}}_{absorption}. \tag{1-45}$$

The two parts correspond to a propagating wave that is multiplied by some phase factor, $e^{i\omega(t - \frac{n'}{c}\Delta r)}$, and an exponential dampening term, $e^{-\frac{\omega n''}{c}\Delta r}$. Finally, a comparison can be made between this damping term and the Beer-Lambert attenuation coefficient in Eqn. (1-9) by taking the square modulus of Eqn. (1-45) and finding the intensity of the wave:

$$\left|\vec{E}\right|^2 = \left|\tilde{E}_0\right|^2 e^{-\frac{2\omega n''}{c}.\Delta r}, \tag{1-46}$$

leading to:

$$e^{-\frac{2\omega n''}{c}\Delta r} = e^{-\mu \Delta r}. \tag{1-47}$$

By comparing with the attenuation coefficient in Eqn. (1-9), we deduce that:

$$2kn'' = \mu. \tag{1-48}$$

Equation (1-48) directly links the imaginary quantity, n'', and therefore β, to the linear attenuation coefficient, suggesting that the term is responsible for the dissipation of wave energy as it propagates through a medium. However, the real part n', of the refractive index can be separated into two terms:

$$\vec{E} = \tilde{E}_0 \underbrace{e^{i\omega\left(\frac{1}{c}\Delta r - t\right)}}_{wave} \underbrace{e^{\frac{i\omega\delta}{c}\Delta r}}_{phase\ factor}. \tag{1-49}$$

The first term is just the original propagating wave, but the second term describes the phase change experienced by the wave as it propagates through the medium, as a result of δ. In truth, both the real and imaginary parts of the refractive index are dependent on each other, and a full expression of this dependence can be expressed via the Kramers-Kronig relations [Kronig 1926; Kramers 1927].

1.4 Motivation for phase contrast imaging

In addition to attenuation, X-rays can also undergo refraction; therefore, a complete description of a real object needs to account for both these physical modes of interaction. This leads to the introduction of the complex transfer function T, which describes how objects with both phase and attenuating properties, modify an incident X-ray beam. In the case of extended object geometry, T can be calculated by integrating over the extent of the object for δ and β as follows:

$$T = e^{-[ik\int_0^r \delta\, dr]-[k\int_0^r \beta\, dr]}, \tag{1-50}$$

where $\phi\ (r) = \ k\int_0^r \delta(r)dr$ and $\alpha(r) = \ k\int_0^r \beta(r)dr$ are the total phase shift and the attenuation caused by an object of length r. Such effects can be sensed by a dedicated XPCI set-up.

In fact, XPCI techniques can be sensitive to more than one form of contrast i.e. phase contrast and the traditional attenuation contrast provided by a conventional set-up. Indeed, XPCI set-ups provide increased capability of detecting fine detail within an object's internal structure, which is otherwise invisible to conventional set-ups. Contrast enhancement can occur in three ways. Firstly, δ, which governs refraction, can be up to three orders of magnitude greater than the attenuating quantity, β, meaning that phase contrast signals can be inherently higher than attenuation signals. Furthermore, objects in close proximity which possess identical β values may be differentiated by the set-up thanks to the differences in their δ values. According to Eqn. (1-11), this difference leads to a higher subject contrast. Finally, object boundaries are well delineated in phase contrast images because phase contrast effects occur more prominently at the interface between objects with different δ values.

Figure 1-10 shows how δ and β vary as a function of X-ray energy for Carbon, where it can be observed that δ can be much greater than β, and that it decreases more slowly with increasing energy than β. The observation is significant because it indicates that attenuation suffers more than refraction at higher X-ray energies, which is particularly beneficial for XPCI set-ups when compared against their X-ray attenuation counterparts. This is in line with one of the conclusions drawn at the end of section 1.2, namely that photoelectric absorption is less probable at higher energies.

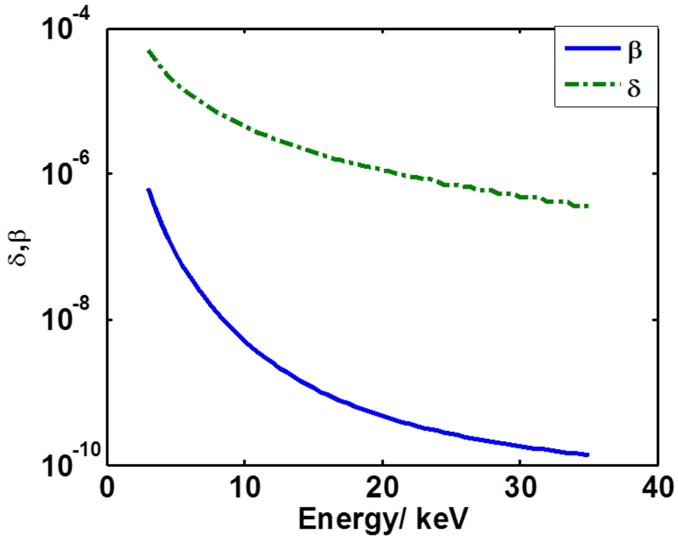

Figure 1-10 Variation of δ and β with respect to energy for Carbon.

However, this decrease in the probability of interaction for the photoelectric effect, and therefore attenuation, at higher energies does not necessarily reduce the image quality in an XPCI system when the signal can be supplemented by phase contrast. In fact, phase contrast images may provide a means of further reducing the dose necessary to produce useful X-ray images, since phase effects do not rely on attenuation to generate contrast. This realization, as well as the other benefits provided by XPCI set-ups, drives the development of XPCI as a tool to replace the established attenuation-based systems.

However, X-ray refraction is notoriously difficult to detect because the angles through which X-ray photons are deflected are very small, therefore requiring extremely stable and sensitive set-ups. So far, such set-ups have only been realised in highly controlled laboratory environments with specialised equipment; however this obvious limitation, which renders XPCI impractical for real-world applications i.e. to replace the current conventional set-ups, is being addressed by current research efforts.

The motivation for the work undertaken here is to pursue developments which would make XPCI more practical for use outside of laboratory environments. The benefits of such a system have been enumerated throughout this chapter, but once again emphasis must be placed on its increased image contrast. This could reduce some of the risks associated with diagnostic X-ray imaging, e.g. probability of cancers, false positives/negatives etc. Along with more informative images, simpler XPCI set-ups, which can be readily translated, would also enable more detailed investigations and a deeper understanding of the structure of investigated objects.

Consequently, the overall aim of this work was to study and develop novel XPCI set-ups using the edge illumination method, a technique which utilises two periodic masks that need to be finely aligned to sense phase shifts. This technique will be introduced in the next chapter. First, the factors affecting its refraction sensitivity will be studied to ensure that they are well understood, and that they could be used to design simpler set-ups while preserving the sensitivity as much as possible. Next, a significantly simpler implementation of the method (using a single periodic mask), which has significantly less stringent stability requirements, will be compared against its predecessor (two mask), both experimentally and via computer simulations. The latter will be used to study the loss of refraction sensitivity and, more importantly, to determine whether this could be recovered through appropriate set-up modifications. Finally, another novel edge illumination set-up will be tested to determine whether it is possible to build a set-up which is capable of sensing refraction signals along two orthogonal directions simultaneously.

Chapter 2 Phase Contrast Imaging

2.1 Overview

This chapter reviews the history of phase contrast imaging techniques and describes various phase sensitive set-ups, as well as listing some of their advantages and disadvantages. Among them, the standard edge illumination set-up, which is the starting point for this work, is introduced, and the physical principles which govern the method are explained. Finally, a phase retrieval algorithm, which allows for the separation of phase and absorption signals, is presented.

2.2 X-ray Phase Contrast Imaging (XPCI)

The primary goal of XPCI is to produce high quality images which can supplement the information obtained from attenuation-based X-ray imaging. As such, the current capabilities of the conventional technique, i.e. rapid acquisition time, large fields of view, limited dose deposition etc. must first be matched by XPCI techniques before they can be seen as a practical alternative. This can prove particularly challenging because XPCI methods are relatively recent developments, which are yet to be fully optimised for “real-world” use. The first XPCI method was developed several decades after the initial discovery, and subsequent use, of X-rays as a diagnostic tool. Over the years, several set-ups and methods have been designed to detect and extract the phase and amplitude information, each possessing its own advantages and disadvantages. Initially, their use was restricted to synchrotron facilities, but now they are being translated to laboratory environments. In the last two decades, new modalities have emerged, each of which represents an incremental step towards the realisation of a “real-world” commercial XPCI system.

2.2.1 Crystal interferometry

The first XPCI method utilised the Bonse-Hart interferometer, which was demonstrated in 1965. However, it was only in the mid-90s that its potential as a tool for biomedical imaging was first suggested [Bonse & Hart 1965; Momose et al. 1996]. The set-up consisted of three parallel lamellae, which were monolithically cut from a perfect silicon crystal. The three blocks were equidistant from each other and are referred to as beam splitter (S), mirror (M) and analyser (A), respectively. A schematic of the set-up is shown in Figure 2-1.

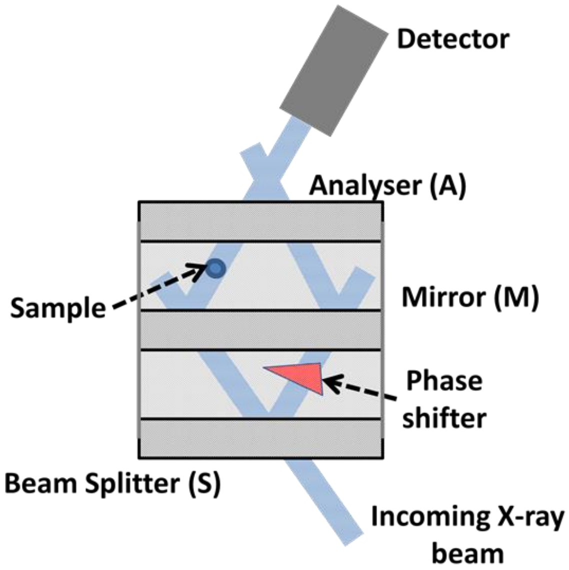

Figure 2-1 A Bonse-Hart interferometer consisting of three crystals acting as beam splitter (S), mirror (M) and analyser (A) respectively. A wedge-shaped phase shifter is placed in the path of the reference beam, while the object is placed in the other beam. The interference pattern is measured by a detector placed after the analyser crystal.

When the Bragg diffraction condition is satisfied such that,

$$n\lambda = 2d\sin\theta, \tag{2-1}$$

where n is an integer, λ is the wavelength of the incident radiation, d is the distance between adjacent atomic planes; the planes reflect X-rays at an angle θ. As a result, the first crystal (S) “splits” the incident X-ray beam, creating two mutually coherent beams propagating in the forward direction. The beams then interact with the mirror (M), where they are split once more. At the analyser crystal (A), the diffracted beams from each path are recombined and their interference pattern is measured as they exit the crystal.

Since the lamellae are cut from the same crystal, they are automatically aligned to within one interatomic distance, and since the beams then traverse the same path length, they remain coherent. A phase shifter can be inserted into the reference beam to introduce a relative phase difference between the two beams and create a series of straight interference (carrier) fringes. When an object is placed in the “sample branch”, the fringe lines are distorted according to the absorptive and refractive properties of the object. The displacement of the carrier fringes can be analysed to give a direct measure of the object’s phase.

The method was shown to produce quantitative phase contrast information for biological samples [Momose et al. 1996; Momose 2003]. However, the set-up relied on the precise cutting of a single perfect crystal, which results in limited fields of view, and suffered from stringent stability and alignment requirements. The technique is also limited to monochromatic radiation, which restricted it to dedicated facilities, such as synchrotrons. This method can provide a high sensitivity but its inherent constraints explain its limited adoption as a “real-world” imaging technique [Bravin et al. 2013].

2.2.2 Analyser-based Imaging

Analyser based imaging (ABI) employs some of the elements of a Bonse-Hart interferometer to construct a simpler set-up. A schematic of an ABI system is shown in Figure 2-2(a), where a monochromator defines a beam and directs it toward an analyser crystal.

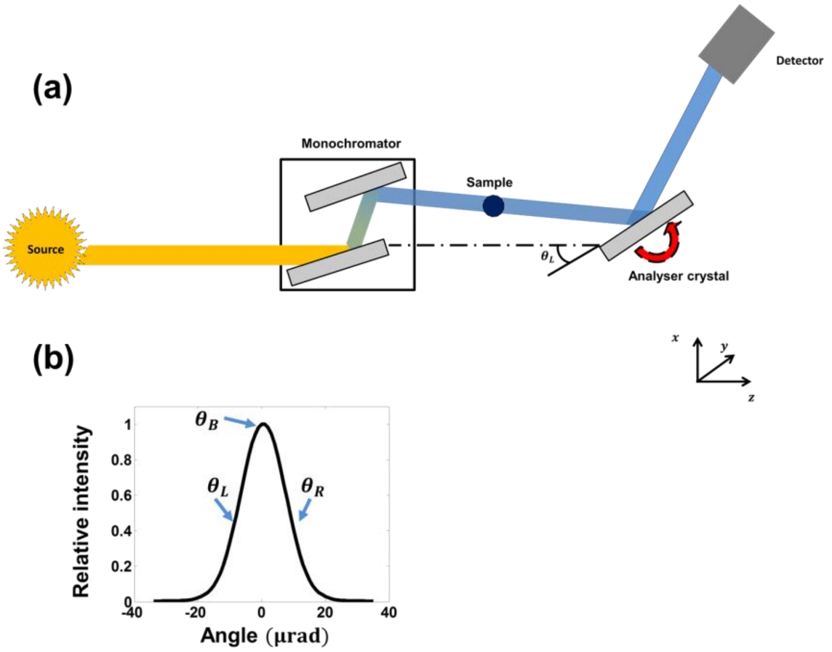

Figure 2-2 Schematic of the analyser based imaging set-up, consisting of a monochromator, a sample, an analyser crystal and a detector. The rocking curve (b) expresses how the intensity changes with respect to the angle with which the X-rays hit the analyser.

The second crystal is called an analyser because it acts as an angular filter. Thanks to the Bragg diffraction phenomenon, at a given energy, the analyser reflects maximally when the beam hits the crystal at the Bragg angle, θ_B. However, when the crystal is rocked off this angle, a decrease in its reflected intensity is observed. Hence, the detected intensity changes as a function of the angle between the incoming beam and the analyser crystal. The function which relates the intensity of the detected beam with its angle of incidence with respect to the crystal is known as the “rocking curve” (RC), and it is shown in Figure 2-2(b).

If the analyser crystal is positioned at its Bragg angle and a phase object is placed before the analyser, then the refraction suffered by the beam would change its angle of incidence upon the crystal compared to the case when no object is present. This would correspond to a reduction in the intensity of the reflected beam, and hence a decrease in the measured intensity. Alternatively, if the crystal is rocked slightly off its Bragg angle, such that it sits on one of the RC slopes (indicated as θ_L or θ_R in Figure 2.2(b)), either an increase or decrease in the reflected intensity would be measured, depending on the direction in which the beam is refracted. This is analogous to ascending or descending the RC slopes, and translates into a bright or dark fringe in the image. In other words, the RC relates changes of intensity to the angle of refraction.

ABI belongs to the family of “differential phase imaging” (DPI) techniques. They are so-called because the angular deflection to which they are sensitive is proportional to the first derivative of the phase along the direction of refraction:

$$\Delta\alpha = \frac{1}{\mathrm{k}} \frac{\partial \phi}{\partial x}. \tag{2-2}$$

In Eqn. (2-2), $\Delta\alpha$ is the refraction angle, $k = \frac{2\pi}{\lambda}$, where λ is the wavelength of the incoming radiation, and $\frac{\partial \phi}{\partial x}$ is the derivative of the phase along the x-direction (see Figure 2-2(a)). Depending on the types of features present in the sample, the beam is likely to undergo several types of distortions, i.e. it can be absorbed, refracted and scattered. In the context of XPCI, the latter refers to multiple refractions occurring at a sub-pixel scale, which cannot be resolved by the pixel. These changes can be isolated on separate images and retrieved by using an algorithm which requires the same number of images as the number of unknowns. In one of the earliest examples published by Chapman et al [Chapman et al. 1997], only two channels (absorption and refraction) were retrieved. Hence two images were acquired, one on each slope of the RC. However, in later works, algorithms were developed to retrieve also the dark-field (or “ultra-small angle X-ray scattering” (USAXS)) signals [Rigon et al. 2003; Rigon et al. 2007; Wernick et al. 2003; Oltulu et al. 2003; Pagot et al. 2003]. It was shown that the best SNR and most accurate retrieval of USAXS angles were achieved when the third image was acquired near the top of the RC, while the first two were acquired on opposite slopes. The dark-field/USAXS signal is important because it provides a map of the sample inhomogeneity. These inhomogeneous details cause multiple refractions of the X-ray beam and, since this occurs at the sub-pixel scale, the details cannot be individually resolved. However, by analysing an ensemble of these details, the dark field signal can be retrieved. In the case of ABI and edge-illumination, which will be introduced later, the signal manifests as a broadening of the X-ray beam.

ABI is similar to the Bonse-Hart interferometer, and therefore shares some of its limitations. In particular, the need for a monochromatic source confines ABI mainly to synchrotron facilities where this is readily available. However, unlike its predecessor, it provides a much simpler set-up.

2.2.3 Propagation based Imaging

In the late 1940s Gabor developed the in-line holography method for electron microscopy in order to eliminate the need for objectives. The technique was capable of recording the phase and amplitude information from an object [Gabor 1948]. In the mid-90s, the same principles were applied to monochromatic hard X-rays by Snigirev et al using synchrotron sources [Snigirev et al. 1995]. Later, Wilkins et al showed that the technique could also be implemented with polychromatic tube sources as long as its lateral spatial coherence $d_{\perp}$ was sufficiently large, i.e. a focal spot of a few microns was used [Wilkins et al. 1996]. An expression for the lateral coherence length is given by:

$$\mathrm{d}_{\perp} = \frac{\lambda r_n}{\sigma}, \tag{2-3}$$

where λ is the wavelength of the radiation, r_n is the source to detector distance, and σ is source size.

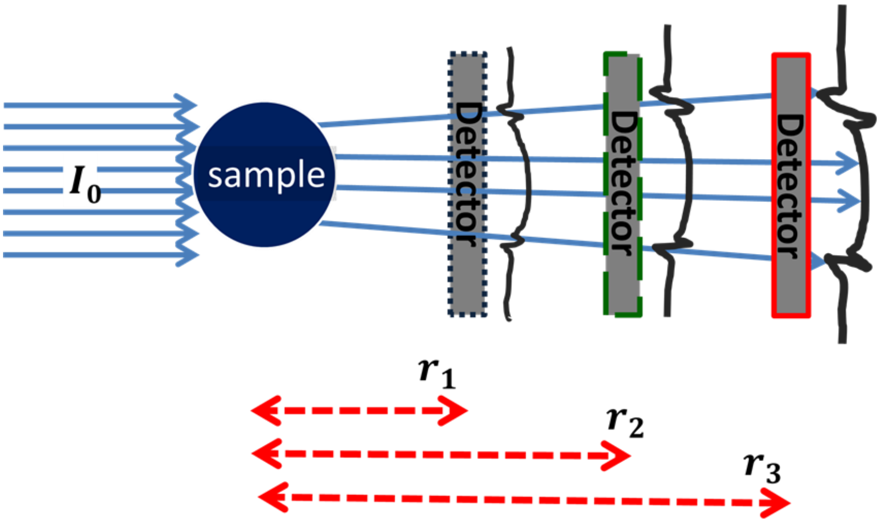

Figure 2-3. A free-space propagation (FSP) set-up, which shows how the obtained signal varies as a function of the propagation distance for an object illuminated by a plane wave.

The method became known as free-space propagation (FSP) because it eliminates the need for any optical elements, such as an analyser crystal. Thus far, it is the simplest XPCI set-up. A basic synchrotron set-up is shown in Figure 2-3, where a sample is illuminated by a monochromatic, spatially coherent wave front. The object introduces distortions to the wave field, such that the detected wave is a combination of the scattered and non-scattered parts of the wave. If allowed to propagate, these two components of the wave interfere. A detector is placed at some distance, r, downstream of the sample so that it can record the interference pattern. The intensity of the detected wave can be expressed as,

$$I(Mx, My; \lambda) \approx I_0 e^{-2k \int_{Sample} \beta(x,y,z;\lambda) dz} \left(1 - \frac{r\lambda}{2\pi M} \nabla^2 \Phi(x, y; \lambda)\right), \qquad \textbf{(2-4)}$$

where r is the propagation distance after the object, $\nabla^2 = \left(\frac{\partial^2}{\partial x} + \frac{\partial^2}{\partial y}\right)$, is the 2D Laplacian operator, $M = \frac{(r_0 + r)}{r_0}$ is the magnification factor and I_0 is the intensity measured at the object plane. Note that Eqn. (2-4) refers to the case of illumination by a spherical wave, whereas if the object is illuminated by a plane wave, the system possesses unit magnification. In deriving Eqn. (2-4) it is assumed that $\frac{r\lambda}{2\pi M} \nabla^2 \Phi(x, y) \ll 1$, which suggests that the phase contrast signal increases as the distance from the object increases [Peterzol et al. 2005]. Moreover, since $I \propto \nabla^2 \Phi(x, y)$, it is evident that interference is strongest where the sharpest changes in the phase occur. This is illustrated in Figure 2-3 and leads to the well-known edge enhancement features typical of FSP phase contrast images.

Although the raw images could be used as they are, since they contain more information than a conventional radiological image [Castelli et al. 2011], the phase and absorption components can also be separated. By applying a series of assumptions, the transport-of-intensity (TIE) formalism allows quantitative retrieval of ϕ, provided that the incident intensity is known and the transmitted intensity is measured (typically in more than one condition) [Peterzol et al. 2005]. Alternatively, a single defocused image may be used, but much stronger assumptions must be made on the sample [Paganin et al. 2002].

Thanks to its simplicity, FSP is widely used at both synchrotron and in laboratory environments. However, it is evident from Eqn. (2-3) that as the source size increases, the lateral coherence length decreases, which in turn reduces the detected phase contrast signal. This can be remedied by increasing the propagation distance, which means that large conventional sources would require increasingly more space, leading to significantly diminished X-ray flux, due to the inverse square law. These two factors are largely responsible for obstructing FSP's translation into "real-world" systems [Bravin et al. 2013]; in principle, they could be circumvented through the development of highly intense microfocal sources, but these are not currently available.

2.2.4 Grating Interferometry

Grating Interferometry (GI) is an interferometric XPCI method based on the Talbot effect [Talbot 1836]. It was observed that when illuminated by a coherent plane wave, a self-image of a periodic object would manifest at distances which were multiples of the Talbot distance, z_T:

$$\mathrm{z_T} = \frac{\zeta 2p^2}{\lambda}, \tag{2-5}$$

where p is the period of the object and ζ is the Talbot order. In addition, it was later shown that these self-images also appear at fractional distances but shifted in periodicity [Talbot 1836; Momose et al. 2003]. The method was first applied to hard X-ray imaging by David et al, and soon afterwards by Momose et al [David et al. 2002; Momose et al. 2003]. In the Talbot configuration, two gratings are placed sequentially after the sample. The first is a phase grating (G_1), which imposes a known phase modulation to the wave front. This phase modulation is then translated into an intensity pattern that varies with distance, and creates a self-image at Talbot distances.

In practice, a self-image of G_1 is projected unto the plane of the absorption grating (G_2), which consists of a series of absorbing and transmitting lines. The gratings have periods p_1 and p_2 respectively, where usually $p_2 = \frac{p_1}{2}$. The setup shares some similarities with the Bonse-Hart and ABI techniques because it uses the second grating as an analyser. The range of applicability of GI was extended further when it was applied to large, conventional X-ray sources, which required modifying the set-up into a Talbot-Lau configuration [Pfeiffer et al. 2006]. This incorporates an additional grating (G_0) at the source plane, which creates a series of individually coherent but mutually incoherent sources. Consequently, it decreases the spatial coherence requirements placed on the uncollimated source and enables the use of much larger focal spots. A Talbot-Lau set-up is shown in Figure 2-4.

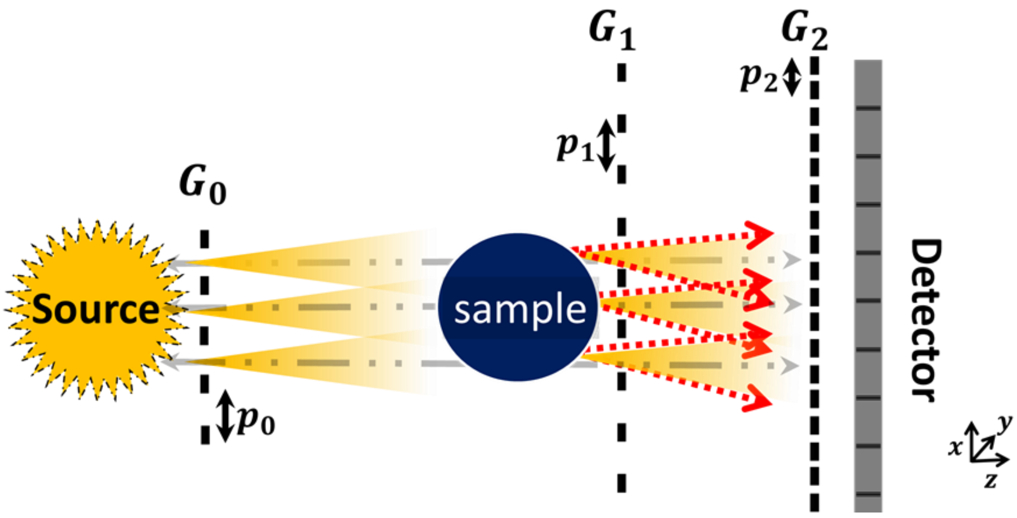

Figure 2-4 A schematic of a grating interferometer in the Talbot-Lau configuration consisting of three gratings, the beam splitter, G_0, the phase grating, G_1, and the absorption grating, G_2.

If G_2 is scanned in a step-wise fashion in the direction orthogonal to the grating lines, with steps smaller than the grating period, each pixel records a sinusoidal intensity variation, known as a phase-stepping curve. In the presence of a phase object, refraction causes a transverse shift in the detected fringe pattern. This shift can be quantified by taking images at several displacements of G_2:

$$I(m,n) \approx a_0(m,n) + a_1(m,n)\cos\left(\frac{2\pi x_g}{p_2} + \phi(m,n)\right), \tag{2-6}$$

where a_0 and a_1 are Fourier coefficients, x_g is the displacement of G_2 and m and n represent spatial frequencies. In principle, three images are sufficient to retrieve the absorption, refraction and dark-field signals by tracking the changes to the phase stepping curve caused by a sample [Pelliccia et al. 2013]. However, in practice, 6-40 images are usually acquired at regularly spaced points of the phase stepping curve, in order to accurately track the changes imposed by a sample. A single-shot approach exists, where a single interferogram obtained at one grating displacement position is analysed in the Fourier domain. Since this approach requires no motion of the gratings, it reduces the error associated with grating movement, reduces the exposure time, and can potentially reduce the dose received by the object. However, the images produced in single-shot mode have a significantly lower spatial resolution than those produced by phase stepping. A hybrid method combining the phase stepping and Fourier analysis techniques has also been proposed [Nagai 2014].

GI is a DPI technique similar to ABI, as it also enables extracting USAXS information from the object, although the tolerance to less monochromatic beams is significantly improved compared to the Bonse-Hart or ABI set-ups. However, the gratings are manufactured with pitches of only a few μm, which makes them difficult to fabricate for applications requiring large fields of view. It also means that they need to be aligned with sub-micron precision. This is a possible hindrance to its potential use in “real-world” applications, but this can be remedied as grating fabrication improves. In light of this, Miao et al removed the need for mechanical motion of the gratings, replacing it with a movement of the focal spot through electronic beam scanning [Miao et al. 2013].

2.3 Edge Illumination Phase Contrast imaging

2.3.1 The edge-illumination method

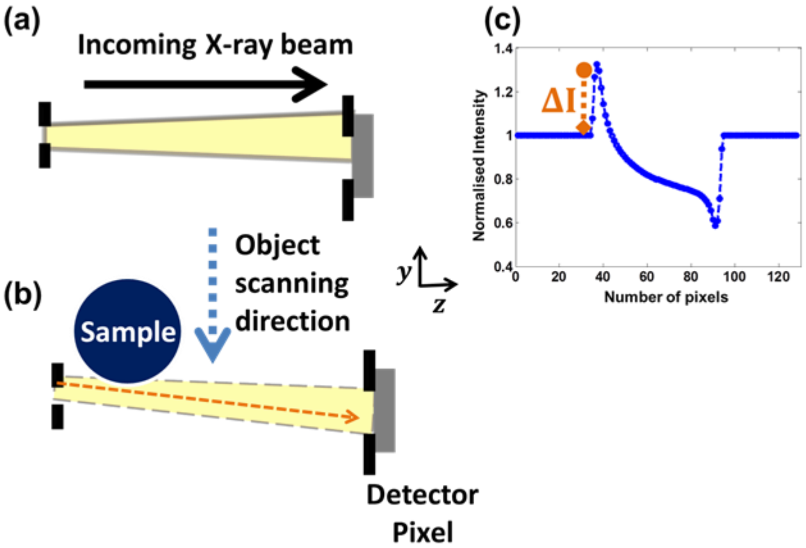

Figure 2-5 (a) A basic (e.g. scanning, synchrotron based) edge-illumination set-up where a beam is defined by the first aperture and aligned with an absorbing edge. When an object is scanned immediately downstream of the first aperture (b), refraction changes the proportion of the beam incident on the detector pixel. A profile of the object is shown in (c).

Edge Illumination (EI) is a non-interferometric XPCI technique that was invented at synchrotron facilities in the late-90s, where it was also first used [Olivo et al. 2001]. A pair of apertures suffices to implement the technique. The first aperture is placed at some distance from the source and collimates the incident X-ray beam. The second aperture is placed just before the detector, such that it partially obscures a row of pixels, leaving only the centre uncovered (see Figure 2-5(a)). A partial vertical offset of the two slits fulfils the so-called ‘‘edge-illumination condition’’, i.e. the beam straddles one of the edges of the aperture placed on the detector. In the presence of an object, refraction changes the proportion of the beam incident on the pixel, and hence the intensity recorded by the pixel (see Figure 2-5(b) and (c)). To obtain a full image, the object must be vertically scanned, which produces a mixed intensity profile containing both differential phase (i.e. refraction) and absorption signals.

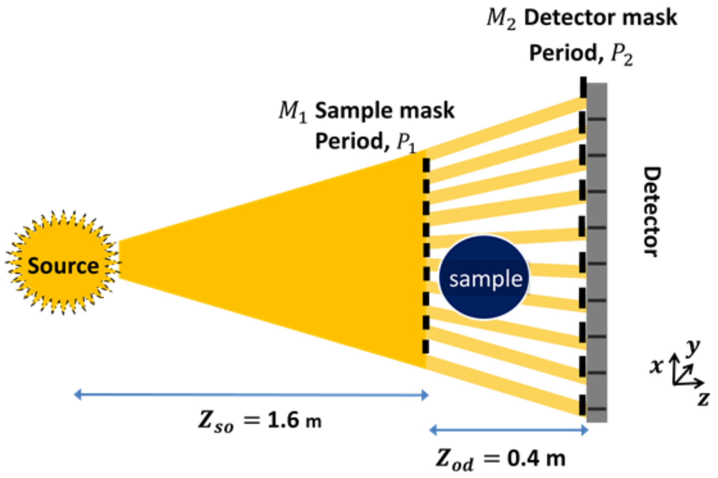

Figure 2-6 A schematic of the laboratory edge illumination configuration consisting of two periodic masks: the pre-sample mask, M_1, and the detector mask, M_2.

EI was later adapted to large focal spot, conventional sources [Olivo & Speller 2006]. Since it is a non-interferometric technique, it imposes almost no coherence requirements on the source and can be performed without the need for source segmentation, as used by e.g. GI, making it possible to use large focal spot tube sources with no additional collimation. In the laboratory case, scanning large objects can become time consuming because lab sources are orders of magnitude less intense than synchrotron sources. In order to rectify this, the EI principle was applied to multiple detector pixels simultaneously by replacing the apertures with two sets of periodic masks. This is the standard lab-based EI system (Figure 2-6).

The first mask, M_1, has a period P_1, and is known as the pre-sample mask. It defines a set of individual beamlets which are incident upon the second mask, M_2. This is known as the detector mask and has a period P_2. The detector mask is placed just before the detector to partially intercept the beamlets. The ratios between the mask periods are such that $P_2 = P_1 \times m$, where m is the geometric magnification factor defined as $\frac{Z_{so}+Z_{od}}{Z_{so}}$. Z_{so} is the source-to-object distance and Z_{od} is the object-to-detector distance. The mask periods used in EI are typically an order of magnitude greater than those used in GI, which means that beamlets from adjacent apertures do not interfere. As well as making EI less sensitive to misalignments and mechanical vibrations than other XPCI methods, this also makes the masks easier to manufacture and more easily scalable to large fields of view.

EI is a powerful non-interferometric technique which counts among its main advantages relaxed mask alignment requirements [Millard et al. 2013], reduced dose to the sample, lack of source coherence restrictions, [Olivo & Speller 2007; Diemoz & Olivo 2014] and achromaticity [Diemoz & Olivo 2014; Endrizzi et al. 2015a]. Although the standard EI set-up does not possess the simplicity of FSP, it has been demonstrated that the strength of the recorded phase contrast signal is less affected by larger source sizes. A direct comparison showed that while the FSP signal steadily decreases with increasing source size, EI is not significantly disadvantaged until after a source $FWHM$ of $\sim 100\mu m$ [Olivo et al. 2001; Olivo & Speller 2007; Peterzol et al. 2005].

2.3.2 Dithering

In the full field EI set-up shown in Figure 2-6, some (sub-pixels sized) parts of the sample remain invisible to the pre-defined beamlets. These regions can be seen in a composite image of the sample, which is comprised of many images taken at several sub-pixel steps and stitched together, thereby increasing the sampling of the object, although it is not always necessary to do so [Olivo et al. 2013]. This process is called dithering.

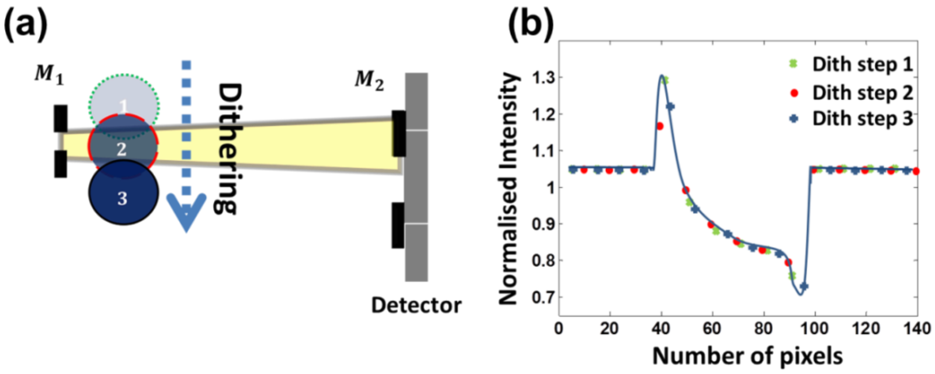

Figure 2-7(a) Demonstration of the dithering procedure over a single set of apertures. The object is displaced in sub-pixel steps (from top to bottom), and an image is acquired at each position. (b) shows the simulated differential phase profile of the wire, which was composed by stitching together multiple dithering steps

Figure 2-7 shows how dithering is achieved for a small feature scanned downstream of a single set of pre-sample apertures. An image is acquired at each of the three sub-pixel positions shown in Figure 2-7(a), and the resulting images are stitched together. Note that the size of each dithering step has been exaggerated in the figure for the ease of display. The differential phase profile of a wire in Figure 2-7(b) was acquired with the full field EI system. It highlights the importance of increased sampling schemes for DPI techniques, especially at the edges of the detail where refraction is largest. An adequately sampled refraction peak can be crucial to correctly retrieving an integrated phase image. Ultimately, in the typical EI set-ups which are used in this work, the spatial resolution of the system in the direction orthogonal to the mask lines is ultimately determined by the sample aperture, while in the parallel direction it is limited by the source blurring and pixel size [Diemoz et al. 2014].

2.3.3 Phase and absorption retrieval

EI produces “raw” images in which absorption and refraction information are entangled. However, these two complementary channels can be separated via a quantitative phase retrieval algorithm. The first of its kind for EI was developed by Munro et al. and inspired by the original Chapman DEI algorithm [Munro et al. 2012; Chapman et al. 1997]. In a similar fashion, it makes use of two images, each of which is acquired with a different position of the pre-sample mask, as shown in Figure 2-8.

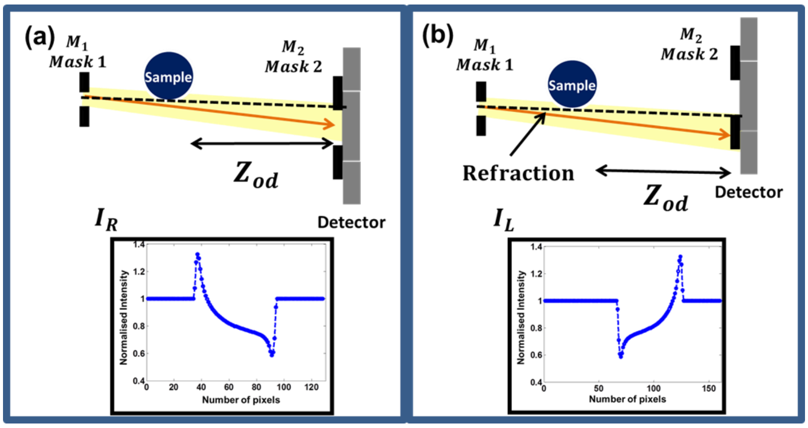

Figure 2-8 Two images are acquired with two different configurations of the system. In (a), the pre-sample aperture is aligned with the top edge of the detector aperture and downward refraction causes an increase in the recorded intensity. In (b) the pre-sample aperture is aligned with the bottom edge of the detector one, and the same refraction causes a decrease in the measured intensity.

Once again, we focus on single set of apertures to simplify the explanation, while emphasising the alignment of the beam with the top and bottom edges of the aperture in the detector mask, respectively. In full field EI, since the masks are periodic, when they are correctly aligned, the same placement of the beam is replicated for all apertures.

Figure 2-8(a) shows the beam aligned with the top edge of the detector aperture, and the downward refraction represented in the figure causes an increase in the measured intensity. In Figure 2-8(b), the beam is aligned with the bottom edge, but now the same refraction causes a decrease in the measured intensity. The profiles shown at the bottom of each figure reflect the inverse nature of these two signals. It is evident that, while the refraction signal is reversed, the absorption signal remains the same. Therefore, the two images can be algebraically combined to retrieve the separate refraction and absorption signals. This led to the following expression for differential phase retrieval with an extended source [Munro et al. 2012]:

$$\frac{\partial \phi}{\partial x} = \frac{\sigma\sqrt{\pi}}{2z_{so}}\frac{I_R - I_L}{I_R + I_L}, \tag{2-7}$$

where σ is the size of the source, I_R is the image taken in the first configuration and I_L is the one taken in the second. Later, algorithms were developed to extract dark-field information by acquiring a third image [Endrizzi et al. 2014].

2.4 Summary

In this chapter, a brief historical review of phase contrast imaging methods was presented. In particular, the edge illumination method is introduced, and a detailed description of its working principles was given. An early phase retrieval algorithm, which was inspired by the algorithms developed by Chapman et al, was also presented.

Chapter 3 Materials and Methods

3.1 Overview

The first part of this chapter outlines the experimental procedure used to measure the size of the X-ray source focal spot. In the next section, the two detectors used in this work (Anrad and Pixirad) are described. Finally, two simulation packages are introduced; each will be used to carry out investigations into novel EI set-ups in chapters 5 and 6. The first is based on a Monte Carlo ray-tracing programme called McXtrace, and the second is based on wave optics (Fresnel diffraction theory). All aspects of these packages that are pertinent to understanding the work presented in this thesis will be explained.

3.2 Source measurements

A polychromatic laboratory X-ray source (Rigaku HF007) was used in the EI set-ups featured in this work. The source utilises a rotating molybdenum target and was run at $35\ kVp$ and $25\ mA$ for all the experiments carried out in chapters 4, 5, and 6, with no added filtration. In order to accurately model the shape of this source in simulations, the focal spot size was measured experimentally using the edge response method along two orthogonal directions. This involved acquiring images of a sharp edge, which was placed approximately $5.6\ mm$ from the X-ray source. A photon counting detector with a cadmium telluride (CdTe) CMOS sensor and $100\ \mu m$ square pixels (XCounter) was placed $202\ mm$ downstream of the edge to collect the images. Thus, a high magnification set-up was realised, the geometry of which has been schematised in Figure 3-1.

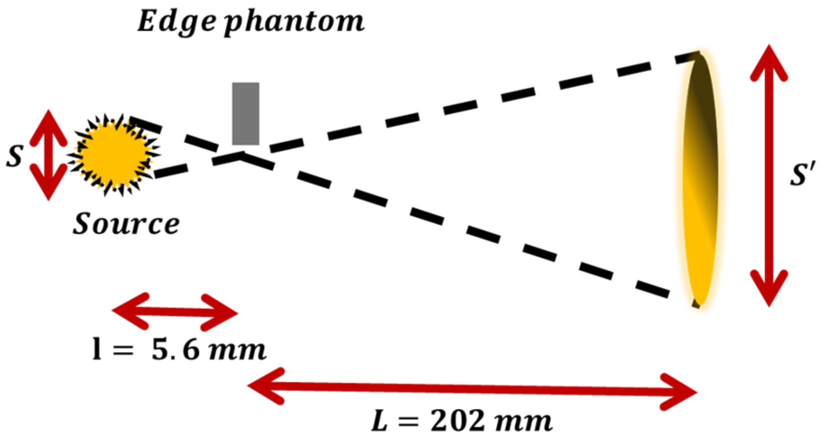

Figure 3-1 Schematic of the source size measurement using the edge response method.

The set-up depicted in Figure 3-1 illustrates that the image of the edge collected at the detector plane is blurred and magnified as a result of the geometry of the source, as well as the distances used. In fact, the high system magnification renders contributions to image blurring from the detector point-spread function (PSF) negligible such that, by considering only the system magnification, the size of the focal spot at the source plane can be directly calculated as follows:

$$s = \frac{l}{L} \times S. \tag{3-1}$$

In the above equation, s is the focal spot size at the source plane, l is the distance between the source and the edge, L is the distance between the edge and the detector, and finally, S is the focal spot size at the detector.

Figure 3-2(a) and Figure 3-2(b) show the profiles taken along the two edges, which were oriented along two orthogonal directions, respectively.

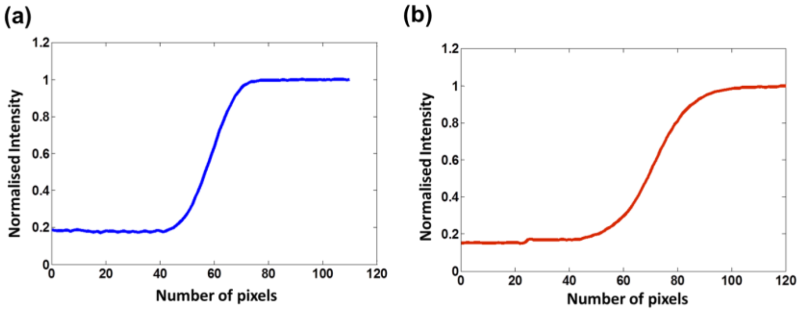

Figure 3-2(a) The profile is extracted in the direction orthogonal to the edge when it was oriented in the vertical direction, and (b) the horizontal direction.

The profiles shown in Figure 3-2(a) and (b) are known as edge-response-functions (ERFs), and their derivative result in line-spread-functions (LSFs), which may be mathematically expressed as a convolution between the source and the edge. The LSFs were then fitted using the MATLAB curve fitting tool, which allows the user to create custom fitting functions. It was assumed that the source could be well approximated by a Gaussian, such that its analytic fitting function was defined as:

$$\mathrm{G}_1 = Ae^{\frac{-x^2}{\sigma^2}}, \tag{3-2}$$

where A is the amplitude and σ is the standard deviation of the Gaussian. The amplitude represents the peak intensity value of the focal spot, while the standard deviation is proportional to the full width at half maximum (FWHM) of the focal spot.

The model was then fitted to the experimental data, and the curves are shown in Figure 3-3. The good agreement observed in this figure shows that the Gaussian approximation for the shape of the source is acceptable. The standard deviation of each fit was then extracted and used to calculate the FWHM of the curve. Thus, the source was calculated to be $50\,\mu m$ and $70\,\mu m$, in the horizontal (x) and vertical directions (y), respectively.

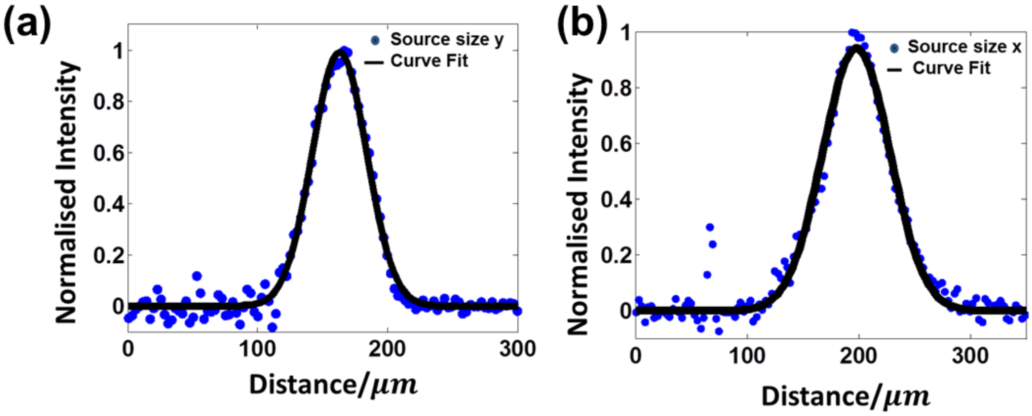

Figure 3-3 The measured source size in (a) the y-direction and (b) the x-direction.

To model the spectral output of the source, a measurement of its spectrum, performed at $35\ kVp$, was provided by the manufacturers. The data acquired by the manufacturers has been shown to match the spectrum calculated numerically from the data obtained by Boone et al [Boone et al. 1997], which is important since it allows us to make the assumption that the spectral data collected by Boone et al at other $kVps$ may be used as an accurate description of this polychromatic source.

3.3 Detectors

3.3.1 ANRAD

The Anrad SMAM flat panel detector was used in chapters 5 & 6. It is a direct converter (amorphous selenium, a-Se) with a pixel size of $85\ \mu m$, and, to first approximation, a linear energy response. It has been characterised and modelled by Millard et al [Millard et al. 2014], who obtained a good agreement between experimental and simulated data. The model developed by Millard et al was adapted to a wave optics simulation package and modified to include the PSF in chapters 5.

The PSF of the detector had been acquired in a previous measurement, and it will be presented, as well as an analytic expression which is used to perform its fitting.

3.3.2 PixiRad

Pixirad is a photon counting detector with a CdTe sensor and energy discrimination capabilities. In this respect, it is similar to the XCounter detector, which was used in the previous section to perform the source measurements. However, in comparison to XCounter, Pixirad possesses smaller pixels ($62\ \mu m$); this increases the likelihood of charge sharing between adjacent pixels. Indeed, the charge sharing effect occurs when the electric charge generated by an incident photon within one pixel diffuses into its neighbours as a result of coulomb repulsion and diffusion. Thus, the signal from a single event is recorded in multiple times in adjacent pixels as separate events. To eliminate these erroneous signals, the Pixirad detector was designed with a winner-take-all mechanism, which, when implemented, analyses the charge collected by a small array of pixels and assigns the event exclusively to the pixel with the largest signal. This also potentially leads to a more ideal, box-shaped pixel PSF, which may benefit future EI set-ups. The extent of this benefit is briefly discussed in chapter 5.

In addition, each pixel has two energy thresholds, meaning that photons can be sorted into two energy bins, thus enabling dual-energy imaging. The Peltier effect is used to cool the detector to temperatures below zero, thereby eliminating the detector dark current. While Pixirad-2 has not yet been characterised, the necessary measurements have been performed with its predecessor, Pixirad-1 and are described extensively in previous works [Bellazzini et al. 2013; Vincenzi et al. 2015; Delogu et al. 2016].

In chapter 4, the detector is used in an experiment designed to study and optimise the sensitivity of the EI set-up by making use of its increased efficiency, compared to the Anrad detector. While, many of the features of Pixirad are not used in this work, they may be beneficial in future implementations of EI set-ups.

3.4 Simulations

During the course of this work, simulations are used to test, inform and improve experimental procedures, as well as to verify experimental results. Simulations are also crucial to designing experiments, and performing additional investigations, which may be impractical to pursue experimentally, due to time or other practical constraints. Therefore, flexible and reliable simulations are critical to the development of novel EI set-ups and future experimentation.

Two simulation packages have been independently developed by Vittoria et al and Millard et al, respectively, and were used during the course of this work. One is based on the formal wave description of X-rays, and the other on a Monte Carlo ray tracing approach. The former makes use of the Fresnel-Kirchhoff diffraction integral, which provides a means for calculating the complex wave field that is detected at an arbitrary plane, after some propagation, for a known initial field. The calculation of this resultant field is expressed within the integral as a convolution between the initial field and a propagator term. In contrast, the Monte Carlo method utilises geometrical (ray) optics, which assumes that waves can be modelled as a collection of narrow beams that travel in straight lines through a medium. Snell's law can then be used to calculate new ray trajectories at the interfaces between different media. Thus, the ray is incrementally advanced along its path until it is either fully absorbed or detected.

For both methods, absorption and refraction effects can be correctly modelled; however, diffraction and interference effects, which are exclusively wave related phenomena, cannot be modelled by the ray tracing method. Nonetheless, it is important to understand that the two simulations are essentially equivalent, since geometrical and wave optics produce the same results under certain conditions. Generally speaking, the former has been shown to be an approximation of the latter in previous works [Peterzol et al. 2005; Munro et al. 2010]. Hence, the decision as to which one to use when performing a given task is based only on its suitability and convenience. As a result, established models of the standard double-mask EI set-up, which had already been experimentally validated [Millard et al. 2014; Vittoria et al. 2013], were adapted and used to simulate two new EI set-ups.

3.4.1 Wave Optics

The standard EI set-up can be described as a series of free-space propagations of X-rays interspersed with interactions with the complex transmission functions of EI masks and samples. Using the Fresnel-Kirchhoff diffraction theory, this is then translated into an intensity variation measured by a detector [Vittoria et al. 2013]. The simulation is run through MATLAB, which is also used to read and analyse the results. As a simulation method, it is fast and not computationally intensive.

Figure 3-4 A simulated sapphire wire generated using the model of a full-field laboratory EI set-up with the wave optics package. The image is comprised of 32 dithering steps.

The simulated images generated from the wave optics simulation, such as the one shown in Figure 3-4, are completely noise-free, which therefore allows the user to add the type and level of noise to the simulated data in a successive step. In addition, it is also easy to incorporate the detector PSF into the simulation. This is done in a simple and effective way through a convolution between an ideal pixel and a user defined function, which in this case was a Gaussian. For these reasons, the wave optics simulation was used to model the novel EI set-up introduced in chapter 5, as well as its sensitivity as a function of the pixel PSF. In that chapter, a detailed outline of the modifications made to the set-up in the simulation code will also be given.

3.4.2 McXtrace

McXtrace is a Monte Carlo ray-tracing software package, which was built upon the McStas ray-tracing tool for neutron beams. It is written in its own meta-language and possesses a modular structure, which makes it easier to create interfaces for other simulation software. A detailed description of this simulation package can be found in its programme manual and in Knudsen et al. [Knudsen et al. 2013]. Here, a basic outline of its working principles is presented, which is necessary to understand the work done in chapter 6.

The aim of McXtrace is to model beamlines and other set-ups which, due to their complexity, cannot be easily described using analytical models. It achieves this goal by replacing deterministic interactions with probabilistic events, and allows users to model objects individually and then to combine them to model complex systems.

McXtrace consists of three layers, two of which can be modified by the user, and a third which is not directly accessible. Models of the individual objects which make up the beamline/set-up are implemented in the first of two modifiable layers. These include X-ray sources, samples, other optical components and detectors. In the McXtrace language they are referred to as "*components*", which are in turn made up of functions. Functions are embedded in *components* and can determine their physical characteristics, as well as dictate the changes experienced by photon after interacting with a specific *componen*t.

The second modifiable layer is used for the implementation of "*instruments*". These contain the appropriate combination of *components* needed to simulate the overall effect of a set-up. Absolute and relative spatial positions, object dimensions and orientation in space can all be specified within this level. One advantage of the *instrument* file, which is relevant to this work, is that *components* can be manipulated in 3D space in a relatively simple manner, without the need to modify the code in the levels below, or to recalculate the geometry of the interactions. For example, within an instrument, the command, "AT (x, y, z) ABSOLUTE" determines the absolute position of a component, while “AT (x, y, z) RELATIVE TO” places a *component* relative to a reference point or to another *component* in the set-up. Similarly, “ROTATED (ϕ_x, ϕ_y, ϕ_z)” can be used to reorient components in space, either in absolute (with respect to the origin) or relative terms. Moreover, these changes are automatically taken into account at the lower levels of the simulation, i.e. within the functions.

The final layer of McXtrace is generated when the McXtrace programme itself reads and parses the *instrument* and *components* to create an executable programme, where the ray-tracing calculations are performed. One advantage of keeping this section hidden is that it is compiled and optimised for each machine, independent of the code written within *instruments* or *components*. When the simulation is run, numerical photons are generated and assigned an initial state and weight based on input parameters, i.e. the conditions set for the X-ray source. This state is then modified by each component the photons encounters, until they are either absorbed or detected.

In order to simulate the EI set-up, some of the standard McXtrace *components* were modified by Millard et al, and were used to create EI specific *instruments*. For example, masks are defined as periodic transmitting and semi-opaque regions [Millard et al. 2014, Millard et al. 2015]. When a photon travels through the set-up, a function determines whether it passes through the aperture, or if it is intercepted by the mask septa. In the latter case, the septa material properties are used to calculate the proportion of the photons attenuated.

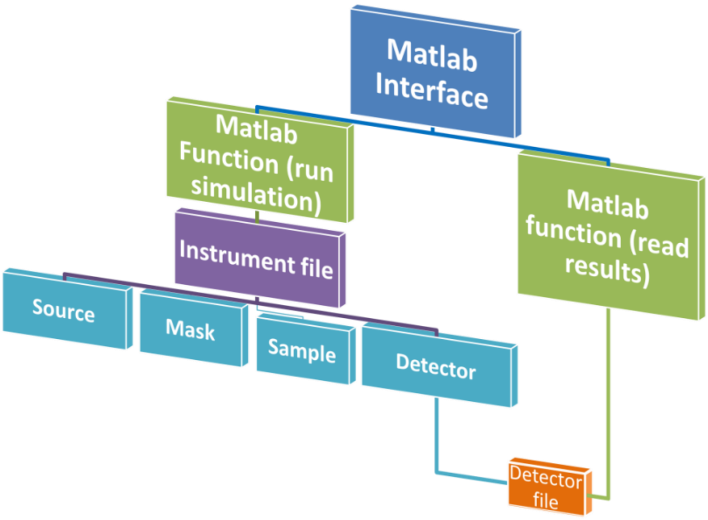

Figure 3-5 Hierarchy of operation for simulating the EI set-up using McXtrace.

Additionally, in order to automate the acquisition of image sequences with McXtrace, and also to facilitate data analysis using a more widely available and user friendly platform, a MATLAB interface was added to the previously described McXtrace hierarchy. A representation of the new hierarchy is shown in Figure 3-5. The MATLAB interface now sits at the top, with one of its functions driving the Monte Carlo simulations and another reading the results. The desired parameters, e.g. number of dithering steps, source spectrum, number of photons etc. can all be set from within MATLAB, and are then sent as a series of strings to the *instrument*, where they are compiled into an executable. Furthermore, using MATLAB for data acquisition and analysis in the simulation mimics the experimental procedures used in this work, i.e. that data acquisition or analysis procedures can be written and tested with the simulation, and then be automatically applied to the experimental case.

Finally, at the backend, another MATLAB function reads the detector files and converts the final “weight” of the photons collected in each pixel into a grayscale image. The Anrad SMAM flat panel was used in the simulation and experiment because it had been previously characterised by Millard et al [Millard et al. 2014], who also obtained an excellent match between the two.

The McXtrace package has been used in chapter 6 to model an EI set-up which employed L-shaped masks to achieve two-directional refraction sensitivity. An implementation of the model, which included the L-shaped masks, was used to study the shape of an illumination curve produced by these masks before undertaking experimental work, and also to investigate the effect on the recorded intensity patterns for a given misalignment of the two masks. The goal was to understand the general trend that images without the sample would show as a function of a misalignment of the various spatial parameters. This was key to reducing the time spent in the laboratory performing live alignments.

3.5 Summary

In this chapter, the focal spot size was measured along its x and y directions and was fitted with an analytic function. The FWHM was calculated along the two directions, and was determined to be $50\,\mu m$ and $70\,\mu m$ respectively. These measurements will be used to model the XPCI set-ups in the simulations in chapters 5 and 6. Additionally, a photon counting detector was used for the experiments performed in chapter 4, and a direct converter A-Se detector was used for the experiments performed in chapters 5 and 6; both of these instruments were briefly described.

Moreover, two simulation packages have been adapted for the purposes of this work. The first is a wave-optics package based on Fresnel-Kirchhoff diffraction theory. This was used to simulate a single-mask EI set-up in chapter 5, and to study the effects of the detector PSF on the set-up. The second package uses a Monte Carlo approach, where the path of an individual photon is followed as it traverses the various elements in the set-up. Weights are assigned to each ray according to the attenuation it suffers, and its trajectory can be changed according to the refraction it undergoes, due to its interaction with various *components* (calculated via Snell's law).

In the lab set-up, Fresnel-Kirchhoff diffraction theory and geometrical optics have been shown to be valid descriptions of the EI set-up and its physical principles. However, despite the equivalence of the two simulations, in some cases, certain features are more easily implemented with one method or the other. For example, each image generated by the Monte Carlo approach possesses an inherent level of the noise; to reduce this noise, more photons must be generated, which increases the computing time and the computational power needed. On the contrary, the wave optics model produces noiseless images, which make it easier to investigate image noise in a fast and efficient manner, since this can be added retrospectively. However, the Monte Carlo simulation is flexible and optical elements can be easily manipulated in 3D space. This could also be used to build a 3D model of the masks in the future; however, in this work the 2D model has proven sufficient in describing the system since a good agreement was found in all cases with the experimental results.

Chapter 4 Edge Illumination Phase Contrast Sensitivity

4.1 Overview

In this chapter the standard (double mask) EI sensitivity is studied as a function of sample mask displacement position. First, a metric called the illumination curve (IC) is introduced. It characterises the EI system and relates the changes in detected intensity to the refraction angle of the beam. This leads both to a simple quantitative phase retrieval algorithm and to a model capable of predicting the system sensitivity for a given set of experimental parameters. The approach used in this chapter was first developed by Diemoz et al [Diemoz et al. 2013a], but will be revisited here as it forms the basis for the experimental work.

The aim of this study was to experimentally verify an established model for phase retrieval, and also to determine the optimal sensitivity of the EI set-up under two constraining conditions: the time limited case and the dose limited case. The first experiment investigates the optimal sensitivity of the set-up when the time available to acquire images is limited. This situation may be encountered in clinical or real-world settings. Similarly, the second case is a problem mainly encountered at synchrotron facilities, or when using of powerful X-ray sources, which can risk oversaturating imaging detectors. In such cases, when a single long exposure is not practical, it is necessary to investigate the optimal sensitivity that can be achieved by combining a number of shorter exposures to achieve equivalent statistics.

4.2 The Illumination Curve (IC)

The standard EI configuration consists of two masks which are displaced by a fraction of the aperture width in the direction orthogonal to the apertures themselves in order to achieve phase contrast sensitivity (see Figure 2-6 and Figure 2-8). This misalignment is inversely proportional to the fraction of the pixel which is illuminated, i.e. the illuminated pixel fraction (IPF). It has been observed that changes in the IPF translate into changes in the EI signal [Olivo & Speller 2007]. As the misalignment decreases, the IPF increases and more photons impinge upon the pixel, thereby increasing the detected statistics in the obtained image. However, it also decreases the phase signal, i.e. the contrast. Conversely, when the IPF is reduced (larger misalignment) the contrast increases, and so does the noise due to reduced detected statistics, which makes the determination of the conditions providing maximum SNR non-trivial. In other words, since the position of the masks changes the quality of the signal, a study of the signal refraction as a function of IPF is needed in order to optimise the system performance.

An EI system is characterised by its (IC), which is analogous to the rocking curve in ABI. The IC is obtained by displacing either the sample or the detector mask over one period, and recording the intensity at each position. In practice, the sample mask is displaced while the detector mask is kept fixed. A key reason for this is that the PSF of most detectors is not flat, leading to a different response when the beam hits different parts of the pixel. The IC relates changes in intensity to changes in the displacement of the beam, and can be expressed as a function of sample mask position. A general expression for the IC, $L(x)$ is:

$$L(x) = Src\left(\frac{z_{od}}{z_{so}}x\right) * M_1(x) * M_2(x), \tag{4-1}$$

where $src\left(\frac{z_{od}}{z_{so}}x\right)$ represents the de-magnified source spatial distribution incident on the detector mask, and $M_n(x)$ represents the masks [Vittoria et al. 2013; Diemoz & Olivo 2014]. Figure 4-1 shows a typical IC, with insets schematising the degree of misalignment between the sample and detector masks used to achieve each particular IPF. At the position of maximum illumination, apertures in the detector mask are completely exposed to the beam because the masks are perfectly aligned, and the system has very little sensitivity to refraction. Conversely, certain positions on the IC lead to higher sensitivity for some signals (refraction, absorption, and dark-field).

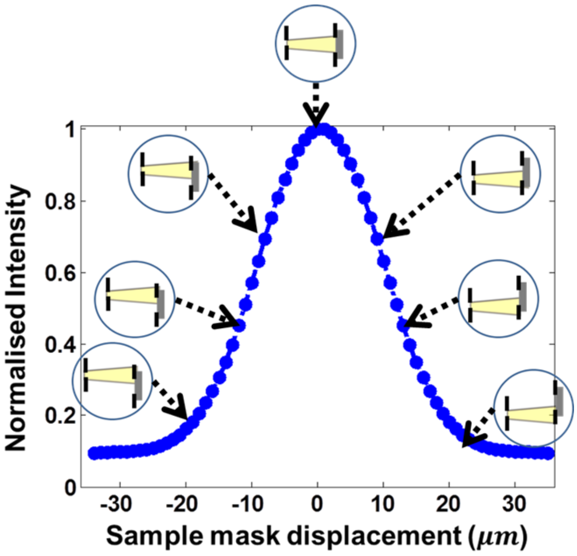

Figure 4-1 The illumination curve (IC) of the EI system is accompanied by illustrations depicting the misalignment between the sample and detector masks used to achieve a given illumination level.

In general, a single frame acquired at any one of the positions depicted on Figure 4-1 would contain a mixture of absorption, refraction and dark-field signals. In particular, images acquired at the top of the IC, for which the apertures are perfectly aligned, are most sensitive to the absorption signal; images acquired on the linear regions of either slope, for which the apertures are partially misaligned, are most sensitive to refraction. Finally, those images obtained near the tails of the IC, for which the apertures are almost completely misaligned, are mostly sensitive to the scattering signal. However, in practice, these three entangled signals can be separated by using a retrieval algorithm, which would require multiple frames to be acquired at different IC positions. The IC also enables a more intuitive representation of these three signals. For example, absorption can be represented as a reduction in the total area under the IC curve, refraction as a translation of the IC centre, and USAXS as a broadening of the IC. To disentangle these three signals, three separate frames need to be acquired, with the sample mask displaced to three different positions on the IC [Endrizzi et al. 2014]. These signals constitute three different channels of information, which can highlight different features within an object.

Since the sample is placed just after the sample mask and the thin object approximation is normally valid in most cases explored with our system, it is possible to relate the apparent translation of the sample mask, i.e. the beam displacement, which is caused by the presence of an object, to a given refraction angle. In other words, the IC can be used to calculate the refraction angle.

Figure 4-2(a) and (b) show how the refraction-induced change in intensity can be related to a particular beam displacement via the IC, while Figure 4-2(c) defines the geometry of the system. The intensity value I, due to refraction, can be written as a function of the sample mask position along the IC $L(x)$:

$$I = L\left(x \pm \overbrace{z_{od}\Delta\theta_{eff}}^{\Delta x}\right), \tag{4-2}$$

where the approximation $\tan(\Delta\theta) \approx \Delta\theta$, which is valid for small angles as is the case in X-ray refraction, was used, $\Delta\theta_{eff}$ is the effective refraction angle (i.e. the refraction angle at the effective energy of the set-up.

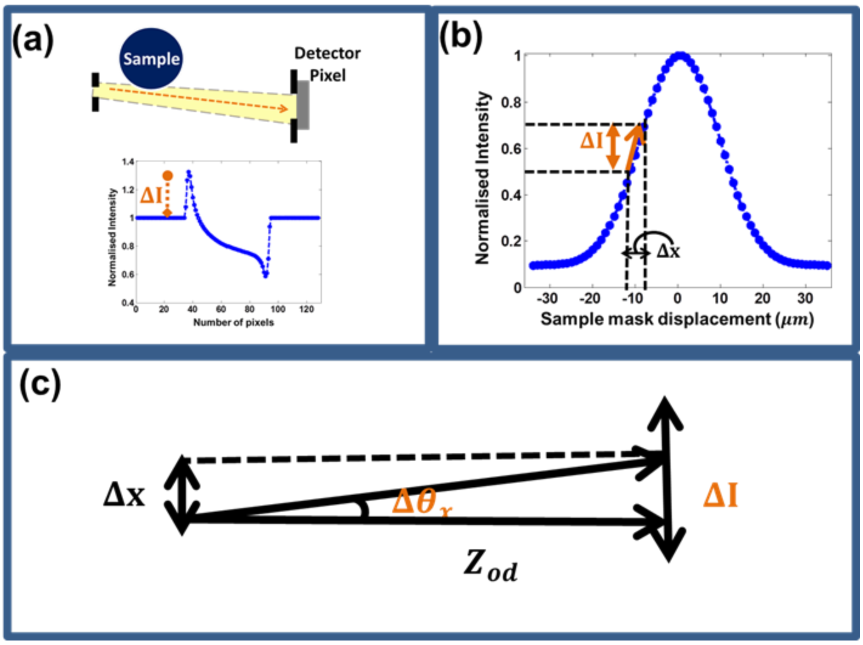

Figure 4-2 (a) shows how refraction from a phase object can increase the intensity measured by the pixel. In (b) the relationship between the intensity variation and a corresponding translation of the mask is shown and finally, (c) depicts the geometry of the set-up which allows for a calculation of the refraction angle.

While the IC relates the displacement of the beam at the detector mask to a change in intensity, the system magnification must be taken into account for refraction to be correctly retrieved. The expression in Eqn. (4-2) enables the description of mixed intensity images $I(x_{e_\pm})$ as a function of the sample mask position ($x_{e_\pm}$):

$$I(x_{e,\pm}) = I_0 T_{eff} L(x_{e,\pm} - z_{od}\Delta\theta_{eff}), \qquad \textbf{\textit{(4-3)}}$$

where I_0 is the intensity incident on the sample and, $x_{e\pm}$ is the position of the sample mask, and the positive (negative) subscript represents images taken on the right (left) hand side of the IC in Figure 4-2(b). Finally, T_{eff} and $\Delta\theta_{eff}$ are the effective object transmission and induced refraction angles, where the subscript “eff” is used to indicate that they are calculated by taking the weighted average over the source spectrum. It must be noted that the effective energy is not necessarily the same as the mean energy of the spectrum, and it can be different for phase and attenuation [Munro & Olivo 2013].

With the introduction of the IC, a phase retrieval algorithm similar to the one discussed in Chapter 2, section 2.3.3 can be derived. However, in this case, the algorithm explicitly takes into account the shape of the IC slopes. Here, the two images acquired on either side of the IC correspond to the two configurations shown in Figure 2-8, which lead to reversed refraction signals. The object transmission can be eliminated by taking the ratio of the two images in the following way:

$$\frac{I(x_{e,+})}{I(x_{e,-})} = \frac{L(x_{e,+} - z_{od}\Delta\theta_{eff})}{L(x_{e,-} - z_{od}\Delta\theta_{eff})} \equiv R(z_{od}\Delta\theta_{\mathrm{eff}}). \tag{4-4}$$

Eqn. (4-4) is an expression of the R-function. The refraction angle can then be calculated by inverting this function in the following way:

$$\Delta\theta_{eff} = \frac{1}{z_{od}} R^{-1}\left(\frac{I(x_{e,+})}{I(x_{e,-})}\right). \tag{4-5}$$

Eqn. (4-5) enables the derivation of an analytical expression which can be used to estimate the error on the refraction angle. For small statistical noise and symmetric imaging positions, i.e. $L(x_{e_+}) = L(x_{e_-})$, Diemoz et al calculated that the error on the refraction angle can be derived using standard error propagation, which yields the following expression [Diemoz et al. 2013a]:

$$\sigma(\Delta\theta_{eff}) \approx \frac{\sqrt{L(x_{e_+})}}{z_{od}\sqrt{2T_{eff}I_0}\left[L'(x_{e,+}) - L'(x_{e,+} + d)\right]}, \qquad \textbf{\textit{(4-6)}}$$

where $L'(x_{e,+})$ is the value of the IC gradient, which is related to the mask aperture size, d and to the shape and dimension of the focal spot.

Physically, it is easy to understand that a smaller aperture reduces the absolute number of photons impinging on the detector pixel, and therefore increases the noise (the term in the numerator). However, it also leads a steeper IC gradient, which increases the quantity in the denominator, thus decreasing the error. Eqn. (4-6) is an expression which enables an estimation of the sensitivity of any EI system given these system parameters. It is important to note, however, that the periods of the masks do not appear in the expression for $\sigma(\Delta\theta)$ as they do instead for GI [Modregger et al. 2011]. The sensitivity represents the smallest detectible refraction angle that is distinguishable from the image noise.

By relying on the IC based description, we have a means for explaining the initial observation made by Olivo & Speller [Olivo & Speller 2007], according to which the contrast increases with decreasing IPF.

Consider images acquired at two positions on the IC, one near the top and the other near the tail. Let’s assume for simplicity that, to first approximation, the positions are selected so that the gradient at both points is equal, and therefore refraction induces an equal change in intensity for both images, i.e. $\Delta I_1 = \Delta I_2$. However, when contrast is calculated, the images are normalised by their respective background illumination levels. In that case, $\frac{\Delta I_1}{I_1} > \frac{\Delta I_2}{I_2}$, because $I_1 < \mathrm{I}_2$. Hence, the contrast for images acquired at lower IPFs is larger than for higher IPFs. In the real case, the gradient will also vary, meaning the change in contrast does not simply scale with the background illumination, but is also modulated by the shape of the IC.

4.3 Experimental measurement of refraction sensitivity in EI

4.3.1 The Experimental set-up

The sensitivity of an EI system has been measured at both synchrotron and laboratory environments [Diemoz et al. 2013a; Diemoz et al. 2013b] and was shown to be comparable to GI. In a previous study conducted in the lab, a value of $\sigma(\Delta\theta) = 270 \pm 5\,nrad$ was obtained for images acquired at 50% illumination level with the Anrad detector described in Chapter 3 [Diemoz et al. 2013a]. However, this does not constitute the ultimate limit for the sensitivity achievable with a lab-based EI system.

As discussed above, Eqn. (4-6) shows that the position on the IC changes the system sensitivity. In order to study this effect in detail and to ultimately improve the refraction sensitivity, a new set-up was designed using line-skipped masks i.e. masks which illuminate every other pixel column, combined with a photon counting detector.

Line-skipping is usually employed to reduce the effects of high pixel cross-talk. However, since the PixiRad detector does not suffer from this effect, line-skipping was not, strictly speaking, necessary for this set-up. As such, future EI implementation that utilise the PixiRad detector could double the object sampling by using standard (i.e. non line-skipped) masks. In fact, line-skipping was only used here to match the periods of the sample and detector mask ($79\,\mu m$ and $98\,\mu m,$ respectively) to a multiple of the detector pixel pitch. The masks also had aperture sizes of $10\,\mu m$ and $16\,\mu m$ and a gold septa thickness of $\sim 150\,\mu m$, making them approximately five times thicker than those used in the first lab-based sensitivity experiments. These parameters were selected to reduce unwanted transmission through the mask and to reduce the size of the beamlets while maintaining a high photon flux.

Transmission can increase the baseline of the IC, which subsequently increases the inaccuracy of the retrieved refraction angle, and affects the sensitivity as it reduces the gradient of the slope. Additionally, it increases background noise because the photons transmitted through the mask septa are not considered in the retrieval algorithm and provide no useful information. A more detailed discussion of the inaccuracies introduced on the retrieved phase contrast signal as a result of using thin masks is provided in Chapter 5.

A diagram of the table-top experimental set-up is shown below. The sample and detector masks were each first independently aligned with the detector pixels, i.e. each one was removed in turn while the other was aligned. Finally, they were introduced simultaneously and were finely aligned with respect to each other and to the detector. After this fine adjustment, the sample and detector masks and the detector are placed at distances of $Z_1 = 1.57\,m$, $Z_2 = 0.36\,m$ and $Z_3 = 0.52\,m$ from the X-ray source, respectively; this was done in order to match the mask periods to twice the pitch of the detector pixels. Finally, the source is operated at $35\,kVp,$ $25\ mA$.

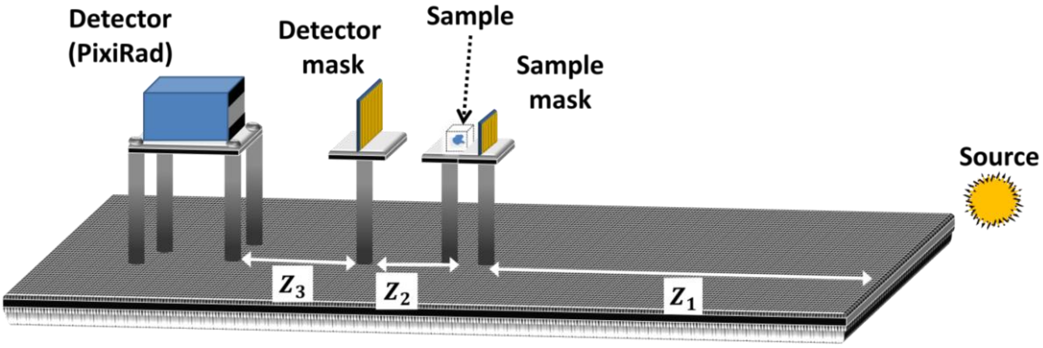

Figure 4-3 A schematic of the EI set-up used to study the refraction sensitivity. The sample mask was placed at a distance of $Z_1 = 1.57\,m$, away from the source; the detector mask and detectors were then placed at distances $Z_2 = 0.36m$, and $Z_3 = 0.52\,m$ away from the sample mask, respectively. The final distance was added in order to match the mask periods to twice the pitch of the detector pixels.

Figure 4-3 constitutes an atypical set-up because the EI masks, as well as having a “skipped” design as discussed above, were designed with periods only slightly smaller than the pixel size of the Pixirad detector ($62\,\mu m \times 2$). Hence, in order to match the magnified periods of the masks to a multiple of the detector pixel pitch, the detector was placed $0.52\,m$ away from the detector mask. In the usual EI set-up, the detector mask and detector are placed as close to each other as physically possible. In the double mask EI set-up this does not pose a problem as long as the IC is measured in the same configuration in which the images are obtained.

A picture of the first sample that was imaged, which consisted of five wires mounted on a metal frame, is shown in Figure 4-4. Wires were chosen because they represent a simple geometry, which can be easily replicated in simulations and used to verify the quantitative accuracy of the phase retrieval algorithm. Later, an image of a biological sample (insect leg) will also be presented.

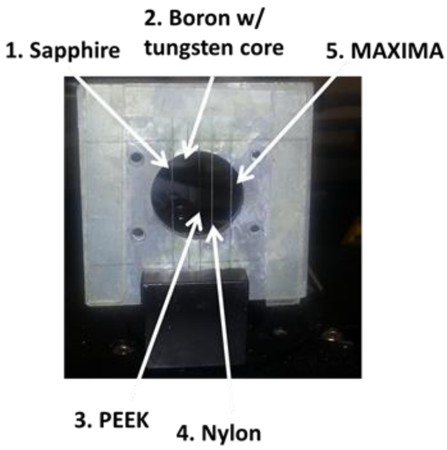

Figure 4-4 The wire sample consisting of five wires [1. Sapphire (radius =$130\ \mu m$), 2. Boron w\tungsten core (B radius= $100\ \mu m$, W core radius = $7\ \mu m$), 3. PEEK (radius = $50\ \mu m$), 4. Nylon (radius = $70\ \mu m$), 5. MAXIMA (radius = $150\ \mu m$)]. The latter is a trademark mix of plastic materials used in the manufacturing of fishing lines.

Images were acquired at the ten positions shown by insets on the experimentally measured IC shown in Figure 4-5.

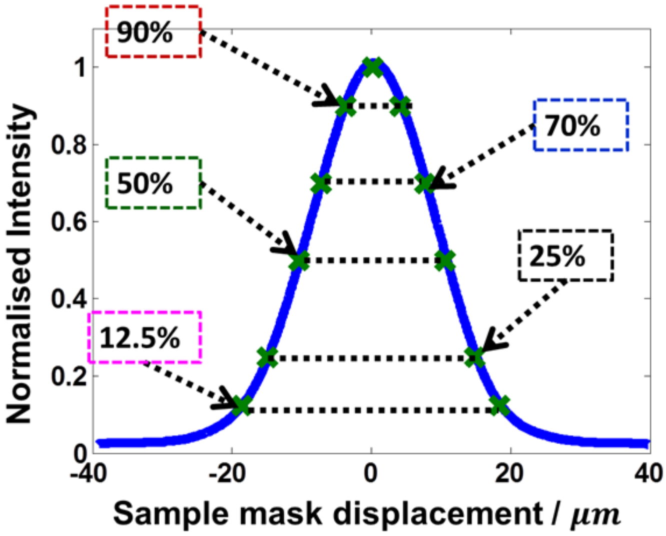

Figure 4-5 An annotated IC with insets showing the IPFs at which the images were acquired.

The positions correspond to sample mask displacements (IPFs) of $\sim \pm 5\ \mu m(\ 90\%)$, $\pm 7\ \mu m(\ 70\%)$, $\pm 11\ \mu m(\ 50\%)$, $\pm 15\ \mu m(\ 25\%)$ & $\pm\ 18\ \mu m\ (12.5\%)$. Seven frames, each with an exposure time of $3.5\ s$, were acquired at each sample mask position. In addition, the spatial resolution of the image was artificially increased by using 8 dithering steps (step size $= 9.8\ \mu m$). As previously mentioned, the purpose of this study was to determine the position of maximum sensitivity (minimum $\sigma(\Delta\theta)$). Hence, phase retrieval was performed for each symmetric pair of images and the standard deviation of the background of the retrieved image was measured, which represents noise in the retrieved refraction angles. Two separate investigations were undertaken, which can be referred to as "sensitivity at constant exposure time" and "sensitivity at constant detected counts". The first compares the sensitivity obtained at different IPFs for the same exposure time. To enable a direct comparison with the previous sensitivity study performed only at 50%, which used an exposure time of $7\ s$ per frame, two frames obtained with exposure times of $3.5\ s$ were combined at each imaging position.

In the second investigation, the mean background count at each IPF was matched to the mean background count in one frame at 90% IPF. This match was achieved by combining an accordingly larger number of frames at the lower IPFs. Since the number of frames is a discrete quantity and the ratio between the counts is typically non-discreet, the whole number of frames resulting in the total statistics closest to the desired one was used.

In order to perform phase retrieval for each symmetric pair of images according to Eqn. (4-4), the R-function was calculated at each position. This is given by the ratio of the two "arms" (left and right) of the IC at each IPF, which also ensures that the intensity value in the background of the R-images (ratio of I_+ and I_-) was equal to unity. The R-function curves were calculated at the various IPFs and are plotted in Figure 4-6.

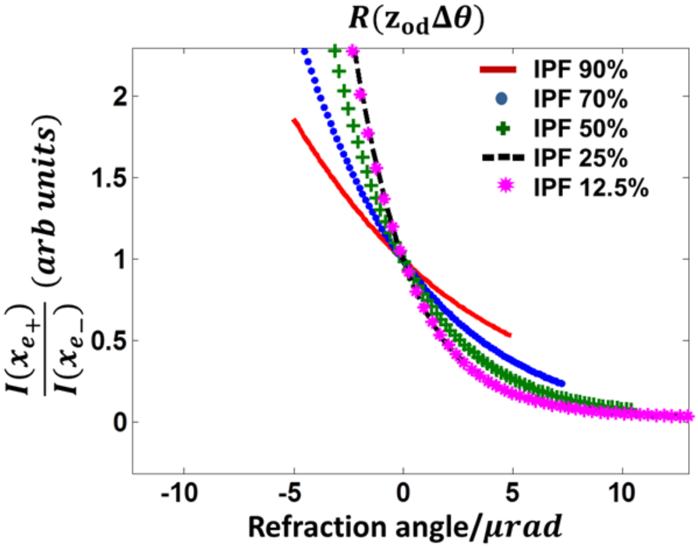

Figure 4-6 R-function curves obtained at various IPFs.

In the plot, the y-axis is the ratio of the mixed intensity images, acquired on opposite sides of the IC, while the corresponding refraction angle is reported on the x-axis. The R-function thus provides a more intuitive explanation of the increased contrast at smaller IPFs, since it is apparent that each R-curve possesses a different gradient. In particular, the gradient of the R-function at lower IPFs is steeper because they are normalised such that they all cross at the $x = 0\ \mu rad\ , y = 1$ point. This is actually a physical constraint since the refraction angle in the background region of an image must be 0, and therefore, any fluctuation in those regions can only be attributed to noise.

Moreover, the R-function also explains how phase wrapping can manifest in EI. If the refraction angle is so large that the beam falls on the other side of the IC, or goes onto the next period of the IC, then the signal cannot be recovered. This is especially true at the highest IPF (90%), where the detection of large refraction angles becomes more difficult. Due to the periodic nature of the IC, at IPFs approaching the IC turning points, large refraction angles can cause the R-function to become non-monotonic, meaning that its inversion is only valid within the confines of one period. This however can account for a relatively large range of refraction angles ($\sim 45\ \mu rad$ in this case). This is an interesting property, shared only by ABI, where a larger dynamic range is achieved without affecting the minimum resolvable angle.

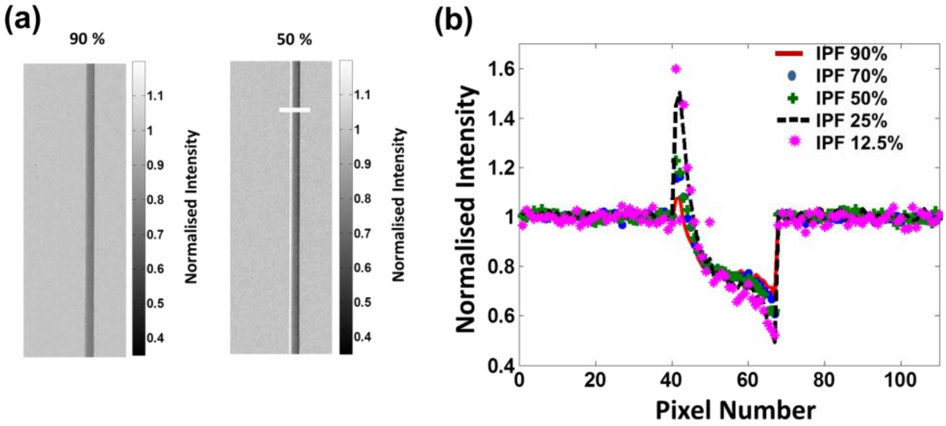

Figure 4-7 (a) Two example mixed intensity images of the sapphire wire acquired at different IPF values (90% and 50%). (b) The plotted profiles were extracted from the images obtained at all IPFs, from the same position along the wire as indicated by the line across the sapphire wire in the second image in (a).

The two mixed intensity images of the sapphire wire shown in Figure 4-7(a) were acquired at different IPF values (90% and 50%). In addition, profiles of the same wire, obtained at all IPFs, are compared against one another in Figure 4-7(b). These profiles have been extracted as indicated by the line visible across the wire in the second image of Figure 4-7(b). As expected, for both the profile and the image, a reduction in contrast is evident at higher IPFs. In fact, sapphire was selected for this comparison because it is a particularly challenging sample, which produces strong refraction and absorption signals, and therefore makes it easy to see this effect.

4.3.2 Constant Exposure Time

Phase retrieval was performed for each symmetric pair of images at a constant exposure time ($7\ s$), resulting in five phase retrieved images. First, the differential phase profile obtained at 50% IPF was compared against an analytically calculated profile obtained at the correct effective energy [Munro & Olivo 2013]. The result is shown in Figure 4.8.

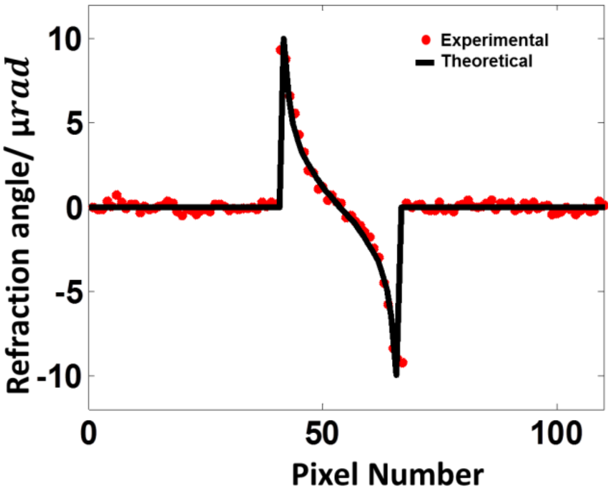

Figure 4-8 The experimentally retrieved differential phase contrast profile of sapphire at 50% IPF compared to the theoretical profile of the same object calculated at the effective energy for refraction, after considering the sample transmission.

Figure 4.8 shows a good match between the experimentally and analytically calculated profiles, which verifies the accuracy of the phase retrieval algorithm. The retrieved images of the sapphire wire obtained at all IPFs are shown in Figure 4.9. A qualitative comparison between the retrieved images in Figure 4.9 and the mixed intensity ones in Figure 4.7(a) makes it apparent that in the retrieved case, the strength of the retrieved refraction signal does not vary with IPF.

Another aspect which might be more difficult to appreciate from simple visual inspection of the images is that, since the images are retrieved and not “mixed”, the first and last images (acquired at 90% and 12.5% IPF, respectively) seem to be noisiest. This can be better appreciated from the profiles in Figure 4-10.

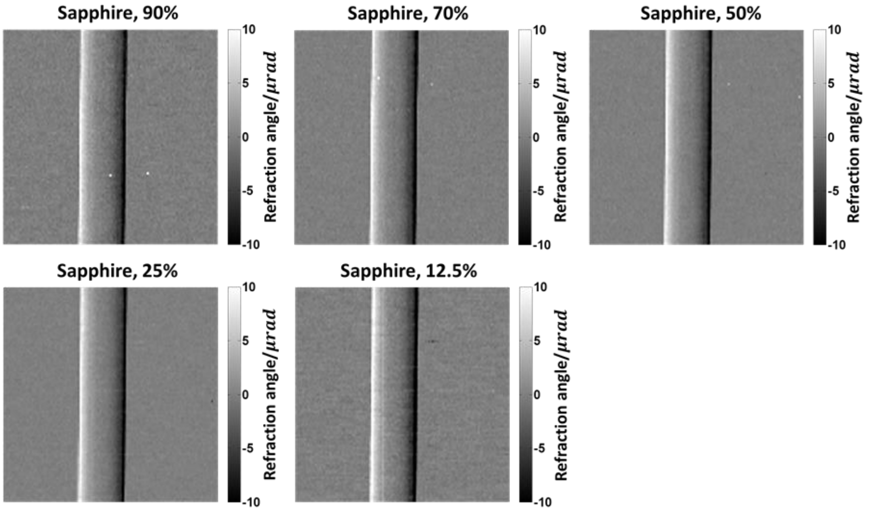
Sapphire, 90%

Sapphire, 70%

Sapphire, 50%

Sapphire, 25%

Sapphire, 12.5%

Figure 4-9 Differential phase contrast images of a sapphire wire at IPFs (90%, 70%, 50%, 25% and 12.5%).

Additionally, the fact the profiles in Figure 4-10, unlike those in Figure 4-7(b), are identical at all IPFs is further verification of the accuracy of the phase retrieval algorithms. It also means that the mixed intensity signal is correctly adjusted by including the shape of the IC slopes in the retrieval algorithm, i.e. by using the R-function.

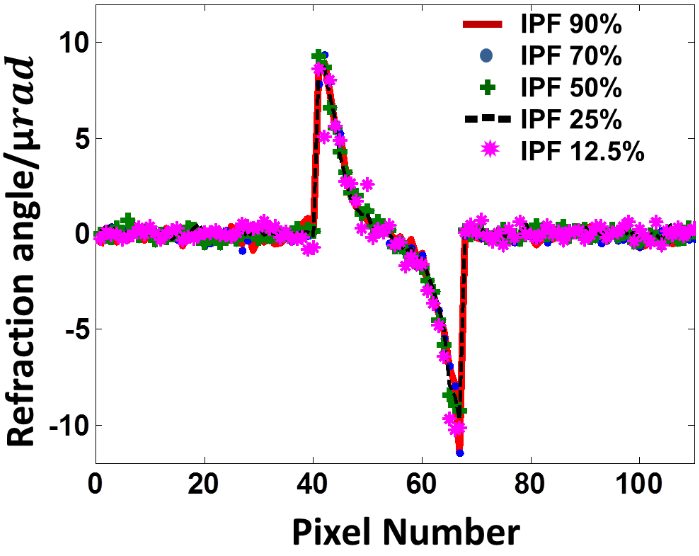

Figure 4-10 The retrieved profiles of the sapphire wire at all IPFs are compared against each other.

The sensitivity can now be extracted by measuring the standard deviation from a sufficiently large background region in the retrieved images. The sensitivity values measured at the various IPFs are reported in Table 4.1 and further verify that the images obtained at the largest and smallest IPFs are noisiest. In addition, the results obtained at 50% IPF can be compared against those extracted from a previous EI sensitivity study, in which the sensitivity was measured only at this IPF. In both cases, the same value for the refraction sensitivity was obtained. In principle, one could have expected a slight improvement in this case due to the use of a photon counting detector, but the similarity between the values is probably due mostly to the different pixel sizes used in the two studies.

Illuminated Pixel Fraction	$\sigma(\Delta\theta)\ /\ nrad$
90%	415 ± 10
70%	310 ± 5
50%	270 ± 10
25%	240 ± 3
12.5%	360 ± 10

Table 4.1 The error on the retrieved refraction angle $\sigma(\Delta\theta)$ at different IPFs for constant exposure time.

In particular, the Anrad detector, which was used in the previous study, has a pixel that is 1.4 times larger than that of Pixirad, leading to increased detected statistics per pixel of $(1.4)^2$ for the same exposure time. This means that normalising by the pixel size could lead to an improvement by a factor of 1.4, which would give a value of $\sigma(\Delta\theta) = 190\,nrad$. It should however be noted that additional factors might play a part in the comparison e.g. aperture sizes.

However, the most important aspect to observe in Table 4.1 is the trend of the sensitivity as a function of IPF. In this case, the absolute value of the sensitivity is not as important as the trend. The different values obtained at the various IPFs demonstrate that the quantity does indeed change as a function of IC position, as expected from Eqn. (4-6). In fact, the error on the retrieved refraction angle is minimal at 25% IPF and maximal at 90% IPF, which correspond to the positions of highest and lowest sensitivity, respectively. Furthermore, since sensitivity is a function of both the noise and IC slope (see Eqn. (4-6)), there is an optimal trade-off between detected photon flux and IPF value. The latter is ultimately driven by the precise shape of the IC and, in particular, by the gradients at various points of its shape.

In fact, the R-function curves in Figure 4.6 also provide a more general explanation for the trend shown in Table 4.1. For example, since the R-function curves at 12.5% and 25% overlap, it is reasonable to expect that their sensitivities would also match. However, the measurements in Table 4.1 demonstrate that the sensitivity at 12.5% IPF is significantly worse than the one at 25% IPF. This is due to the reduced photon flux, from which images acquired at lower IPFs would also suffer, compared to those acquired at the higher IPFs. This reduction would lead to more significant and increased noise fluctuations in the images acquired at lower IPFs. Ultimately, this would account for the subsequent reduction in sensitivity at 12.5% IPF.

4.3.3 Comparable statistics

For this part of the experiment, the mean background count in a single frame at 90% IPF was measured, and a number of frames were selected in order to approximately match this mean value at lower IPFs while using a discrete number of frames. However, due to the proximity of the first two points, at both 70% and 90% IPFs, only a single frame was used. Table 4.2 summarises the results obtained in the various conditions.

Illuminated Pixel Fraction	Number of frames	$\sigma(\Delta\theta)\ /\ nrad$
90%	1	550 ± 10
70%	1	420 ± 10
50%	2	270 ± 10
25%	3	200 ± 5
12.5%	7	235 ± 5

Table 4.2 The error on the retrieved refraction angle $\sigma(\Delta\theta)$ at different IPFs for images obtained with a different number of frames (but at approximately constant total number of counts).

Also in this case, the best sensitivity was achieved at 25% IPF; however, additional improvements were observed in Table 4.2 at 25% IPF and 12.5% IPF compared to the previous study. Indeed, in order to match the statistics to the one used at 90% IPF, greater numbers of frames were used at both 25% IPF and 12.5% IPF compared to the previous study. The increased number of frames compensates for the natural reduction in flux which would otherwise occur at lower IPFs. Hence, in Table 4.2, unlike Table 4.1, the sensitivity at 12.5% IPF is improved compared to those obtained at 50% and 70%, as well as when compared against the previous study.

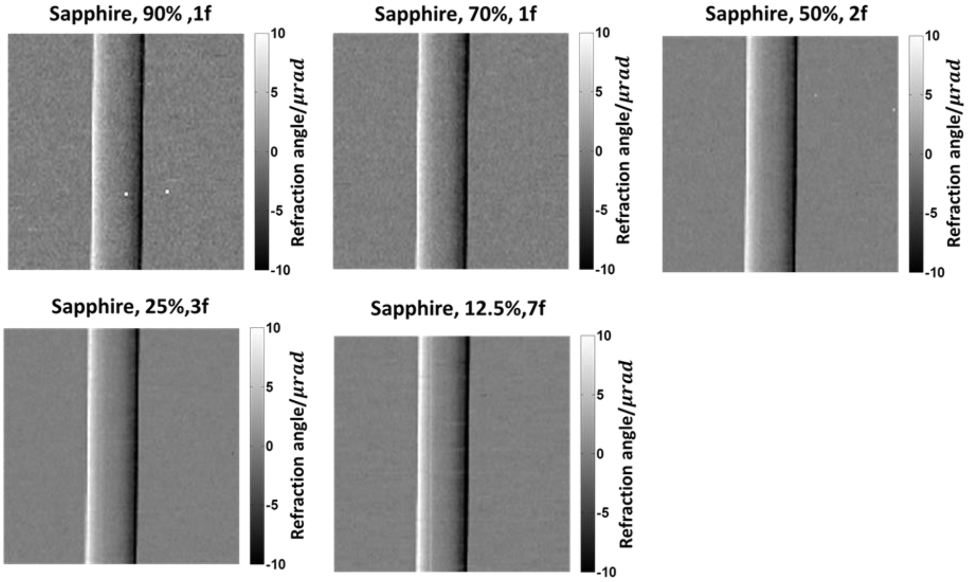
Sapphire, 90% ,1f

Sapphire, 70%, 1f

Sapphire, 50%, 2f

Sapphire, 25%,3f

Sapphire, 12.5%,7f

Figure 4-11 Differential phase contrast images at different IPFs retrieved with the number of frames required to approximately match the noise at 90 % IPF.

The images obtained at various IPFs are shown in Figure 4-11. The images have been reconstructed with varying number of frames. They show how the image quality varies as a function of the IC imaging positions. The images appear to become smoother as the IPF is decreased, with the background of the image acquired at 90% IPF appearing grainier than that of images acquired at lower IPFs.

Since the quantitative accuracy of the phase retrieval algorithm was validated in the previous part, the profiles of the wires will not be shown in this section.

4.3.4 Insect Leg

Biological samples present a more realistic challenge to XPCI systems, since they are characterised by unknown and complex geometries, as expected in a “real-world” setting. They can also contain small, weakly refracting features, invisible to conventional X-ray imaging set-ups, but detected by XPCI. Figure 4-12 shows images of an insect leg, which were acquired with 16 dithering steps at various IPFs. Seven frames were combined for each image in order to increase the overall image quality at all IPFs and to facilitate the discussion.

The images are displayed using the same window settings to ensure that the same $\Delta\theta$ corresponds to the same gray level. Furthermore, the images demonstrate how a loss in sensitivity can affect the visibility of some features present in a sample. For example, the hairs on the insect leg, which are practically pure phase objects, are clearly visible at 25% IPF and at 50% IPF (features 1 & 2 in Figure 4-12), but are only barely visible at 12.5% IPF and at 90% IPF.

Indeed, at the highest IPF, the decreased sensitivity leads to the weak signal from the hairs falling below the image noise. Moreover, the image acquired at 90% IPF suffers from additional artefacts, which manifest as horizontal lines (16 pixels in length) along the dithering direction (feature 3 in Figure 4-12). In fact, these artefacts are produced as a result of the dithering procedure, but can be seen much more clearly in this image due to reduced accuracy of the phase retrieval algorithm when performed with images acquired near the IC turning points.

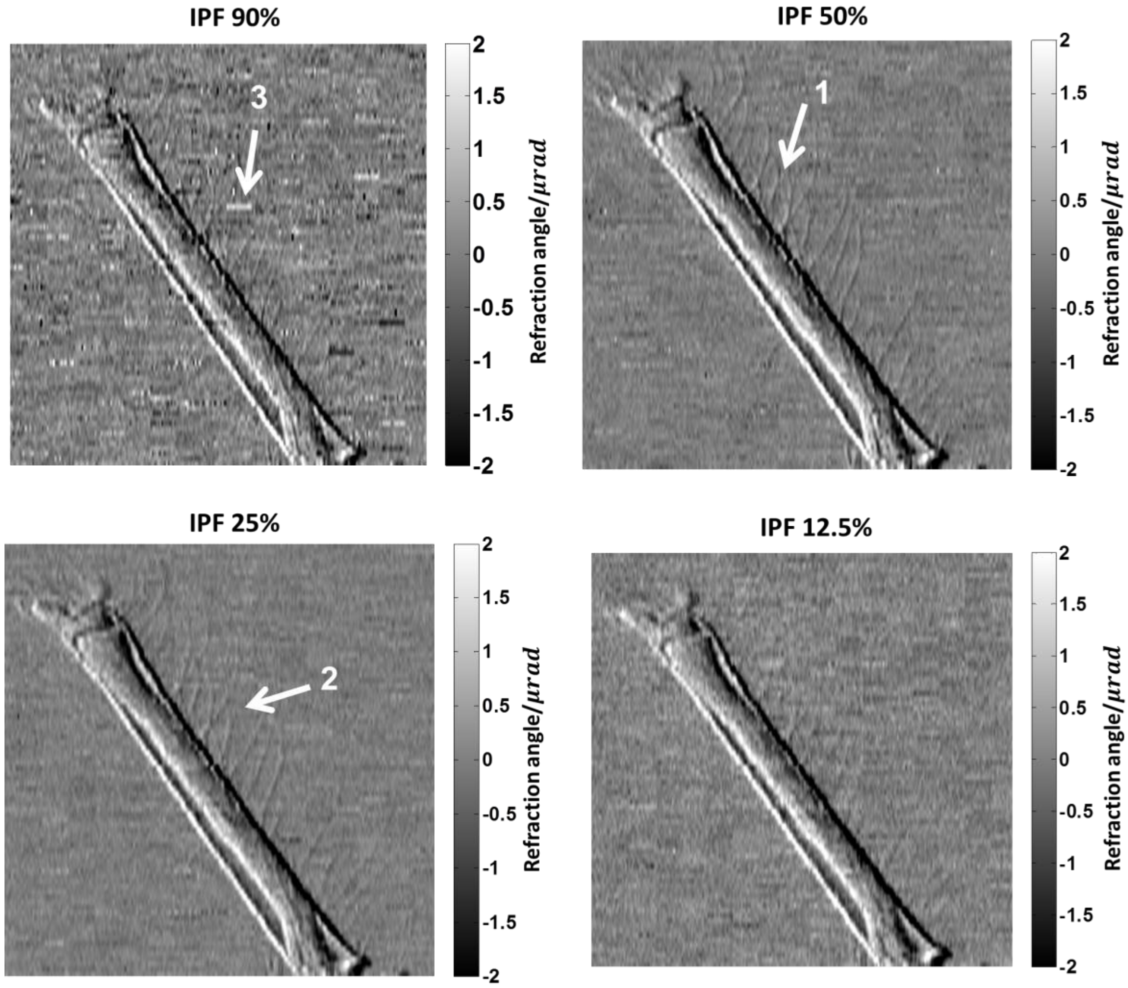

Figure 4-12 Differential phase images of an insect leg obtained at various IPFs. Insect hairs (features 1 & 2), which are visible at 50% and 25% IPF, cannot be visualised at 90% and 12.5%, due to the reduced refraction sensitivity at these IPFs. Also, the image at 90% IPF is noisy, and the dithering steps manifest as horizontal strips in the image (feature 3).

Finally, images of the same sample were combined also on the basis of the "comparable statistics" principle. In this case, since only seven frames were obtained at each IPF in total, the quality all the images shown in Figure 4-13 is either equal to or reduced compared to the images shown in Figure 4-12.

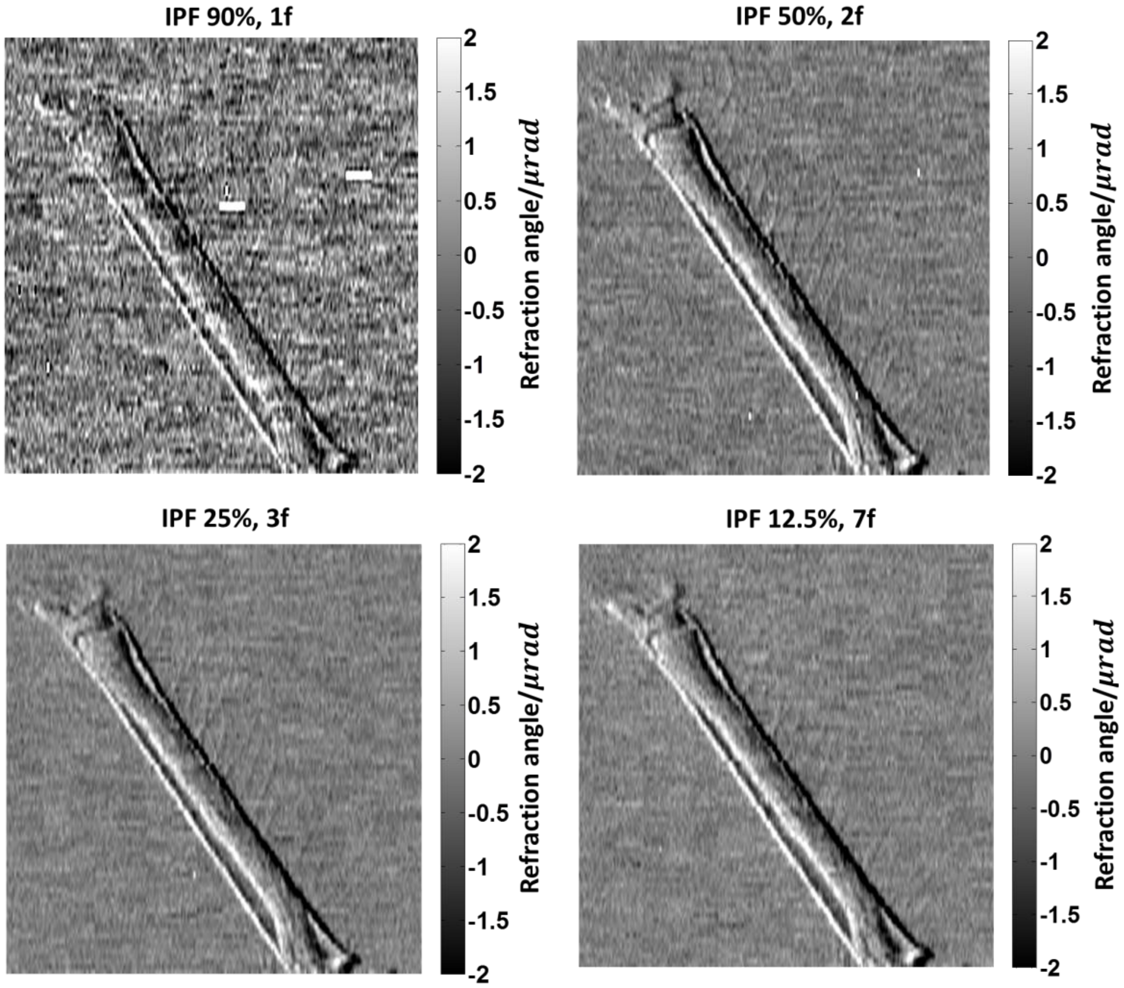

Figure 4-13 Differential phase images of an insect leg obtained at comparable statistics across all IPFs.

Here it is easier to see the disappearance of various details on the insect leg, especially its hairs, due to the increased noise. The images of the biological sample qualitatively agree with the trends measured in sections 4.3.2 and 4.3.3, i.e. in both modes, the best image quality is obtained at 25% IPF.

4.4 Summary

In this chapter, the experimental sensitivity of the standard (double mask) EI system was studied as a function of the position on the IC where the images are acquired. Five pairs of images were acquired across the span of the IC, and each symmetric pair was used to perform phase retrieval. First, a sapphire wire was used to verify the quantitative accuracy of the phase retrieval algorithm. Then, the standard deviation in the background of each differential phase image was measured in order to determine the minimum resolvable refraction angle.

Given the parameters of the current system, for the time limited case, where the exposure time was kept constant across the span of the IC, the sensitivity was found to be highest at 25% IPF, i.e. where the error on the measured refraction angle was lowest. Similarly, in the dose limited case, where the detected statistics are instead kept constant, the best sensitivity was also obtained at 25% IPF. The equivalence of these two results for the experimental conditions was not immediately obvious since no previous experimental studies of the EI sensitivity, as a function of IPF, had been undertaken.

However, the results from this study are aligned with those from previous ABI studies, which concluded that the refraction sensitivity would be highest at some position along the slopes of the RC [Rigon et al. 2007]. Indeed, the position of maximum sensitivity can change depending on several parameters, such as the mask apertures, inter-mask distances and source FWHM; ultimately, the sensitivity is a function of the IC gradient and the image noise. Hence, in future studies, an analytical model may be used to calculate the sensitivity for a variety of imaging parameters.

Chapter 5 Single-Mask Edge Illumination

5.1 Overview

Standard double mask EI possesses several advantages, e.g. achromaticity [Endrizzi et al. 2015a], relative insensitivity to misalignments [Millard et al. 2013; Endrizzi et al. 2015b], and an ability to work with fairly large, incoherent x-ray sources [Diemoz & Olivo 2014]. It has also been repeatedly demonstrated that EI is largely immune to the effects of vibrations on the order of a few microns: our current systems are located on the second floor of a densely populated building in the middle of a large city, and are therefore subject to vibrations of this magnitude without much detriment to the data collected. However, the need to acquire two images for separate differential phase and absorption retrieval can increase the likelihood of errors occurring while positioning the sample or the masks in between the two acquisitions. This could have an adverse effect on the quality of the retrieved images. While these additional sources of error can be mitigated by careful data collection and analysis procedures, the ability to perform phase and absorption retrieval on images acquired in a single shot would simplify and speed up the acquisition procedure. This can also lead to a more dose efficient acquisition method.

For this reason, numerous adaptations have recently been made to the EI system which better exploit its advantages [Endrizzi et al. 2015; Basta et al. 2015; Vittoria et al. 2015a]. Thus far, two such developments have explored the possibility of acquiring sufficient phase-based information with a single exposure. The first approach allows for the retrieval of the electron density or thickness of a sample from a single mixed intensity projection [Diemoz et al. 2015]. This single image phase retrieval method uses the free-space propagation and transmission signals in the direction orthogonal to EI sensitivity to enforce consistency between the image columns, thereby eliminating some common artefacts in 1D phase integration. However, for inhomogeneous materials, where the ratio between δ and β is not constant, the approximation breaks down or requires ad-hoc tuning of δ / β to achieve the best image quality for selected features only.

Another approach, termed “beam-tracking" [Vittoria et al. 2015a; Vittoria et al. 2015b], employs a pixel that is sufficiently small to resolve the individual beamlets, such that the changes to each beamlet caused by the sample's attenuation, refraction and scattering can be retrieved by comparing it to the reference case i.e. without the sample. To be effective, this method requires a high resolution detector or a high magnification set-up: conditions which may not always be practical or even achievable.

In this chapter, a simpler approach to single shot EI XPCI is described, which removes some of the limitations of the methods mentioned above, i.e. it does not require any assumption on δ/β, or a high resolution detector. The simultaneous acquisition of two images is achieved by using a single-mask approach, and eliminating the detector mask. In this approach, odd and even columns are used to create two separate images (with half the resolution) that are then used as input for the retrieval procedure.

This experiment aims to investigate the advantages and disadvantages of the single-mask set-up compared to the standard EI set-up. In the first part of this chapter, a laboratory implementation of a single-mask EI system is compared against the standard EI set-up. Both set-ups are used to acquire images of a wire sample for which contrast, SNR and refraction sensitivities of both systems are evaluated.

The experimental set-ups are then modelled via the wave optics simulation package described in chapter 3. The simulation has been modified to incorporate the polychromatic spectrum of the Rigaku source at 35 kVp and the Anrad detector, which were both used in the experiment. Following benchmarking of the simulation against experimental results, simulated images are used to study and compare the signal and refraction sensitivities of the two EI set-ups.

5.2 Laboratory single-mask and standard EI set-ups

The single-mask EI system consists of only a pre-sample mask, which defines a set of beamlets that are incident on the detector (Figure 5-1(a)). The beamlets are aligned so that they hit the boundary between two pixels, and the edges of the detector pixel are used as the “sensors” to track refraction-induced beam displacements.

Figure 5-1(b) shows that refraction to the left-hand side redirects the beam onto pixel 1, thus increasing its counts while simultaneously reducing the beam intensity incident on pixel 2. The opposite would obviously occur for refraction to pushing the beam to the right-hand side. The opposite effect that refraction has on the two pixels allows the acquisition of two “reversed” refraction images in a single exposure (Figure 5-1(c)), which, as we have seen in previous chapters, can be used to perform phase and absorption separation. Figure 5-1(a) also shows that the SM-EI set-up requires the use of line-skipped masks in order to create its alternating illumination condition in odd and even pixel columns. It is important to note that line-skipped masks are not required for the standard EI set-up, but they were used here for the sake of comparing the two set-ups under equivalent conditions.

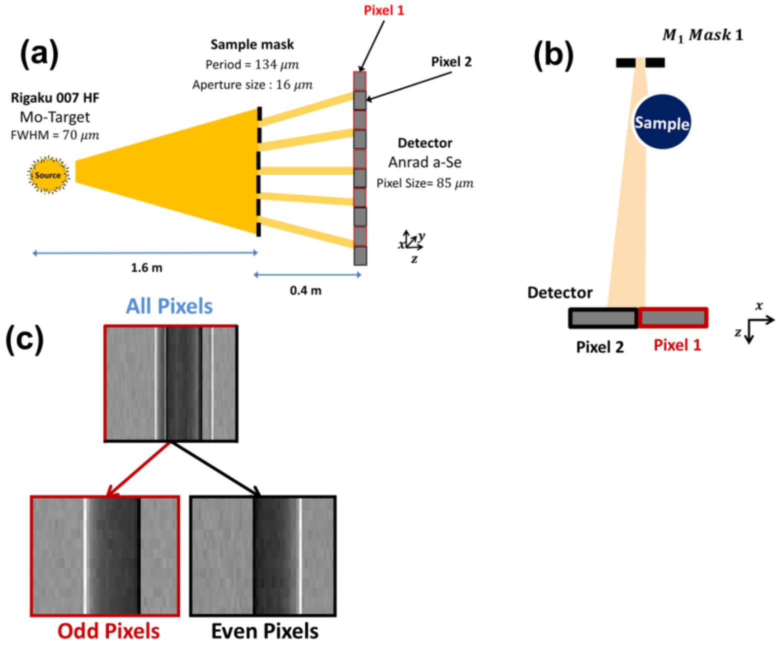

Figure 5-1 (a) is a schematic of the single-mask EI set-up; the mask apertures define beamlets which are aligned with the edge between two pixels. (b) shows a section of the set-up in (a); however, the addition of a refracting sample causes a displacement of the beamlet. Ultimately, this demonstrates how inverted refraction signals can be simultaneously acquired by separately considering odd and even pixels (i.e. pixels 1 and 2 respectively). (c) shows the mixed intensity image obtained when combining every pixel, as well as the images obtained by separating the odd and even pixels, respectively.

In the experiment, the pre-sample and detector masks had periods of $p_1 = 134\ \mu m$ and $p_2 = 167\ \mu m$, and aperture sizes of $a_1 = 16\ \mu m$ and $a_2 = 20\ \mu m$, respectively. The pre-sample mask was placed at a distance of $1.6\ m$ from the source, and aligned with the detector pixels columns. In the comparison below, the same pre-sample mask was used also in the standard (double mask) EI set-up, and the detector mask was added, to switch from the SM-EI to standard EI set-up. Masks had nominal septa thickness of $\sim 30\ \mu m$ of gold electroplated on $500\ \mu m$ of graphite. However, it has been shown that the septa thickness can be less than the nominal value if difficulties are encountered during the electroplating process. This can lead to increased unwanted transmission through the mask, reducing the sensitivity of the system by introducing a higher offset in the ICs. The SM-EI set-up is particularly sensitive to this effect, since only one mask is used and therefore, X-rays traverse only one gold layer.

In both the single and double mask cases, 32 dithering steps were used to increase the spatial resolution of the images, with an exposure time of 30s per step. In applications where resolution is important, the single-mask set-up would require twice as many dithering steps as a standard non-skipped EI system in order to match its resolution. Hence, to ensure an equivalent initial spatial resolution, we used a skipped mask for the standard EI set-up in our comparison. It is also important to understand that dithering only improves the spatial resolution of an image, but not the statistics in each pixel, and may not be required in some biomedical applications [Olivo et al. 2013].

5.3 Modelling EI and SM-EI signal

The experimental set-ups described in the previous section were also modelled with the wave optics simulation package. The primary goal was to model the mixed intensity profiles produced by both set-ups and compare them against the experimental data. This required adding several components and features to the wave optics simulation. These modifications are schematised in Figure 5-2; they include the absorption from the graphite substrates in the masks, the carbon fibre cover of the detector and its energy response, which to first approximation is assumed to be linear.

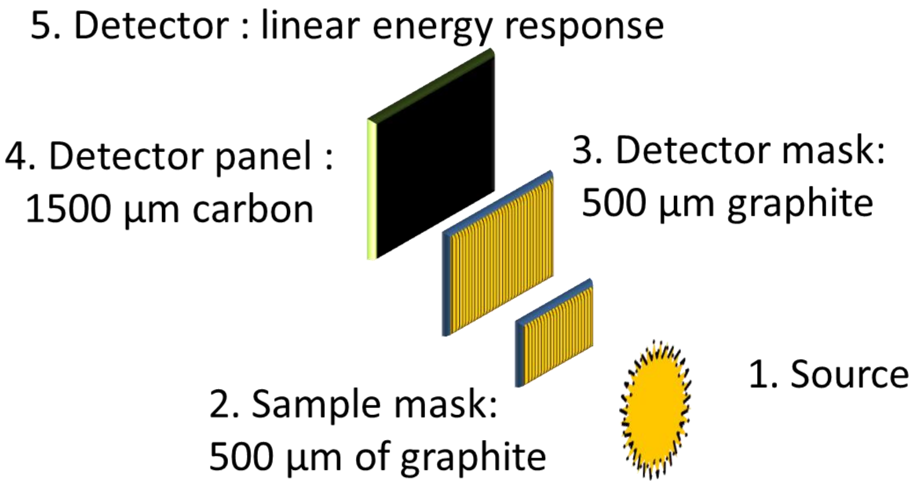

Figure 5-2 A schematic list of the components which were incorporated into the wave optics simulation in order to model both EI and SM-EI set-ups.

5.3.1 Validating the model

Experimentally acquired measurements of the spectrum, sampled in 0.5 keV steps, were provided by the manufacturers (Rigaku), and for the sake of simplicity the detector was assumed to have a linear energy response. Both assumptions are consistent with those used in previous works [Millard et al. 2014]. Polychromatic images were thus obtained by performing monochromatic simulation at given energy steps over the desired range of energies, and taking the weighted average over the spectrum [Olivo & Speller 2006].

The IC is a key parameter in the characterisation of EI set-ups, and can thus be used to assess the accuracy of simulations by comparing simulated ICs against experimentally obtained ones. Therefore, the model was initially benchmarked against a previous experimental measurement of the IC acquired at 40 kVp with a standard EI set-up, which employed an older and well-characterised set of masks. The septa thickness of the masks used in this measurement are known ($\sim 28\ \mu m$) [Millard et al. 2014]; however, they were also independently determined here by matching the offset in the experimental and simulated IC curves. The result is displayed in Figure 5-3 and shows a good agreement between the simulation and experimental data.

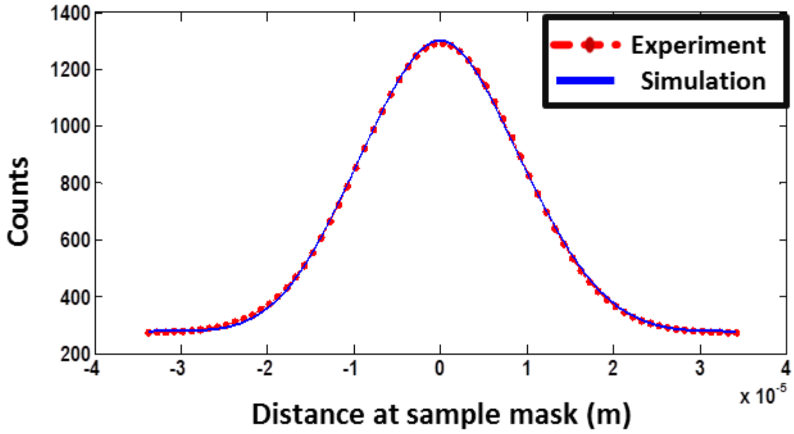

Figure 5-3 Benchmarking of the wave optics simulation by comparison with an experimental IC acquired with a well-known set of masks at $40\ kVp$.

The next step involved modelling the SM-EI set-up at 35 kVp using the new mask. Validation of the model was also obtained through benchmarking the simulated IC against the experimental data. Due to the absence of the detector mask, the IC was modelled by introducing the detector PSF into the simulation. Analytically, the SM-EI IC, L_{SM}, can be expressed in the following way:

$$L_{SM}(x) = Src\left(\frac{z_{od}x}{z_{so}}\right) * M_1(x) * PSF(x), \qquad \textbf{(5-1)}$$

with:

$$\mathrm{PSF(x)} = rect\left(x - \frac{w}{2}\right) * \exp\left(-\frac{x^2}{2\sigma_{PSF}^2}\right), \tag{5-2}$$

where $Src\left(\frac{z_{od}}{z_{so}}x\right)$ represents the rescaled source size, $M_1(x)$ represents the first mask and $PSF(x)$ is the point spread function of the detector, modelled as a convolution between an ideal pixel (top-hat function) of size w, and a Gaussian parameterised by σ_{PSF}, its standard deviation. It is worth noting that in chapter 4 the PSF does not appear in the expression for the standard EI IC in Eqn. (4-1) because the presence of the detector mask apertures redefines the pixel response by introducing a sharp cut-off before the physical edge of the detector. On the contrary, for SM-EI, the sensitivity with which the transition of the beam can be detected, as it shifts between two pixels, depends on the slope of the detector PSF, and therefore on pixel cross-talk. Generally, one side of the PSF can be considered as a smoothed edge, which leads to a broader IC for SM-EI compared to the standard EI case, where the pixel response redefined by the detector mask can be considered to be ideal.

In chapter 4 it was shown that the refraction sensitivity for standard EI can be calculated directly from the IC. This is equally true for SM-EI; however, since the IC is a convolution between beam, the sample mask and the detector PSF (Eqn.(5-1)), the sensitivity of the set-up is directly influenced by the detector PSF. In fact, as pixel cross-talk increases, the Gaussian with which the pixel is convolved becomes larger, which leads to a smoother PSF function, a decreased slope of the IC and ultimately a less sensitive SM-EI set-up.

5.3.2 Modelling the experimental set-ups

To reduce the oscillations in the experimentally measured PSF, this was fitted with the analytic expression shown in Eqn. (5-2), which resulted in the extraction of $\sigma_{PSF} = 10\ \mu m$. Note that, as is made clear by Eqn. (5-2), σ_{PSF} does not refer to the width of the PSF but only to the Gaussian curve used to smooth its first order "ideal" approximation, i.e. a box function. The fitting is shown in Figure 5-4 and, as can be seen, provides a satisfactory representation of the data. The PSF and linear energy response of the detector could then be included in the simulation, leaving the thickness of the mask septa as the only parameters to be determined.

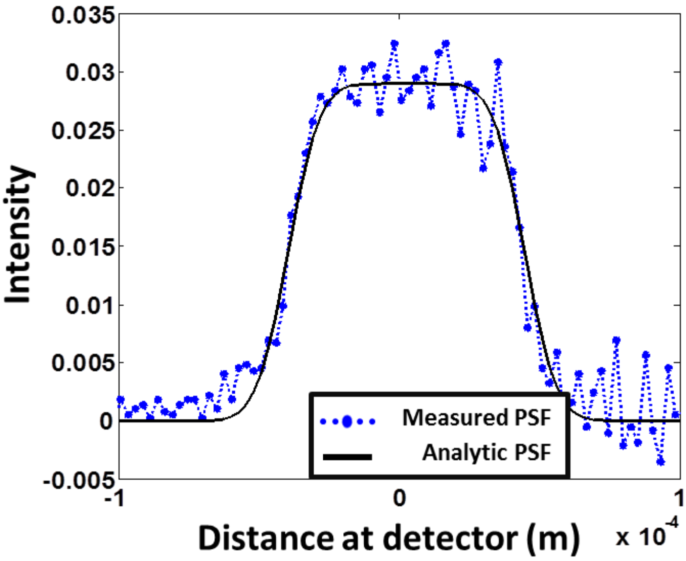

Figure 5-4 The experimentally measured PSF of the Anrad detector and the analytically fitted function.

Next, the septa of two different masks had to be determined (the sample mask used in both set-ups and the detector mask used for the standard EI set-up), which was done in two steps. First, the thickness of the septa in the sample mask was determined by matching the single mask IC offset (Figure 5-5(b)). Once this was known, it was used in a second step, where the thickness of the detector mask septa was determined by matching the offset of the simulation to that of the standard EI IC (Figure 5-5(a)). As previously stated, the thicknesses of the mask septa are often found to be lower than their nominal values. In this case, a match with the single mask IC offset was obtained with a simulated sample mask septa thickness of $17\mu m$. Figure 5-5(b) shows a comparison between the experimental and simulated single mask ICs. Each “arm" of the SM-EI IC corresponds to one set of skipped pixels (e.g. odd pixels, like pixel 1 in Figure 5-1(b)), while the other corresponds to the adjacent ones (e.g. even pixels, like pixel 2 in Figure 5-1(b)).

The sample mask position at which the two images needed for the phase retrieval are simultaneously acquired corresponds to the point at which both sets of pixels share an equal amount of the incident beam, i.e. the sample mask position where the two “arms” of the single mask IC intersect in Figure 5-5(b). At this position, the two sets of pixels, corresponding to “odd" and “even" columns, are subjected to an “inverted illumination condition”, i.e. any photons gained by pixel 1 due to refraction are simultaneously lost by pixel 2. This corresponds to the detection of simultaneous positive/negative refraction signals in neighbouring pixels, producing the two images with inverted refraction-induced contrasts, which are needed for the phase retrieval. Conversely, for the standard EI set-up, two images were obtained at the 60 % illumination level on both sides of the IC with two separate exposures.

Figure 5-5(a) shows a comparison between the experimental and simulated standard ICs, for a detector mask septa thickness of $28\,\mu m$, which is very close to the nominal value of $30\,\mu m$. Figure 5-5(b) shows the same thing for SM-EI. The good agreement shown in Figure 5-5(a) and (b) demonstrates that the characteristics of the source, sample mask, detector mask and the detector have been modelled satisfactorily. This also means that the model can be used to predict the signal generated by each system for a given sample.

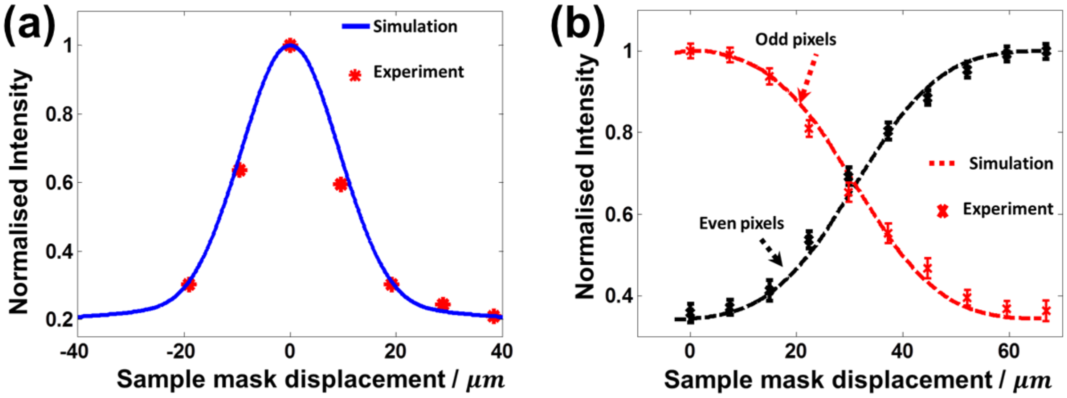

Figure 5-5 (a) The simulated and experimental standard EI illumination curves. The SM-EI ICs from simulation and experiment are shown in (b); the curve is obtained by combining all the "odd" and "even" pixels, respectively.

To further demonstrate the principle according to which the shape of the PSF significantly affects SM-EI but has no effect on standard EI, the ICs of both set-ups were simulated using two different PSFs. The first was the experimentally measured one for the Anrad detector, with $\sigma_{PSF} = 10\ \mu m$, and the second was an ideal pixel response, i.e. with $\sigma_{PSF} = 0$. It is apparent from Figure 5-6(a) that the IC of the standard system remains unchanged, while the SM-EI set-up in Figure 5-6(b) has a steeper IC for an ideal pixel response compared to the real Anrad case. This highlights one advantage of using the detector mask in standard EI: it mitigates possible negative effects of non-ideal detectors, which allows greater flexibility in realising the set-up.

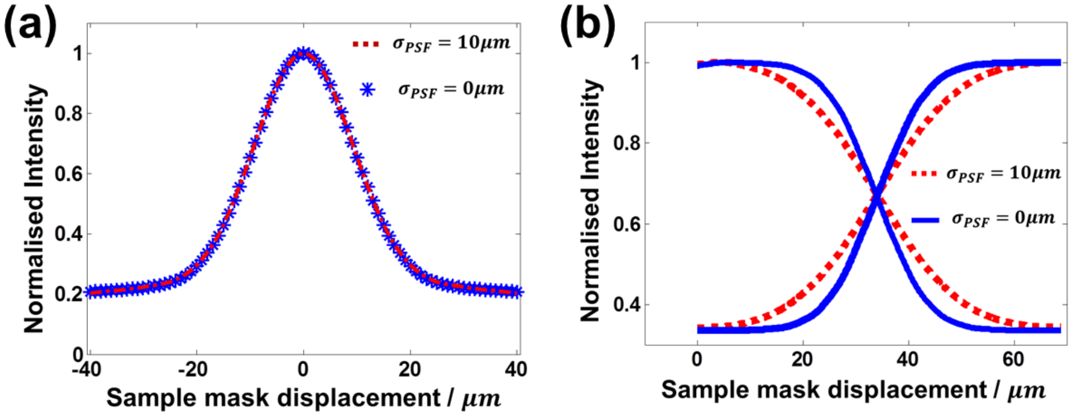

Figure 5-6 The simulated IC for (a) the standard EI set-up and (b) the SM-EI set-up using two different PSFs.

This also means that, for standard EI, the mixed-intensity signal is independent of the detector PSF, while it changes, depending on the detector, for the SM-EI set-up. In order to verify this, the profiles of the sapphire wire were simulated and compared against each other for the two set-ups using both the ideal and experimentally measured detector PSF. The profile acquired using the standard EI set-up was used as a reference signal since it does not change when different PSFs are used.

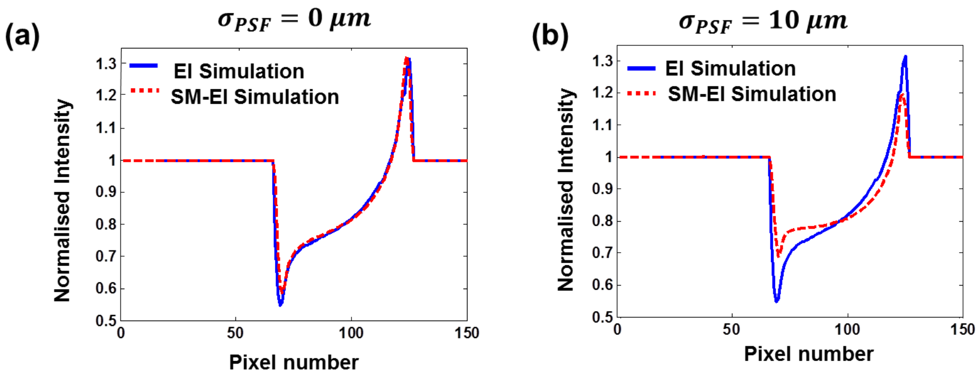

Figure 5-7 Simulation of a sapphire wire profile obtained with (a) an ideal detector and (b) a detector with $\sigma_{PSF} = 10\ \mu m$ for both set-ups.

As expected, Figure 5-7(b) shows a reduction in the contrast of the wire for the SM-EI set-up as σ_{PSF} increases, which is consistent with the reduced slope steepness of its IC visible in Figure 5-6(b). Figure 5-7(a) shows that the use of a detector mask is equivalent to using a detector with an ideal pixel response, since the profiles obtained with the two set-ups are indistinguishable.

Two main ways have been identified to compare the performance of the SM-EI set-up to that of its standard counterpart. In the first one, referred to as SM_1, the total acquisition time for acquiring the two images with the standard set-up, t_{EI}, is halved when the SM-EI set-up is used, $(\text{i.e. } t_{SM_1} = \frac{1}{2} t_{EI})$, thereby halving the dose delivered to the sample. In the second approach, referred to as, SM_2, the total acquisition time was the same in the two cases, $(t_{SM_2} = t_{EI})$. In this case, the dose received by the sample is the same, but higher (double) statistics are collected in SM-EI. The latter approach was selected for comparison in order to determine whether the increased statistics was sufficient to compensate for the reduction in sensitivity caused by the broadening of the IC, which is predicted by Eqn. (5-1) for non-ideal detectors.

5.3.3 Comparison against experimental data

All experimental images were first normalised by the flat field (an image without the sample) in order to eliminate mask defects and non-uniformities in the detector response/radiation field in the sample image. Contrast and SNR were evaluated for each wire in one mixed intensity projection for the standard and SM-EI systems according to Eqn. (1-11) and the definition of SNR used in Diemoz et al, which is shown in Eqn. (5-3) [Diemoz et al. 2012]:

$$\mathrm{SNR} = \frac{I_{max} - I_{min}}{\sqrt{2\sigma\left(I_{background}\right)^2}}\ , \tag{5-3}$$

where I_{max} and I_{min} are the maximum and minimum signals, respectively and $\sigma(I_{background})$ is the standard deviation of the image in a background region adjacent to the wires. The mixed intensity images are displayed in Figure 5-8 and were acquired using the second approach (SM_2).

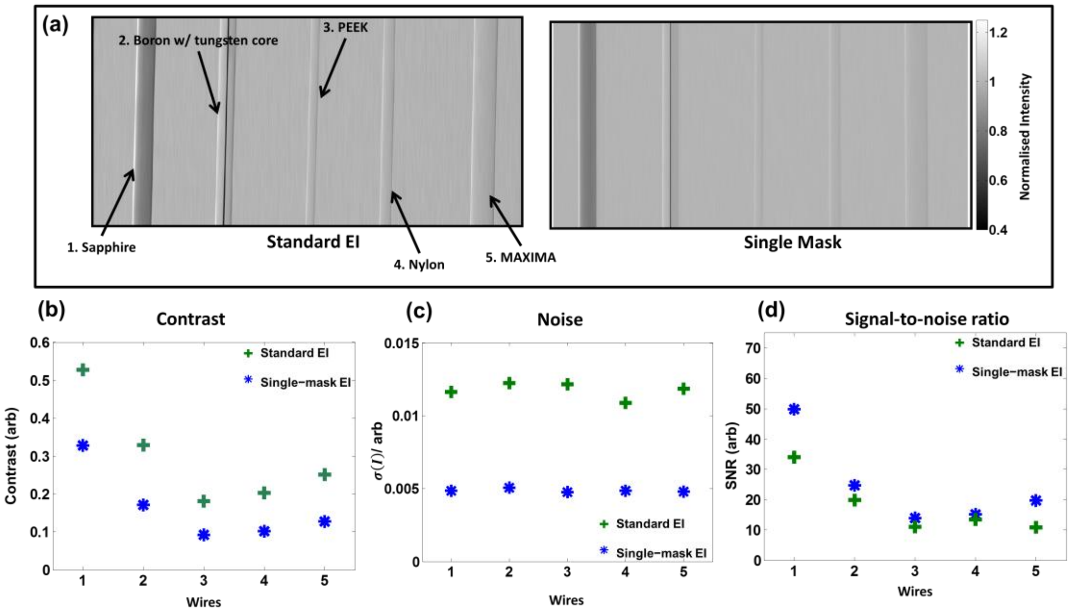

Figure 5-8 (a) Standard and SM-EI experimental mixed intensity projections of a sample consisting of five wires: 1) Sapphire ($radius\ =\ 120\ \mu m$), 2) Boron w/ tungsten core ($Boron\, radius\ =\ 100\ \mu m, Tungsten\, radius\ =\ 7\ \mu m$), 3) PEEK ($radius\ =\ 60\ \mu m$), 4) Nylon ($radius\ =\ 70\ \mu m$) and 5) MAXIMA ($radius\ =\ 150\ \mu m$); (b) shows the contrast for each wire in both set ups, (c) shows the noise in the background regions and (d) shows the signal-to-noise ratio.

Figure 5-8(a) shows images of the wire samples acquired with the standard (left) and SM-EI (right) set-ups. These wires were selected because they represent a range of geometries, as well as refraction and absorption properties. Figure 5-8(b) shows the contrast from the five wires, Figure 5-8(c) shows the average noise in the background regions, and Figure 5-8(d) is the SNR calculated using the values from the previous two figures. In the standard EI set-up, each wire possesses a higher contrast than when acquired with the SM-EI set-up. On the other hand, the SNR appears to be higher for the SM-EI set-up, thanks to the aforementioned increase in photon statistics, resulting from the use of the SM_2 approach. In other words, the reduction in noise observed in the single-mask case when the same exposure time is used overcompensates for the loss of phase sensitivity, which is made evident by the contrast reduction in the SM-EI case.

From among the samples used, the PEEK and sapphire wires were selected for the purposes of comparing simulation and experimental data. These wires were selected as they represent extreme examples of weakly/strongly absorbing/refracting objects.

Figure 5-9(a) and (b) show the experimental mixed intensity images of the PEEK wire for the standard EI and SM-EI cases, respectively. Figure 5-9(c) and (d) show a comparison between the simulated profiles and the experimental ones of the PEEK wire, which are extracted from the red lines shown in the images in Figure 5-9(a) and (b). Similarly, Figure 5-9(e)-(h) show the same data for the sapphire wire. There is generally a good agreement between the experimental and simulated profiles. However, for both set-ups, the simulation slightly overestimates the absorption of the sapphire wire through its thickest part. This slight discrepancy can be attributed to imperfect knowledge of the source spectrum and detector energy response function. Furthermore, it is consistent with previous results which were obtained using a Monte Carlo model of the system using the same material data, spectrum, and a linear detector energy response as inputs. Despite this, it is worth noting that the general shape of the profiles and the reduction in contrast suffered by the wires for the SM-EI set-up is well modelled by the simulation.

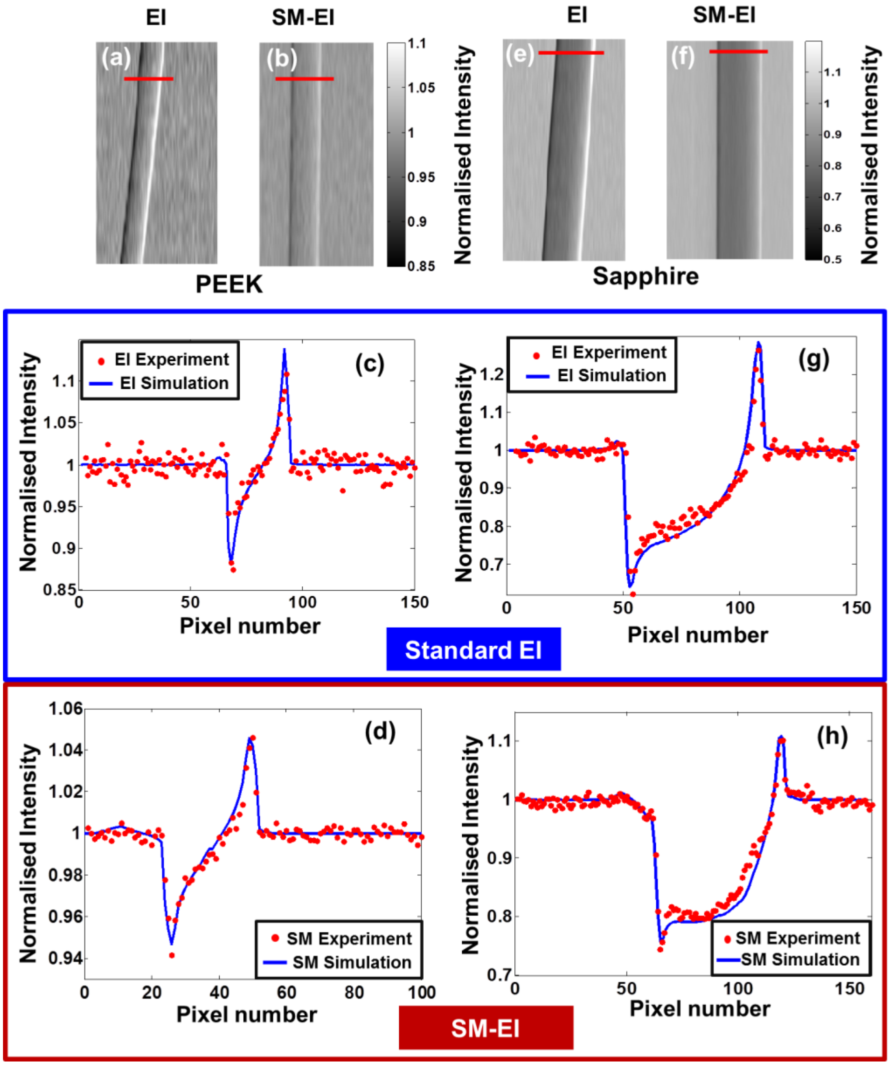

Figure 5-9 (a) and (b) are mixed intensity images of the PEEK wires acquired with the standard and SM-EI set-ups, and (c) and (d) are their simulated profiles compared against the experimental ones. (e) and (f) show mixed intensity images of the sapphire wire and (g) and (h) show their simulated profiles compared against the experimental ones. All experimental profiles were extracted along the red lines indicated in the images of panels (a), (b), (e) and (f).

It should be noted that, as well as reduced steepness of the IC in the SM-EI case, the reduction in the total mask septa thickness also contributes to the sensitivity reduction. Since unwanted transmission through the mask increases, it leads to a higher IC offset, which further underlines the importance of the detector mask in generating increased contrast in standard EI set-ups, as previously stated.

Finally, differential phase retrieval was performed on the two sets of images, using the method developed by Diemoz et al, which was described in chapter 4. To test the reliability of the two approaches, the experimentally retrieved differential phase profiles were compared against their theoretical counterparts, $\tilde{r}$. The latter have been calculated numerically at each energy bin, then weighted by taking into account the approximate X-ray spectrum and detector linear energy response, $spec(E)$, and the transmission through the wire and other optical elements in the set-up $t(E)$ as follows:

$$\tilde{r} = \frac{\sum r(E) \times spec(E) \times t(E)}{\sum spec(E) \times t(E)} . \tag{5-4}$$

The differential phase images obtained from experimental data collected with the two set-ups are displayed in Figure 5-10(a) and (b) for PEEK, and Figure 5-10(e) and (f) for sapphire, while their profiles are displayed in Figure 5-10 (c) and (d) (PEEK) and Figure 5-10(g) and (h) (Sapphire).

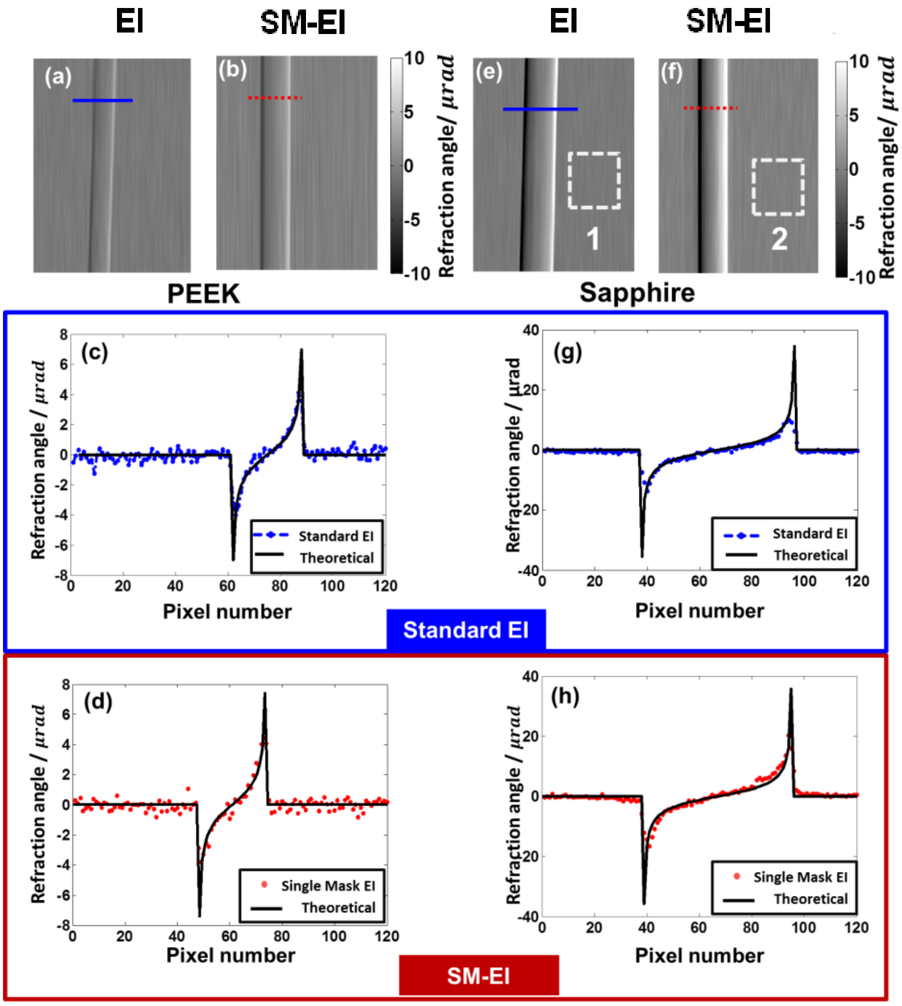

Figure 5-10 (a) and (b) are differential phase retrieved images of the PEEK wires with standard and SM-EI set-ups and (c) and (d) are the corresponding experimental profiles compared against the theoretical ones. (e) and (f) show differential phase retrieved images of the sapphire wire and (g) and (h) show their experimental profiles compared against the theoretical ones. All experimental profiles were extracted along the blue/red lines indicated in the images of panels (a), (b), (e) and (f); values for the sensitivity for the standard and SM-EI set-ups were measured in background regions 1 & 2 shown in (e) and (f), respectively.

There is a generally good agreement between experimentally measured profiles and their respective theoretical counterparts; however, the profiles acquired with the two set-ups are slightly different from one another. The main reason for this is that the theoretical profiles were calculated by taking into account the resultant spectrum for each set-up. These are different, since for SM-EI the beam only passes through a total of $2\ mm$ of carbon, while there is an added $0.5\ mm$ thick layer in the standard EI set-up due to the substrate of the additional mask. The most likely discrepancy on the retrieved profiles relates to the increase in the unwanted transmission through the septa encountered when a thinner mask is used. This means that the sample is simultaneously irradiated by two spectra, one hardened and one not, passing through the mask septa and through the apertures (Figure 5-11(a)). This has a negative effect on the refraction signal at the edges of a highly absorbing wire. For this reason, as can be seen in Figure 5-11(b) for SM-EI, slight discrepancies can be observed at the edges of the sapphire wire, which are not present for PEEK. This is because sapphire, being more absorbing, introduces different degrees of additional hardening to parts of the beam going through the septa and those going through the apertures; this is not observed for PEEK since its absorption is negligible compared to sapphire. As well as being visible when the experimental profiles are compared directly (Figure 5-11(b)), this becomes even more obvious by comparing their simulated profiles (Figure 5-11(c)).

However, these effects can be eliminated through the use of thicker masks; in which case, the profiles of the sapphire wire, obtained with both standard and SM-EI, become identical (Figure 5-11(d)). Additionally, the thinner masks cause a high offset for the SM-EI IC, which negatively affects the phase retrieval algorithm.

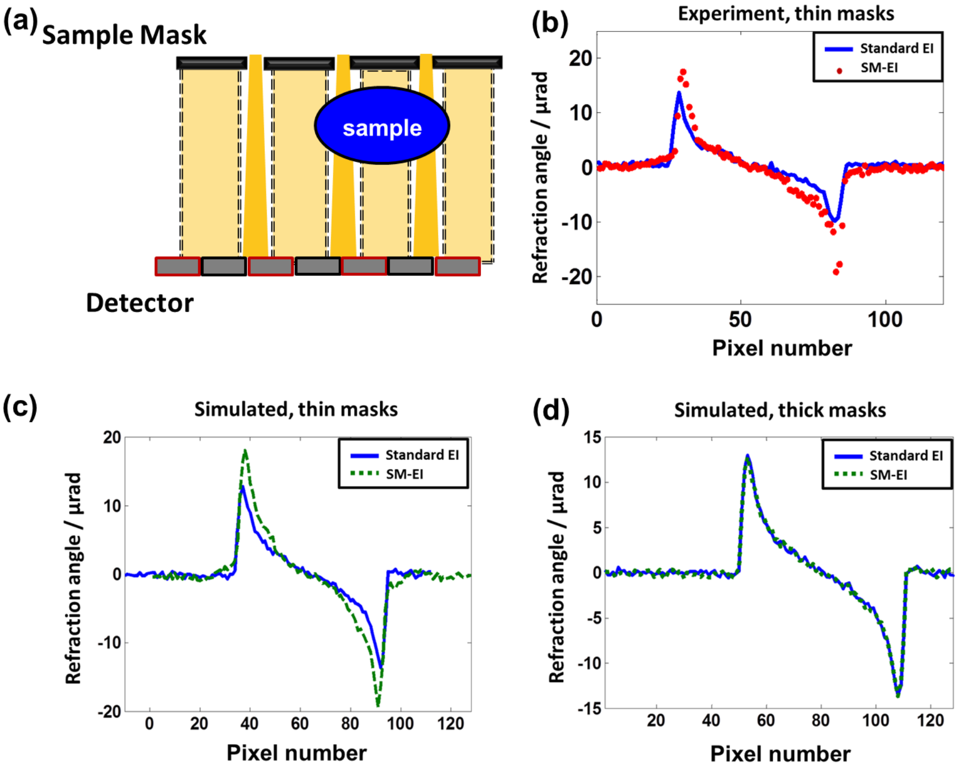

Figure 5-11 (a) is a schematic depiction of transmission through the mask for SM-EI, (b) shows the phase retrieved profiles of the sapphire wire obtained with standard and SM-EI set-ups compared against each other. In (c) the simulated profiles are compared for the same $17\ \mu m$ thick mask septa as used in the experiment, while in (d) much thicker mask septa were simulated, equivalent to the standard EI case ($44\ \mu m$).

It is important to note that the standard EI system does not suffer from such effects probably because the combined thickness of the mask septa is sufficient to make beam hardening effects negligible. This is somewhat supported by its IC in Figure 5-5(a), which has a lower offset (~20%) than the SM-EI IC (~35%).

The experimental sensitivity of the two set-ups was then measured by calculating the standard deviation within the ROIs in the respective phase retrieved images. For the standard EI set-up, the sensitivity was $280 \pm 10\, nrad$, while for SM-EI it was $350 \pm 10\, nrad$. The decreased sensitivity for the standard EI set-up compared to the values obtained in chapter 4 can be attributed to several factors, which include a larger aperture size in the sample mask, thinner mask septa and the use of a non-photon-counting detector.

In order to obtain an equivalent measurement from the simulated data, a comparable level of noise to that of the experimental images was added to the simulated profiles, and the sensitivity was extracted from them following the same procedures outlined above. However, noise was added to the simulated images after the PSF blurring was applied to the image. This means that noise for adjacent detector pixels is completely uncorrelated, which is not necessarily true in the experimental case. Indeed, in the latter case, as σ_{PSF} becomes larger, the noise correlation between adjacent pixels is expected to increase, leading to an apparent increase in sensitivity. However, in this case, the uncorrelated noise is assumed to be a good approximation since σ_{PSF} is small compared to the overall pixel size. The validity of this assumption is further underlined by the good agreement between the sensitivity measured in the simulation and in the experimental cases, for both set-ups. In fact, the sensitivity of the simulated standard EI and SM-EI set-ups were also $280 \pm 10\, nrad$ and $350 \pm 10\, nrad$, respectively. While this should be expected given the agreement in the simulated profile and the inclusion of the appropriate level of noise, it further confirms the accuracy of the proposed model. It also means that the standard EI set-up remains more sensitive than its single-mask counterpart, despite the increase in photon statistics. This experimental validation means that this model can be reliably used to study how the sensitivity varies as a function of the detector PSFs.

5.3.4 Predicting sensitivity

From Figure 5-7, we concluded that using the detector mask is equivalent to the use of an ideal detector PSF. Therefore, if the total exposure time is kept constant (SM_2) it is possible for the sensitivity of the SM-EI set-up to overtake that of the standard EI set-up at a certain smaller values of σ_{PSF}. As σ_{PSF} decreases, the sensitivity is expected to increase as the slopes of the PSF, and therefore the IC become steeper. Hence, a study of the sensitivity as a function of the width of σ_{PSF} was undertaken, using the same parameters of the experimental set-up discussed in the previous section.

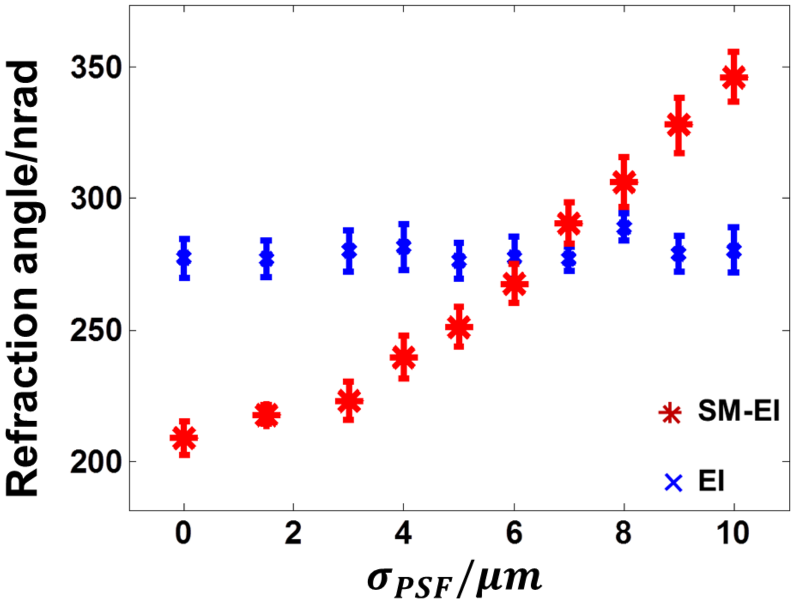

Figure 5-12 The refraction sensitivity is plotted against different values of σ_{PSF}, which are convolved with an ideal pixel function, for both standard and SM-EI set-ups.

Figure 5-12 shows that, for the SM-EI set-up, there is a gradual increase in the sensitivity as σ_{PSF} decreases, as expected. In this configuration, the SM-EI set-up becomes more sensitive to refraction than the standard EI set-up when $\sigma_{PSF} \leq 5\ \mu m$. As should be expected, when using the ideal pixel PSF ($\sigma_{PSF} = 0$), the sensitivity of the SM-EI set-up becomes approximately $\sqrt{2}$ times better than the standard EI set-up, which is due to the increase of a factor of 2 in the detected statistics. Also as expected, the sensitivity of the standard EI remains constant over the range of PSFs simulated, which is consistent with the previous observations that the detector mask reproduces the effect of an “ideal” pixel. As is obvious from the above, this analysis was carried out for SM_2 only, for which the exposure time is kept constant across both set-ups; if SM_1 were used, then one would expect the sensitivity of SM-EI to converge to that of standard EI for $\sigma_{PSF} = 0$.

5.4 Summary

The standard EI set-up possesses many advantages as a DPI method. However, its reliance on two images, acquired with two separate exposures, while the sample mask has to be moved in order to retrieve absorption and differential phase, makes it susceptible to errors arising while re-positioning masks and, generally speaking, makes the entire acquisition procedure more complex. These errors can be mitigated by using an approach which allows for the simultaneous acquisition of two mixed intensity images in a single-shot. This would also have other potential advantages, related to dose and/or exposure time reduction, and make the technique more robust against misalignment errors.

In this chapter, a single-shot technique is realised by eliminating the detector mask of the standard EI system, and using the detector pixels to directly sense the refraction-induced beam displacement. The SM-EI set-up is very similar to the skipped, double mask standard set-up, which means it could provide an alternative use of the same system for some applications, in addition to an alternative design.

In comparison to beam tracking [Vittoria et al. 2015b], only phase and absorption information can be retrieved with the current SM-EI system, but with the significant advantage that very small pixel sizes, possibly incompatible with e.g. clinical imaging, are not required. Moreover, modifications of the system can be envisaged where an appropriately designed mask creates beamlets falling over three pixels, in a way that allows for the retrieval of three signals.

Both single and standard (double mask) set-ups were used to acquire images of a wire sample with a laboratory source. Mixed-intensity profiles of both strongly and weakly refracting/absorbing samples were selected and compared against those generated with the wave optics simulation for both the standard EI and SM-EI set-ups. The simulation was designed to accurately model both set-ups so that it could also be used to determine parameters of the system, such as mask thickness. The thickness of the pre-sample mask septa was determined to be thinner than its nominal value. This led to a higher offset in the SM-EI IC, which in turn caused inaccuracies in the phase retrieval algorithm.

In fact, the inaccuracies introduced by the high SM-EI IC offset were attributed to beam hardening effects, which occur when the beam spectrum passing through the mask septa and apertures undergo additional hardening by a sample with non-negligible absorption. This led to differences in the phase retrieved profiles extracted from the data acquired with the two systems. To further study the negative effects of the thin masks in detail, an SM-EI set-up with thick pre-sample mask septa was also simulated. In this case, both EI configurations give identical results, matching the theoretical differential phase profiles. This provided additional validation that the errors on the differential phase profile extracted from the experimental data, acquired with the SM-EI set-up, were due to the use of excessively thin pre-sample masks.

The sensitivity of the two systems was measured experimentally and estimated via simulation; the obtained values were found to be in agreement. The simulation model was then used to predict the sensitivity of the SM-EI set-up as a function of detector PSF. This showed that the SM-EI set-up becomes more sensitive than the standard one as the detector tends toward ideal behaviour. This is thanks to the increased number of photons impinging on the detector combined with an increasingly steeper PSF slope. In the SM-EI set-up, the sensitivity with which the beam's displacement is detected depends on the slope of the detector PSF. Hence the IC of such a system, and ultimately its sensitivity, depends on the detector used.

Ultimately, it was determined that laboratory implementations of the SM-EI set-up could be improved in the future by using detectors where $\sigma_{PSF} \leq 5\ \mu m$ and employing a sample mask with thicker septa. A system realised using the above modifications could be more sensitive to refraction than its standard EI counterparts, although such a claim warrants further investigation. The clear benefits from such a set-up lie in its simplicity and increased insensitivity against misalignments; however, it imposes the use of a skipped mask, which results either in a resolution decreased by a factor of 2, or in the use of twice as many dithering steps to achieve the same resolution as the non-skipped standard EI set-up.

Chapter 6 Two-directional edge illumination

6.1 Overview

The EI method has been shown to be a flexible XPCI method. In previous chapters we have shown how the sensitivity of the set-up may be optimised, as well as how the set-up can be simplified. However, both these set-ups are still only sensitive to refraction which occurs in one direction, i.e. perpendicular to mask lines. This means that the orientation of the sample in the set-up has an effect on the ultimate image quality, since the set-up is insensitive to photons which are refracted parallel to the mask lines.

One-directional phase sensitivity is a typical disadvantage of many XPCI techniques. In fact, aside from FSP, earlier implementations of all other XPCI techniques were inherently phase sensitive in only one direction, and although in recent years 2D implementations of GI have emerged [Zanette et al. 2010; Kottler et al. 2007; Nagai 2014; Wen et al. 2010], none of these enabled maintaining high phase sensitivity without sectioning and/or collimating an extended source at the source plane [Sato et al. 2011].

The simplest way of achieving two-directional refraction sensitivity is to acquire one image with a one-directionally sensitive set-up, and then rotate the sample (or object) by $90°$ and acquire a second one. In this way, features which are invisible in the first image become visible in the second by virtue of their orientation, and vice-versa. While this can also be done with the standard EI set-up, it introduces a large margin for error in placing the sample, and it can also potentially introduce an additional step to image processing because the images may need to be registered.

Furthermore, it doubles both acquisition time and dose to the sample, making it unrealistic for numerous real-world applications. Therefore, the ability to produce images which display features oriented along two-directions in a single-shot is crucial to future implementations of EI.

To achieve this, a new set of test structures was designed, consisting of periodic L-shaped apertures. This unusual aperture shape was selected so that the EI condition could be realised simultaneously along two orthogonal pixel edges, while at the same time maximising the number of photons incident on the pixel. However, it must be noted that a number of other aperture shapes are similarly capable of fulfilling the EI condition in 2D. The new test structures had been previously tested at the BM5 beamline at the European SR facility, in a pilot study which demonstrated that single-shot two-directional sensitivity could be achieved without needing to rotate the sample or the imaging system [Olivo et al. 2009]. In this chapter, we describe a much more detailed follow-up study with a polychromatic conventional x-ray tube, which aims to study this novel 2D EI set-up, its IC and to demonstrate its quantitative phase retrieval and USAXS imaging capabilities. This was implemented for EI in 2D for the first time in this work.

6.2 Modelling a 2D EI set-up

To commence this work, a model of the 2D EI set-up was created using the Monte Carlo ray-tracing package, McXtrace. The model was used to study the shape of the 2D EI IC and to guide the alignment of the set-up. Subsequently, a novel 2D phase retrieval algorithm was developed, and in order to verify its quantitative accuracy, experimental work was carried out using a pair of crossed PMMA cylinders. Finally, the algorithm was extended to retrieve scattering signal in 2D, and a pair of crossed wooden splints was used as a scattering sample.

6.2.1 L-Shapes Masks

The L-shapes were modelled by modifying the existing code for the 1D masks, which are currently used in the laboratory and had been modelled by Millard et al [Millard et al. 2013]. In a similar fashion, we express the intensity of the flat field, i.e. in the presence of the masks but without the sample, as follows:

$$I(x,y) = I_0 \times T(x,y), \tag{6-1}$$

where I_0 is the intensity incident on the detector in the presence of the mask. The transmission function, $T(x,y)$, can be described by defining two functions, $t(\mathbf{e}_\mathrm{n})$ and Γ in Cartesian space defined by:

$$\mathbf{e}_\mathrm{n} = \{(x,y), \in \mathbb{R}^2\}, \tag{6-2}$$

$$\text{where, } \mathrm{t}(\mathbf{e}_\mathrm{n}) = \cos\left(\frac{2\pi \boldsymbol{e}_n}{p}\right); for\ n = 1{,}2, \tag{6-3}$$

$$\mathrm{t}(\mathbf{e}_\mathrm{n}; w) = \cos\left(\frac{2\pi(\boldsymbol{e}_n + w)}{p}\right); \tag{6-4}$$

$$\text{and, } \Gamma = \cos\left(\frac{\pi w}{p}\right). \tag{6-5}$$

The functions, $t(\mathbf{e}_\mathrm{n})$ and $t(\mathbf{e}_\mathrm{n}; w)$ can be combined to define the shape of the mask apertures, while Γ is the arbitrary boundary condition which defines opaque and transparent regions in Cartesian space. The aperture widths can be varied by changing the shifting parameter w, and p defines the mask period. Hence, we define the mask transmission function, $T(x,y)$, by combining the above expressions in the following way:

$$T(x,y) = \begin{cases} 1, & if\ \ t(\boldsymbol{e}_1) \wedge t(\boldsymbol{e}_2) > \ \ \Gamma,\ t(\boldsymbol{e}_1; w) < \Gamma \wedge t(\boldsymbol{e}_2; w) < \Gamma; \\ 0, & \qquad\qquad\qquad\qquad otherwise. \end{cases} \qquad \textbf{(6-6)}$$

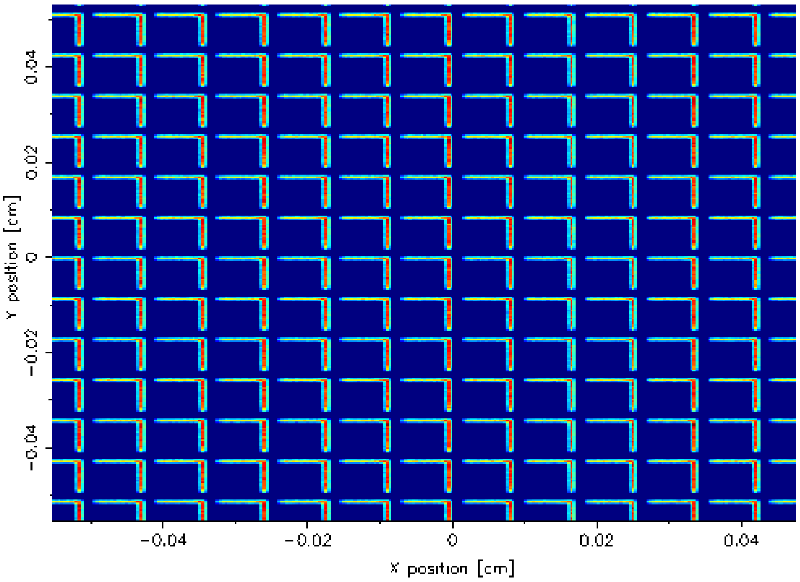

Figure 6-1 Simulated L-shaped mask with $\mathbf{83.5}\ \boldsymbol{\mu m}$ ***period and*** $\mathbf{11}\ \boldsymbol{\mu m}$ ***aperture size, obtained by using Eqns. (6-2)-(6-6)***.

In Eqn. (6-6), the masks are modelled to be completely opaque in order to save computation time while performing the simulations. One example of a simulated X-ray transmission image of an L-shaped mask, with period $83.5\ \mu m$ and aperture size $11\ \mu m$, is displayed in Figure 6-1. The image is a result of modelling the mask using Eqns. (6-2)-(6-6), and then simulating an X-ray image of them using McXtrace package.

6.2.2 Predicting the 2D Illumination curve

Since the aperture shape represents a novel geometry, the simulation was first used to predict the shape of the IC, which was then used to inform the experimental work, where mask alignment is complicated by practical issues such as mask imperfections, bad detector pixels and limited X-ray statistics, and therefore significantly benefits from guidance through an “ideal” image. The alignment procedure is performed on a regular basis with the 1D mask and is done fairly quickly. However, use of L-shaped apertures means there are more degrees of possible misalignment, which makes the 2D alignment more time-consuming. Hence, in order to speed up the experimental work and future alignments, detector illumination distributions, resulting from a series of misaligned set-ups, were studied with the simulation.

In particular, the effects of two types of misalignment were independently studied. The first series of tests consisted of a number of rotations of the sample mask about the z-axis, ϕ. The second study involved a number of sample mask translations along the beam axis (z-direction). Note that, in the general case, misalignment in these (and other) parameters can be combined to analyse multiple misalignments at the same time, thereby simulating more realistic conditions. However, the combined effect of these misalignments would be entangled, leading to the misalignment surfaces which would be difficult to interpret. Finally, although the study focused solely on the sample mask misalignments, the same principles can be used to align the detector mask to the detector. In fact, the focus on the sample mask is due to the increased difficulty in aligning it in the lab since it is farther away from the detector.

Hence, in the simulation, for the sake of simplicity, the detector mask was perfectly aligned with the detector. For each misalignment, the sample mask was raster scanned with respect to the aligned detector mask to obtain an IC, which is, in this case, a 2D surface rather than a curve. Subsequently, new metrics, hereafter called alignment surfaces, were generated by analysing the ICs of each pixel to determine its position of maximum illumination. The IC maxima for each pixel are then plotted as a surface, every point of which corresponds to a detector pixel. For a perfectly aligned set-up, all pixels “see” the same maximum position; hence, the flatness of the surface is an indication of the alignment. Conversely, misalignment produces patterns in the surface, which can be used to uniquely identify the type and degree of misalignment.

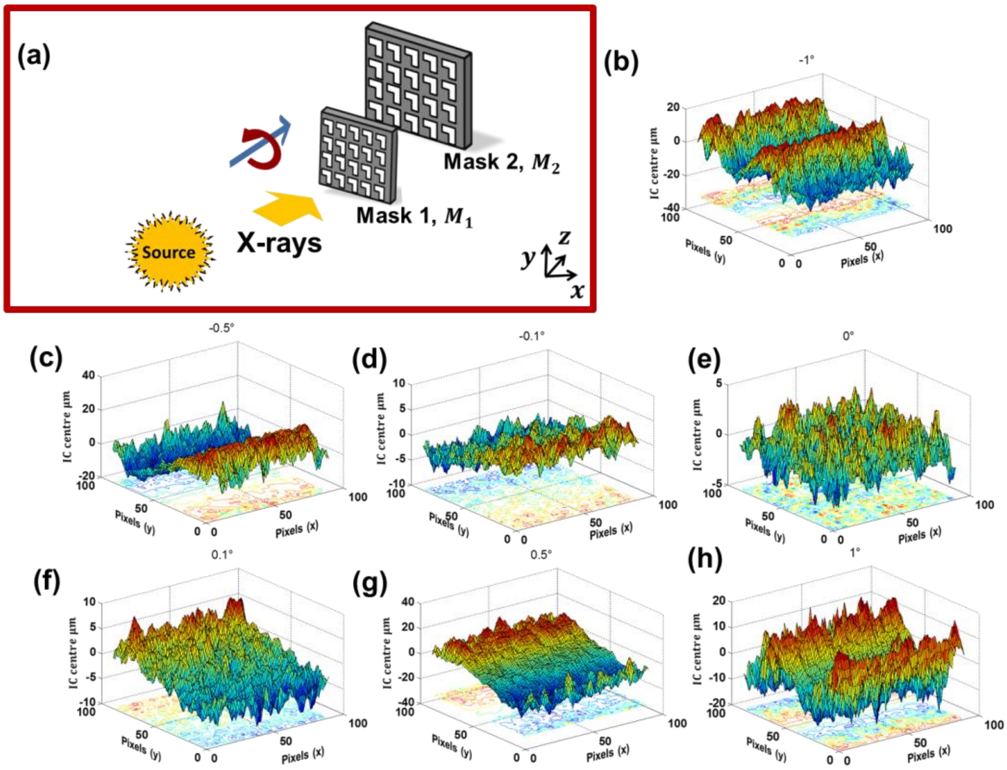

Figure 6-2 (a) A 2D EI set-up with the sample mask misaligned by rotation about the z-axis; (b)-(h) show the misalignment surfaces for various degrees of misalignment.

For example, in Figure 6-2, the result of a misalignment in ϕ is a gradient in the surface along the y-direction, however, at more extreme misalignments, e.g. Figure 6-2(b), (c), (g) and (h), this gradient repeats itself in a periodic fashion; this happens when the patterns in the two masks are out of phase with each other by more than one period. Figure 6-3 depicts a set-up misaligned caused by translation of the mask along the beam axis, and it gives rise to a slope in the x-direction on the surface.

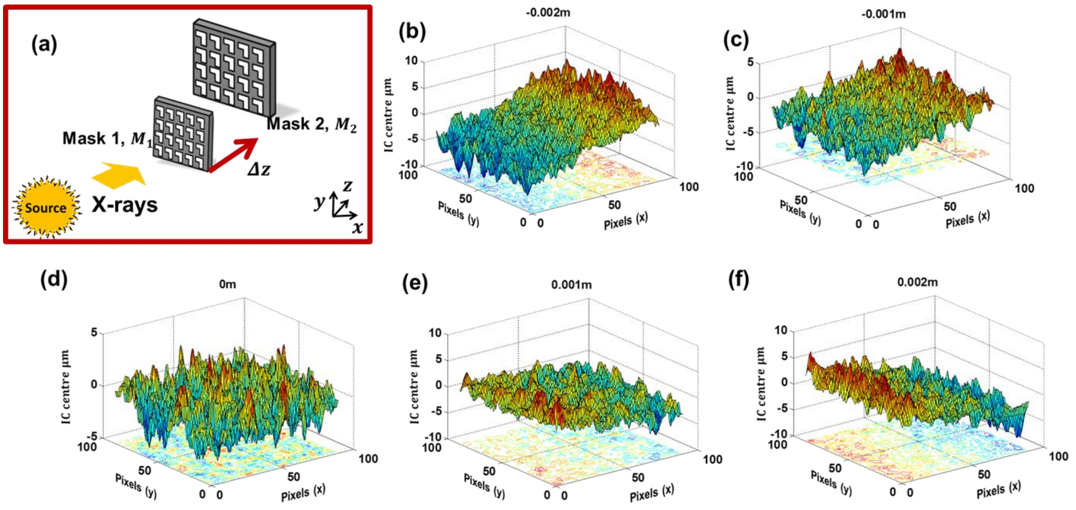

Figure 6-3 (a) A 2D EI set-up with the sample mask misaligned by translation along the z-axis; (b)-(h) show the misalignment surfaces for various translations.

There are two important observations which can be made from Figure 6-2 and Figure 6-3. Firstly, the alignment surfaces observed on opposite sides of a perfectly aligned set-up (e.g. Figure 6-2(e) and Figure 6-3(d), respectively), are symmetric for an equal degree of misalignment in opposite directions. Secondly, at the positions of perfect alignment, the surface is flat (on average), and any fluctuations is due to statistical noise present in the Monte Carlo method.

Finally, a perfectly aligned system was then used to simulate the IC by raster scanning the sample mask with respect to the detector mask and detector. The IC shown in Figure 6-4 is a result of averaging over multiple pixels in order to reduce the noise present in the data.

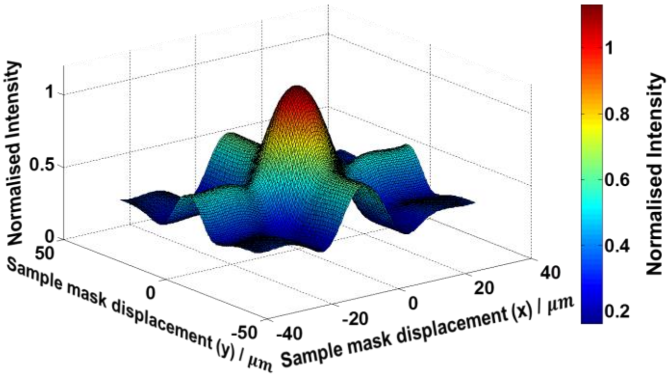

Figure 6-4 A simulated illumination curve obtained using McXtrace with the mask parameters and the experimentally measured source size given as input.

The IC was used to develop a phase retrieval algorithm, which was used to separate the absorption and refraction in two directions. Analysis of its slopes was also key to selecting the optimal positions of the pre-sample mask at which the images, which have been given as input to the phase retrieval algorithm, are collected.

6.3 2D Phase and Scattering Retrieval

6.3.1 Phase Retrieval

Given the IC $L(x, y)$, the detected intensity in the presence of a negligibly scattering sample can be expressed as follows:

$$I(x, y) = I_T L(x + \Delta x_r; y + \Delta y_r), \qquad \textbf{\textit{(6-7)}}$$

where I_T is the intensity transmitted through the sample, $\Delta x_r = z_{od} \Delta\theta_{r,x}$ and $\Delta y_r = z_{od} \Delta\theta_{r,y}$ are the lateral shifts suffered by the beam, z_{od} is the object-to-detector distance and $\Delta\theta_{r,x}$ and $\Delta\theta_{r,y}$, are the refraction angles in the x and y directions, respectively. To develop this algorithm, we exploited the similarity between EI and ABI [Munro et al. 2013], and extended the method developed by Rigon et al [Rigon et al. 2007] to perform a first-order, two-dimensional Taylor expansion, assuming small refraction angles. In order to retrieve three parameters, i.e. absorption and refraction in x and y, three linearly independent equations can be written using three input images, I_{1-3} acquired at different points on the IC.

The algorithm may be rewritten with matrix notation:

$$\begin{bmatrix} I_1 \\ I_2 \\ I_3 \end{bmatrix} = I_T \underbrace{\begin{bmatrix} L_1 \; L_1^x \; L_1^y \\ L_2 \; L_2^x \; L_2^y \\ L_3 \; L_3^x \; L_3^y \end{bmatrix}}_{= M} \begin{bmatrix} 1 \\ \Delta x_r \\ \Delta y_r \end{bmatrix}, \tag{6-8}$$

where L_n^j indicates $\partial L_n / \partial j$ at positions $n = 1,2,3$ on the IC.

Equation (6-8) is a linear set of equations which can be solved analytically to retrieve the three output images $I_{T,}$ $\Delta\theta_{r,x}$, and $\Delta\theta_{r,y}$:

$$I_T = \frac{\mathrm{I_1(L_2^xL_3^y - L_3^xL_2^y) + I_2(L_3^xL_1^y - L_1^xL_3^y) + I_3(L_1^xL_2^y - L_2^xL_1^y)}}{\mathrm{det(M)}}, \tag{6-9}$$

$$\Delta\theta_{r,x} = \frac{\Delta x_r}{z_{od}} = \frac{\mathrm{I_1(L_3L_2^y - L_2L_3^y) + I_2(L_1L_3^y - L_3L_1^y) + I_3(L_2L_1^y - L_1L_2^y)}}{\mathrm{I_Tdet(M)}}, \tag{6-10}$$

$$\Delta\theta_{r,y} = \frac{\Delta y_r}{z_{od}} = \frac{\mathrm{I_1(L_2L_3^x - L_3L_2^x) + I_2(L_3L_1^x - L_1L_3^x) + I_3(L_1L_2^x - L_2L_1^x)}}{\mathrm{I_Tdet(M)}}. \tag{6-11}$$

Equations (6-9)-(6-11) impose no restrictions on the positions at which the images are acquired, as long as the three equations are linearly independent [Rigon et al. 2007]. However, images were only acquired on linear regions of the IC because even small angles can violate the linear approximation at the peak of the IC. In addition to the work performed in chapter 4, previous studies performed both in ABI

[Rigon et al. 2007] and in EI [Diemoz et al. 2013a], have shown that that certain positions leads to a better SNR.

Finally, it has been previously stated that differential phase images can prove difficult to interpret due to the dark and bright fringes present in the images. This can make images appear even more complex in the case of 2D sensitivity. On the contrary, phase integrated images are much easier to interpret, since they are similar to conventional X-ray images, while benefitting from the increase in contrast inherent with XPCI techniques. In the 1D case, direct integration of a refraction image yields the phase of the object accompanied by severe streak artefacts [Kottler et al. 2007; Arnison et al. 2004]. Moreover, in cases of unknown boundary conditions, e.g. when the object is larger than the field of view, 1D phase integration may not be possible. In recent years, Arnison et al 2004 [Arnison et al. 2004] and Kottler et al, 2007 [Kottler et al. 2007] demonstrated that the two differential phase images obtained from a 2D sensitive XPCI set-up can be combined in Fourier space to retrieve the phase $\Phi(\mathrm{x}, \mathrm{y})$, without unfavourable artefacts, and regardless of the boundary conditions. This was achieved by performing the Fourier transform of the complex sum of the two differential phase images in Fourier space, dividing it by their spatial frequencies (k, l), and then taking the inverse Fourier transform:

$$\Phi(x, y) = \mathcal{F}^{-1}\left[\frac{\mathcal{F}\left[I_{\theta_{r,x}} + iI_{\theta_{r,y}}\right]}{2\pi(k + il)}\right](x, y), \qquad \textbf{\textit{(6-12)}}$$

where $\mathcal{F}$ and $\mathcal{F}^{-1}$ represent the Fourier and inverse Fourier transformations, respectively, and $I_{\theta_{r,x}}$ and $I_{\theta_{r,y}}$ are the refraction images in their respective directions.

6.3.2 2D Scattering Retrieval

Furthermore, the two-directional USAXS signal can be retrieved by using an extended version of the phase retrieval algorithm. Scattering is assumed to be a stochastic process taking place at the sub-pixel scale, where each pixel integrates over a given probability distribution of scattering angles $S(\Delta\theta_{s,x,y})$. To first approximation, the distribution of scattering angles collected by each detector pixel can be modelled as a normalised Gaussian centred at zero, [Rigon et al. 2003; Rigon et al. 2007] i.e. $\int_{\frac{w}{2}}^{-\frac{w}{2}} S\big(\Delta\theta_{s,x,y}\big)\, d(\Delta\theta_s) = 1$, $\int_{\frac{w}{2}}^{-\frac{w}{2}} (\Delta\theta_s) S\big(\Delta\theta_{s,x,y}\big)\, d(\Delta\theta_s) = 0$. Moreover, its width is be represented by its standard deviation, which can be expressed as follows, $\sigma^2_{\Delta\theta_{s,x,y}}(x,y) = \int_{\frac{w}{2}}^{-\frac{w}{2}} (\Delta\theta_s)^2 S\big(\Delta\theta_{s,x,y}\big)\, d(\Delta\theta_s)$. An increase in this quantity is linked to the physical broadening of the beam due to the scattering by the sample. The integration limits specify that the scattering distribution is collected over the extent of one pixel, where w represents the size of the pixel.

To some extent the choice of a Gaussian function can be considered as fairly arbitrary; however, previous work on 1D-EI has shown that, at least to first approximation, a Gaussian function can be used to fit the retrieved scattering function [Millard et al. 2013]. Hence, considering the preliminary nature of this investigation, we have simply extended that treatment to the 2D case.

A 2D second-order Taylor expansion can be used to describe the effect of scattering and refraction on the measured intensity in the following way:

$$I_n = I_T[L_n + L_n^x \Delta x_r + L_n^y \Delta y_r \ + (L_n^{xx} \underbrace{\frac{1}{2}(\Delta x_r^2 + \sigma_x^2)}_{x_{s,r}} + L_n^{yy} \underbrace{\frac{1}{2}\left(\Delta y_r^2 + \sigma_y^2\right)}_{y_{s,r}} + L_n^{xy} \Delta x_r \Delta y_r)], \quad \textbf{\textit{(6-13)}}$$

where $L_n^{j,k}$ now indicates $\partial^2 L_n / \partial j \partial k$ at $n = 1 - 6$ positions on the IC, where one image may be acquired at the IC peak. The first three terms within the brackets in Eqn. (6-13) have the same meaning as in Eqn. (6-8). The new quantities, $\sigma_x = z_{od} \sigma_{\Delta\theta_{s,x}}$ and $\sigma_y = z_{od} \sigma_{\Delta\theta_{s,y}}$, represent the broadening of the IC caused by scattering. Note that σ_x is a distance while $\sigma_{\Delta\theta_{s,x,y}}$ represents an angle.

There are five unknown variables to retrieve, but in order to derive an analytical solution we treat the final term, $\Delta x_r \Delta y_r$, as an additional independent variable, thus imposing the need for six input images. However, by exploiting the relationship between this final mixed term and the previous ones, an approach could be developed where only 5 input images are required instead of 6. This may be the focus of future work.

The system can then be solved in a similar manner to Eqn. (6-8), which enables the extraction of the two-directional scattering quantities:

$$\sigma_{\Delta\theta_{s,x}}^2 = \left(\frac{\sigma_x}{z_{od}}\right)^2 = \frac{2x_{s,r} - (\Delta x_r)^2}{z_{od}^2}, \quad \textbf{\textit{(6-14)}}$$

$$\sigma_{\Delta\theta_{s,y}}^2 = \left(\frac{\sigma_y}{z_{od}}\right)^2 = \frac{2y_{s,r} - (\Delta y_r)^2}{z_{od}^2}. \quad \textbf{\textit{(6-15)}}$$

6.4 Laboratory Implementation

The experimental verification of the proposed method was performed using a rotating anode, Mo-target source (Rigaku 007HF) operated at $35kVp,\ 25\,mA$. The 2D masks were manufactured by Creatv Microtech according to an earlier design [Munro et al. 2011]. The periods of the sample and detector mask were $p_1 = 120\,\mu m$ and $p_2 = 166\,\mu m$, with aperture sizes of 11 and $15\,\mu m$ respectively. The absorbing regions of these masks consist of a $30\,\mu m$ layer of gold, which was electroplated upon a $500\,\mu m$ thick graphite substrate. The proof-of-concept nature of this work meant that these first masks possessed thinner septa ($\sim 30\,\mu m$ of gold) than some of their corresponding 1D counterparts, e.g. the masks used in Chapter 4 had $150\,\mu m$ nominally thick septa. Hence, there was a comparative increase in X-ray transmission through the mask septa, and therefore, added background noise was collected in the images.

6.4.1 Demonstration of two-directional phase sensitivity through crossed-PMMA cylinders

The experimental set-up is shown in Figure 6-5(a). The two L-shaped masks, M_1 and M_2, were aligned with the detector pixels and with each other. The alignment surfaces were used to inform this process and their study was instrumental in speeding up alignment in the laboratory. The sample and detector masks were placed at $1.44\,m$ and $1.99\,m$ away from the source, respectively. The distances were selected in order to match the projected mask periods to the "skipped" detector pitch, i.e. to illuminate every other pixel [Ignatyev et al. 2011]. To achieve this skipped EI configuration for the Anrad SMAM detector, which has $85\,\mu m$ square pixels, the detector was placed $2.04\,m$ away from the source. The sample was then placed at a plane immediately after the sample mask, at $1.47\,m$ away from the source. This ensured approximately unit magnification between these two planes, such that both the IC and refraction from the sample could be measured in approximately similar conditions.

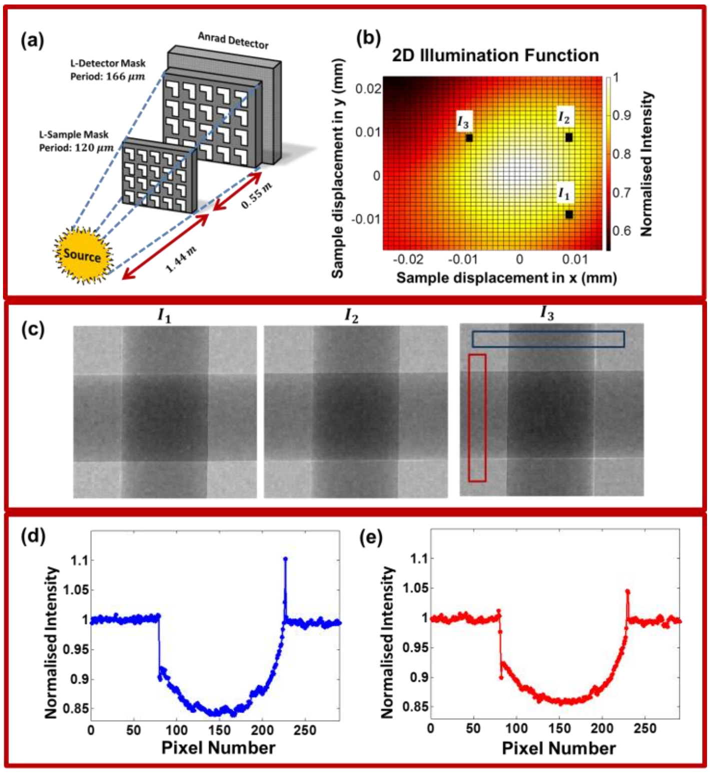

Figure 6-5 (a) Schematic of the experimental 2D EI set-up, (b) IC acquired by scanning the sample mask over a span of $40\,\mu m$ in both x and y directions, and (c) the three mixed intensity images obtained at the three positions highlighted on the IC in (b). Profiles are plotted across the vertical (d) and horizontal (e) cylinder from I_3.

To obtain the experimental 2D-IC shown in Figure 6-5(b), the pre-sample mask was scanned (with the detector mask held fixed) over a span of $40\,\mu m$ in $8\,\mu m$ steps in the x-direction and $5\,\mu m$ steps in y. The pre-sample mask was then placed at the three different imaging positions, which correspond to those shown on the IC in Figure 6-5(b), where images of a pair of crossed PMMA cylinders (radii $1.5 \pm 0.1\,mm$, as measured from the image) were acquired. The three mixed intensity projections are displayed in Figure 6-5(c). Since the set-up is two-directionally sensitive, both PMMA cylinders are simultaneously visible in each of the three mixed intensity images. Additionally, the spatial resolution of each image was improved via dithering, i.e. scanning the sample with 6×6 sub-pixel steps of $20\,\mu m$, in both x and y directions (exposure time = 10s / dithering step).

The absorption signal remains the same in I_1, I_2 and I_3, however, the refraction signal induced by each cylinder changes across the three images. In particular, the refraction signal depends on the position at which the sample mask was placed when the image was acquired. For example, to acquire I_1 the mask was placed at some position (+x,-y), which has been marked in the lower right corner of the IC in Figure 6-5(b). Since this position corresponds to a positive x-coordinate, in this image the bright edge of the vertical cylinder precedes the dark edge (left-to-right in I_1). In addition, at this position the y-coordinate of the sample mask is negative; therefore, for the horizontal cylinder, the bright edge appears at the top while the dark edge appears at the bottom of the image. Conversely, the order in which the bright and dark edges appear reverses in I_3 for both cylinders. This is because I_3 was acquired with the sample mask placed at another position (-x,+y), in the upper left corner of the IC. Note that the I_3 position corresponds to a negative x-coordinate and a positive y-coordinate, i.e. the exact opposite of the I_1 position.

Profiles were extracted from the vertical and horizontal cylinders in I_3 and were plotted in Figure 6-5(d) and (e), wherein the bright and dark edges manifest as positive and negative peaks, respectively. It is more obvious in Figure 6-5(d) and (e) that the positive peak appears after the negative peak for both cylinders, as previously described. This shows the opposite case for the signal described in I_1, where the positive peak instead precedes the negative peak. Similarly, a profile taken across the cylinders in I_2, which corresponds to a (+x,+y) position would preserve the order of the peaks for the vertical cylinder, with respect to I_1, but the signal from the horizontal cylinder would be inverted (since the y-coordinate is positive at this position).

Additionally, it is important to note that the loss of photons from the absorption of the cylinders is much greater than the loss of photons due to negative refraction; therefore, the signal from the latter seems to be obscured by the presence of the former in the mixed intensity profiles. Thus, the negative peak can be difficult to see.

The mixed intensity images in Figure 6-5(c) and equations (6-9)-(6-11) were then used to perform the phase retrieval procedure, the results of which are displayed in Figure 6-6. Figures 6.6(a)-(c) show the retrieved transmission and refraction angle images in the two orthogonal directions. In fact, the image in Figure 6.6(a) may be more accurately described as an “apparent absorption” image, due to the residual phase enhancement peaks which are present at the very edges of the wire. These peaks have been highlighted in the experimental profile shown in Figure 6.6(d). These residual peaks occur because the slowly varying phase assumption of the algorithm is not satisfied at the very edges of an object [Oltulu et al. 2003]. Despite this minor error, Figures 6.6(d)-(f) show a good agreement between the retrieved and theoretical profiles for the “apparent absorption” and refraction images of the PMMA cylinders, which demonstrates the overall quantitative accuracy of the approach. In particular, it is also worth noting that the horizontal and vertical wires disappear in Figure 6.6(b) and Figure 6.6(c), respectively, since they induce refraction only along “non-retrieved” directions.

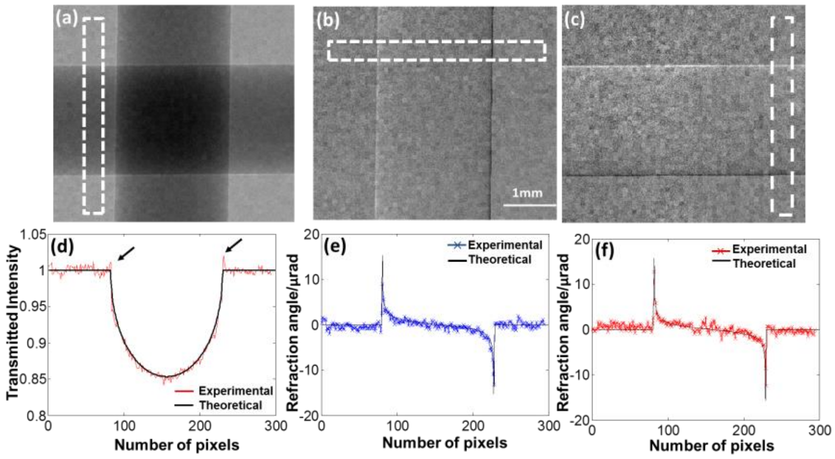

Figure 6-6 Retrieved images for two crossed PMMA cylinders; (a) transmission, (b) refraction image along the horizontal direction and (c) refraction image along the vertical direction. Comparisons between the experimental and theoretical profiles are shown for (d) transmission (e) refraction along the horizontal direction, and (f) refraction along the vertical direction.

Moreover, the differential phase images in Figure 6-6(b) and (c) can be used to calculate integrated phase images. When this calculation is performed using only one refraction image, e.g. either Figure 6-6(b) or (c), and phase integration is performed only along the direction of refraction sensitivity, streak artefacts tend to appear in the resultant phase image. The presence of these artefacts is attributed to the propagation of image noise, which is inconsistent in the direction orthogonal to the direction of integration, i.e. in the “non-retrieved” direction. Examples of this are displayed in Figure 6-7, where Figure 6-6(b) and (c) were treated independently. In both cases, integration was performed only along the direction of refraction sensitivity, thereby producing two separate phase images, which are comparable to two cases of direct 1D integration.

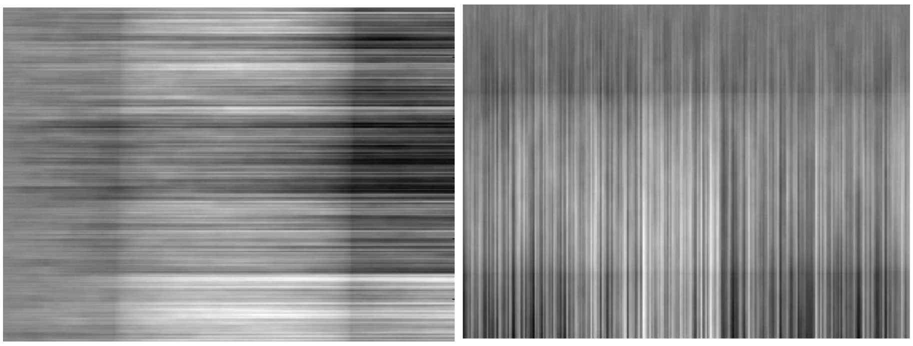

Figure 6-7 One directional phase images obtained from the differential phase contrast images showed in Figure 6-6, integrated along the x and y directions, respectively. These images display severe streak artefacts.

By comparison, in the case of 2D integration, the phase image $\boldsymbol{\Phi}(\boldsymbol{x},\boldsymbol{y})$ can be calculated by combining both differential phase images, which are shown in Figure 6-6(b) and Figure 6-6(c), and using them as inputs in Eqn. (6-12). The resultant image of the 2D integration procedure is displayed in Figure 6-8(a). Average phase retrieved profiles are displayed in Figure 6-8(b) and Figure 6-8(c), where they are also compared against the theoretically calculated values.

As can be seen, phase integrated images obtained by using the Fourier method in Eqn. (6-12) are free of the streak artefacts common to 1D phase integration. However, the image is affected by some low frequency artefacts, which can be potentially caused by an asymmetry in the differential phase profile. Previous work on EI has shown that this asymmetry may be the result of object under-sampling [Hagen et al. 2014]. For example, this can occur when an insufficient number of dithering steps is used to sample the refraction peaks, leading to retrieved differential phase profiles which are asymmetric.

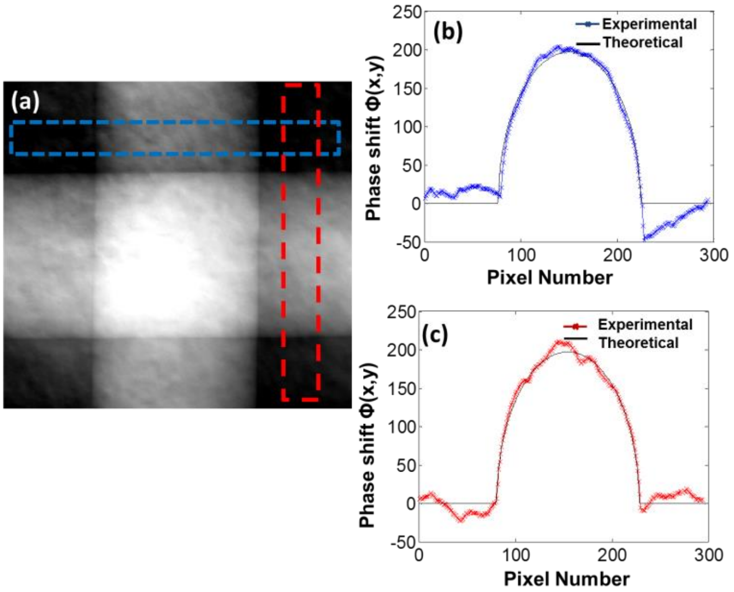

Figure 6-8 (a) Integrated phase image of the crossed PMMA cylinders calculated using the Fourier method on the two differential phase images in Figure 6-6 ***(b) and (c). (b) and (c) show the average horizontal and vertical phase integrated profiles extracted from the regions in (a) respectively, compared to the expected theoretical values.***

Moreover, the denominator in Eqn. (6-12) acts as a high frequency filter in Fourier space, which amplifies low frequencies and has been known to impose an artificial background on the image [Scherer et al. 2014]. Indeed, these artefacts are a known problem in phase integration, and they have already been discussed by Langer et al [Langer et al. 2010]. They can be eliminated by using a priori information on the sample geometry, or a regularization-based algorithm [Zanette et al. 2014].

6.4.2 Demonstration of two-directional USAXS sensitivity through wooden splints

Finally, in order to experimentally validate the retrieval method for scattering, an additional experiment was performed with two orthogonally overlapping pieces of wood, which are known to produce a strong scattering signal. Using Eqns. (6-13)-(6-15), the “apparent absorption”, 2-directional refraction and scattering images were retrieved and are displayed in Figure 6-9.

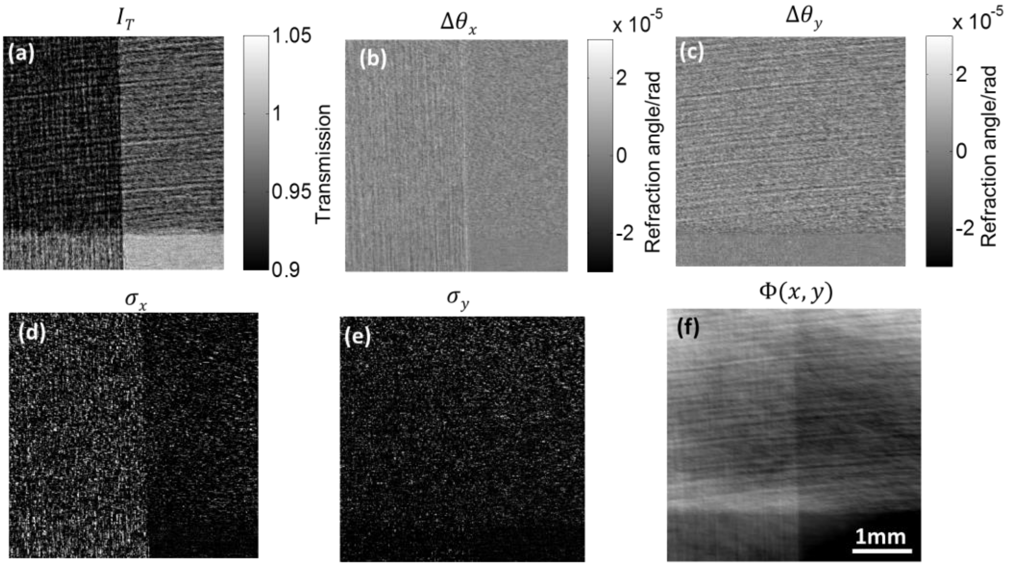

Figure 6-9 Retrieved images for a pair of wooden splints for (a) transmission, (b) refraction along the horizontal direction, (c) refraction along the vertical direction, (d) scattering along the horizontal direction, (e) scattering along the vertical direction, and (f) the phase image calculated from the two refraction images (b) and (c).

Figure 6-9 (a)-(c) show the transmission and refraction images, while Figure 6-9(d) and Figure 6-9(e) show a map of the squared FWHM of the scattering distribution in the x and y directions, respectively. As can be seen, the phase signal is stronger along x than along y. This can be attributed to the differences in the source size along the respective directions, which, according to Eqn.(4-1) and Eqn. (5-1) lead to different differential phase sensitivities [Diemoz et al. 2013a]. In addition, the microstructure of the wood exhibits a strong anisotropy, with features orientated along preferential directions, giving rise to significantly different refractive/scattering intensities in the two directions. In particular, the horizontal structures tend to disappear in Figure 6-9(b) and Figure 6-9(d), while the same occurs for the vertical structures in Figure 6-9(c) and (e). Both signatures are visible in Figure 6-9(f), which shows the phase integrated image of the crossed wooden splints, which was calculated by using the two differential phase images in Figure 6-9(b) and (c) and Eqn. (6-12). However, the signal is stronger for features oriented vertically due to the aforementioned source asymmetry.

6.5 Summary

In this chapter, a laboratory implementation of the EI XPCI technique has been described, which was then shown to be capable of achieving 2D phase and dark-field sensitivity while using a conventional X-ray source. The 2D EI set-up was realised using two masks with L-shaped apertures, and was first modelled using a Monte Carlo ray-tracing simulation package. In the simulation, L-shaped masks were modelled as completely X-ray opaque. A study of the set-up alignment was undertaken and used to optimise and inform the corresponding experimental procedure. In addition, this model was used to predict the shape of the IC, which was then used as a benchmark in the experimental framework.

By exploiting the similarity between ABI and EI, an algorithm was developed to resolve the refraction and scattering signals in both directions. As well as providing additional information compared to its standard (one-directionally sensitive) EI counterpart, the 2D-EI set-up addresses some disadvantages inherent in its predecessor. In particular, phase maps of the sample can be obtained by combining the differential phase images acquired in the two-directions simultaneously; this eliminates the streak artefacts typically encountered in direct integration of 1D differential phase images.

The quantitative accuracy of the technique was then demonstrated by comparing the differential and integrated phase profiles of a PMMA cylinder extracted from the experimental images with their expected theoretical counterparts, which were found to be in agreement. The method also lends itself naturally to more sophisticated dark-field analysis approaches, which enable an extraction of the pixel-wise distributions of a given sample, as recently proposed by Modregger et al [Modregger et al. 2014]; those could be the subject of future investigations.

As can be expected, additional input images are required for the 2D set-up compared to the standard 1D EI set-up in order to retrieve refraction or scattering information in 2D. For 1D-EI, two images are required for refraction and three for scattering, compared to the three and six needed for 2D refraction and scattering retrieval, respectively. One clear disadvantage of acquiring multiple images in separate exposures is an increased chance of errors occurring while positioning the masks and for the sample, as well as increasing exposure time and potentially dose. A single-mask 2D EI set-up would be sufficient to address these concerns, where multiple pixels may be used to simultaneously acquire the number of images required to perform the retrieval, at the cost of a lower spatial resolution. If this was also paired with a high quality detector, such as PixiRad [Delogu et al. 2016; Bellazzini et al. 2013; Vincenzi et al. 2015], as used for the work described in chapter 4, it could lead to a new state-of-the-art implementation, simultaneously benefitting from all the advantages explored in the course of this work.

Chapter 7 Conclusion and future work

The work presented in this thesis explores further developments of the edge illumination X-ray phase contrast imaging technique, and can be seen as a preliminary step to translating the benefits of phase contrast imaging to mainstream and industrial applications. To realise this goal, a phase contrast imaging method must be robust, fast and easy to implement, while simultaneously providing a clear improvement on current technology.

In this chapter, a summary of the steps taken to develop the EI method towards this goal are presented. Finally, suggestions are made regarding the future research directions that should be explored in order to further improve and integrate the results obtained in this thesis.

7.1 Conclusion

Phase contrast imaging methods provide a means of improving the quality of X-ray images. Numerous phase contrast techniques have been developed to detect refraction signals, and capitalise on the potential increase in contrast provided by this modality. However, in the past, these often relied on the use of highly stable set-ups and cutting-edge facilities. In recent years, greater research interest has been directed towards the development of phase contrast techniques that can be translated from the laboratory/research environment to mainstream use. Efforts have been made to speed up the image acquisition process, minimise the dose received by the sample, and to develop novel analysis methods capable of providing more relevant information to investigators.

A brief historical review of phase contrast imaging methods was first undertaken, following which, the edge illumination method was introduced. EI XPCI is a promising candidate for translation into mainstream applications thanks to its numerous advantages. Experiments were carried out to study and optimise the sensitivity, acquisition time/dose to the sample, and to develop novel implementations of the EI method.

7.1.1 Edge Illumination Sensitivity

Detailed descriptions were provided of the EI set-up, its physical principles and imaging procedures. The illumination curve, which is analogous to the rocking curve in ABI, was introduced as a means of characterising the EI system. Additionally, a phase retrieval algorithm was presented, the analysis of which enables predictions of the sensitivity of a set-up given the IC gradient and the image noise.

An experiment was performed, using a polychromatic source, aimed at studying the sensitivity of the set-up as a function of the position on the IC where images are acquired. The first test was carried out by acquiring all images with the same exposure time, which meant that the acquired statistics was different depending on the point at which these were collected on the IC. A sapphire wire was used as a sample to test the quantitative accuracy of the phase retrieval algorithm at different IC points. The standard deviation in the background of each differential phase image was measured in order to determine the minimum resolvable refraction angle. Finally, through this analysis, the optimal imaging position on the IC was found to be the one corresponding to an illuminated pixel fraction of 25%. Here the sensitivity was highest, i.e. the error on the refraction angle was lowest.

A second measurement of the sensitivity was then performed for images acquired at different IC points, but with matching statistics. Also, in this case, the best sensitivity was obtained at 25% illuminated pixel fraction. This confirmed the prediction of the analytical model, namely that refraction sensitivity is highest at the slopes of the IC. Similar conclusions were reached by previous studies performed in ABI.

7.1.2 Single-mask Edge Illumination

The standard, double-mask EI set-up has many advantages; however, for refraction and absorption retrieval, two images need to be acquired. With the standard set-up, this requires two separate exposures, in-between which the masks are moved, thus increasing the susceptibility to positional errors between the acquisitions. Therefore, a new set-up was built to address this potential disadvantage. The single-mask EI set-up eliminates the detector mask of the standard EI set-up, and uses the detector pixels to directly sense refraction-induced beam displacements. This allows the realisation of a single-shot EI set-up, capable of simultaneously acquiring two mixed intensity images. This new method also relaxes the alignment constraints placed on the EI method, and can reduce the acquisition time/dose given to the sample.

An experiment was performed to test the standard EI set-up against the new single-mask implementation. A wave optics simulation was modified to accurately model the experimental set-ups, and benchmarked to ensure that it could accurately reproduce the effects due to the various parameters of the systems. One strongly and one weakly refracting and absorbing wire were then selected, and used to compare their experimentally measured mixed-intensity profiles to those predicted by the simulation. A good agreement was found confirming the quantitative accuracy and reliability of the simulation.

The simulation was also used to predict the sensitivity of the two set-ups, and also in this case a good agreement was found between experimentally measured and simulated values. This is a direct consequence of matching the ICs, and the level of noise found in the image. The sensitivity for the standard set-up was $280 \pm 10\, nrad$, while it was $350 \pm 10\, nrad$ for the single-mask set-up. The standard set-up possesses a higher sensitivity than the SM-EI set-up because of the advantages provided by the detector mask, which redefines the pixel response function of the set-up, making it sharper and to a good extent independent from the detector used. For SM-EI, the sensitivity is directly related to the detector pixel response function. Since typically this is not perfectly sharp, the IC adopts a gentler slope which translates to a worse sensitivity.

The demonstrated reliability of the simulation model enabled estimating the sensitivity of the SM-EI set-up for various detector PSFs. This confirmed that the sensitivity of a standard EI set-up is independent from the detector PSF, and that the SM-EI set-up becomes more sensitive to refraction angles as the PSF of the used detector becomes sharper. For a “perfectly sharp” PSF, the doubled number of photons impinging on the detector would lead to an improved sensitivity by a factor of $\sqrt{2}$. While this may be difficult to obtain in practice, it highlights the presence of a “crossover” point which could be reached if a detector with a sufficiently sharp PSF becomes available.

The retrieved refraction profiles were also compared against the theoretically calculated ones, and a good agreement was obtained for both set-ups. However, reduced thicknesses of the mask septa were used in the SM-EI set-up, which made it more susceptible to beam hardening. This required the use of different spectra to calculate the theoretical profiles acquired with the two set-ups. The excessively thin pre-sample mask septa were shown to have a negative effect on the quantitative accuracy of the retrieved SM-EI profile for the more absorbing samples. This was particularly apparent when phase retrieved profiles obtained from measurements made with the two methods were compared against each other. The simulation was used to validate the assumptions that the thin sample mask was the source of the errors in the retrieval, and to demonstrate that this can be mitigated in future experiments by using a thicker mask. Indeed, in the simulated case of thick masks, both EI configurations produced identical results, also matching their theoretical differential phase profiles.

It was shown that SM-EI can be a viable alternative to the standard EI set-up. Indeed, the simulation predicts that, even with thin masks, for a slope of the detector PSF defined by $\sigma_{PSF} \leq 5\,\mu m$ (see chapter 5), the sensitivity for SM-EI would be better than the one obtained with the standard set-up. A system realised using this specifications and paired with a thicker mask, would present clear advantages over the current EI set-up, thanks to its increased simplicity and insensitivity against misalignments.

7.1.3 2D Edge Illumination

A new laboratory EI set-up, which is capable of resolving refraction and scattering signals in two directions using a conventional X-ray source, was implemented. The 2D EI set-up was realised using two masks with L-shaped apertures, and was initially modelled using a Monte Carlo ray-tracing simulation package. This model was also used to predict the shape of the IC for the unusual L-shaped apertures, which was then used to benchmark the experimental measurement. A study of the alignment of the set-up was undertaken and was used to optimise and inform the corresponding experimental procedure. Despite the increase in exposure time, this set-up can offer additional advantages, by virtue of its two-directional sensitivity, compared to the 1D set-up. For example, it provides an easy way of performing phase retrieval, while mitigating streak artefacts, which typically occur in the 1D integration of a single refraction image.

Simultaneously, a novel phase retrieval algorithm was developed; it requires at least three images for refraction retrieval, and six for scattering retrieval, though the latter may possibly be reduced to five. The approach demonstrated its quantitative accuracy by matching both the differential and integrated phase profiles of a PMMA cylinder, calculated from the experiment, with the theoretical ones. The retrieval algorithm was also tested by acquiring images of a pair of crossed wooden splints, and obtaining the 2D scattering signal from this sample.

7.2 Future Work

Elements of the work which have been presented here can be combined to realise a 2D single-mask EI set-up. By intercepting each beam created by the single mask with more than one pixel, and using “centre of gravity” type approaches, the displacements of the beams may be calculated and translated into phase variations.

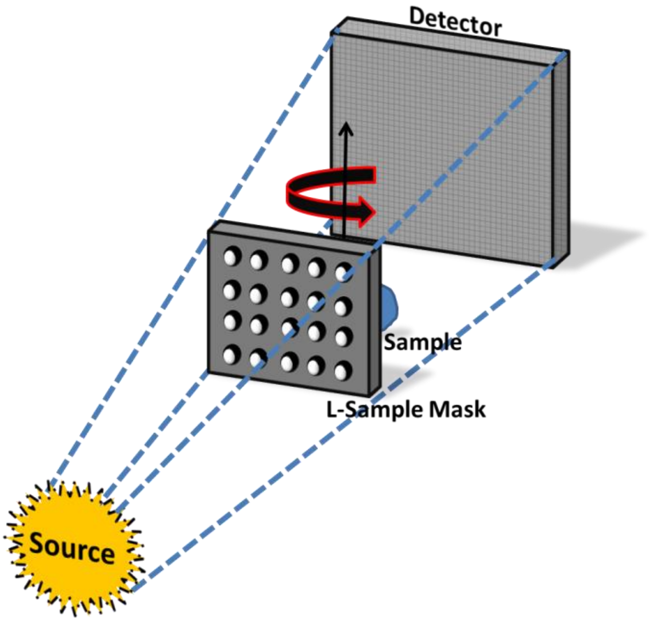

Figure 7-1 A possible implementation of a single-mask 2D-EI CT set-up.

This would constitute a new-generation, fast, robust, and cost-effective lab-based set-up, which may be extended to X-ray Phase Contrast Imaging Computed Tomography, thereby making the method applicable to a wider range of “real world” applications.

When EI was first invented, non-ideal detectors and costly mask manufacturing were two limiting factors imposed on early designs and implementations. Recent advances in the manufacturing process allow for the fabrication of much thicker masks, which can be highly absorbing at high X-ray energies, and extend over larger fields of view, through a much more cost effective process than previously used. If combined with a state-of-the-art photon counting detector with a sharp PSF such as Pixirad, and an appropriate aperture design, the system would possess numerous advantages over the current ones (see Figure 7-1).

Combining single-mask 2D EI, direct detection technology and innovative mask manufacturing approaches in a new system could significantly reduce the alignment requirements of the set-up, while enabling single-shot phase retrieval in two directions. Indeed phase integration is crucial both to CT reconstruction and to ensure that the content within voxels are proportional to the sample electron density.

REFERENCES

J. Als-Nielsen, & D. McMorrow, Elements of Modern X-ray Physics: Second Edition. 2011, *Wiley*

M.R. Arnison, K. G.Larkin, C. J R Sheppard, N. I. Smith, C. J. Cogswell, Linear phase imaging using differential interference contrast microscopy. 2004, *Journal of Microscopy*, 214(1), pp.7–12.

D.Basta, M. Endrizzi, F. A. Vittoria, G. K. N. Kallon, T. P. Millard, P. C. Diemoz, A. Olivo, Note: Design and realization of a portable edge illumination X-ray phase contrast imaging system. 2015, *Review of Scientific Instruments*, 86(9).

R. Bellazzini, G Spandre A. Brez M. Minuti, M Pinchera, P Mozzo, Chromatic X-ray imaging with a fine pitch CdTe sensor coupled to a large area photon counting pixel ASIC. 2013, *Journal of Instrumentation*, 8(2), pp.C02028–C02028.

E. Bergback Knudsen, A. Prodi, J. Baltser, M.Thomsen, P. Kjaer Willendrup, M. Sanchez Del Rio, C. Ferrero, E. Farhi, K. Haldrup, A. Vickery, R. Feidenhans'l, K. Mortensen, M. M. Nielsen, H. F. Poulsen, S. Schmidt, and K. Lefmann, McXtrace: A Monte Carlo software package for simulating X-ray optics, beamlines and experiments. 2013, *Journal of Applied Crystallography*, 46(3), pp.679–696.

U. Bonse & M.Hart, An X-ray interferometer. 1965, *Applied Physics Letters*, 6(8), pp.155–156.

J.M. Boone, T.R. Fewell, & R.J. Jennings, Molybdenum, rhodium, and tungsten anode spectral models using interpolating polynomials with application to mammography. 1997, *Medical physics*, 24(12), pp.1863–1874.

A. Bravin, P. Coan, & P. Suortti, X-ray phase-contrast imaging: from pre-clinical applications towards clinics. 2013, *Physics in medicine and biology*, 58(1), pp.R1-35.

E.Castelli, M. Tonutti, F. Arfelli, R. Longo, E. Quaia, L. Rigon, D. Sanabor, F. Zanconati, D. Dreossi, A. Abrami, E. Quai, P. Bregant, K. Casarin, V.Chenda, R. H. Menk, T. Rokvic, A. Vascotto, G. Tromba, and M. A. Cova, Mammography with synchrotron radiation: first clinical experience with phase-detection technique. 2011, *Radiology*, 259(3), pp.684–694.

D. Chapman, W. Thomlinson, R. E. Johnston, D. Washburn, E. Pisano, N. Gmur, Z. Zhong, R. Menk, F. Arfelli, and D. Sayers, Diffraction enhanced x-ray imaging. 1997, *Physics in medicine and biology*, 42(11), pp.2015–2025.

C. David, B. Nöhammer, H. H. Solak, E.Ziegler, Differential x-ray phase contrast imaging using a shearing interferometer. 2002, *Applied Physics Letters*, 81(17), pp.3287–3289.

P. Delogu, P. Oliva, R. Bellazzini, A. Brez, P.L. de Ruvo, M.Minuti, M. Pinchera, G.Spandre, A.Vincenzi, Characterization of Pixirad-1 photon counting detector for X-ray imaging. 2016, *Journal of Instrumentation*, 11(1), pp.P01015–P01015.

P.C. Diemoz, C. K. Hagen, M. Endrizzi, A. Olivo, Sensitivity of laboratory based implementations of edge illumination X-ray phase-contrast imaging. 2013a, *Applied Physics Letters*, 103(24), pp.24–29.

P.C. Diemoz, F.A.Vittoria, C.K. Hagen, M.Endrizzi, P. Coan, E. Brun, U. H. Wagner, C. Rau, I. K. Robinson, A. Bravin, A. Olivo, Single-image phase retrieval using an edge illumination X-ray phase-contrast imaging setup. 2015, *Journal of Synchrotron Radiation*, 22(4), pp.1072–1077.

P.C. Diemoz, M. Endrizzi, P. Coan, X-ray phase-contrast imaging with nanoradian angular resolution. *Physical Review Letters*, 2013b, 110(13), pp.1–5.

P.C. Diemoz, A. Bravin, & P.Coan, Theoretical comparison of three X-ray phase-contrast imaging techniques : imaging and grating interferometry. 2012, *Optics Express*, 20(3), pp.2789–2805.

P.C. Diemoz, & A. Olivo, On the origin of contrast in edge illumination X-ray phase-contrast imaging. 2014, *Optics express*,22(23), pp.28199–28214.

P.C. Diemoz, F.A. Vittoria, & A.Olivo, Spatial resolution of edge illumination X-ray phase-contrast imaging. 2014, *Optics express*, 22(13), pp.15514–29.

M. Endrizzi, F.A. Vittoria, G. Kallon, D. Basta, P.C. Diemoz, A. Vincenzi, P. Delogu, R. Bellazzini, A. Olivo, Achromatic approach to phase-based multi-modal imaging with conventional X-ray sources. 2015a, *Optics Express*, 23(12), p.16473.

M. Endrizzi, P.C. Diemoz, T.P. Millard, J. Louise Jones, R.D. Speller, I.K. Robinson, A. Olivo,. Hard X-ray dark-field imaging with incoherent sample illumination. 2014, *Applied Physics Letters*, 104(2), pp.1–4.

M. Endrizzi, D. Basta, & A. Olivo, Laboratory-based X-ray phase-contrast imaging with misaligned optical elements. 2015b, *Applied Physics Letters* 107(12), pp.10–15.

R.P. Feynmann, R. Leighton & M. Sands, The Feynmann Lectures. 1964, *Addison-Wesley*. Available at: http://www.feynmanlectures.caltech.edu/.

D. Gabor, A new microscopic principle. 1948, *Nature*, 161(4098), pp.777–778.

A. Haase, G. Landwehr, & E. Umbach, Röntgen Centennial: X-rays in Natural and Life Sciences. 1997, *World Scientific Publishing Company*

C.K. Hagen, P.C. Diemoz, M. Endrizzi, A. Olivo, The effect of the spatial sampling rate on quantitative phase information extracted from planar and tomographic edge illumination x-ray phase contrast images. 2014, *Journal of Physics D: Applied Physics*, 47(45), p.455401.

K. Ignatyev, P.R.T. Munro, D. Chana, R.D. Speller, A. Olivo, Effects of signal diffusion on x-ray phase contrast images. 2011, *Review of Scientific Instruments*, 82(7).

C. Kottler, C. David, F. Pfeiffer, O. Bunk, A two-directional approach for grating based differential phase contrast imaging using hard x-rays. 2007, *Optics express*, 15(3), pp.1175–1181.

H.A. Kramers,. La diffusion de la lumière par les atomes. 1927, *Atti del Congresso Internationale Fisici*, 2, p.545.

R. de L, Kronig, The theory of dispersion of x-rays. 1926, *Journal of the Optical Society of America*, 12(6), pp.547–557.

M. Langer, P.Cloetens, & F. Peyrin, Regularization of phase retrieval with phase-attenuation duality prior for 3-D holotomography. 2010, *IEEE Transactions on Image Processing*, 19(9), pp.2428–2436.

H. Miao, L. Chen, E.E. Bennett, N.M. Adamo, A.A. Gomella, A. M DeLuca, A. Patel, N.Y. Morgan, H. Wen, Motionless phase stepping in X-ray phase contrast imaging with a compact source. 2013, *Proceedings of the National Academy of Sciences of the United States of America*, 110(48), pp.19268–72.

T.P. Millard, M. Endrizzi, K. Ignatyev, C.K. Hagen, P.R.T. Munro, R.D. Speller, A. Olivo, Method for automatization of the alignment of a laboratory based x-ray phase contrast edge illumination system. 2013, *Review of Scientific Instruments*, 84(8).

T.P. Millard, M. Endrizzi, P.C. Diemoz, C.K. Hagen, A. Olivo, Monte Carlo model of a polychromatic laboratory based edge illumination x-ray phase contrast system. 2014, *Review of Scientific Instruments*, 85(5), p.53702.

T.P. Millard, Microbubbles as a quantitative contrast agent for x-ray phase contrast imaging. 2015, Doctoral thesis, *UCL (University College London)*.

P. Modregger, S. Rutishauser, J. Meiser, C. David, M. Stampanoni, Sensitivity of X-ray grating interferometry. 2011, *Optics express*, 19(19), pp.18324–38.

P. Modregger, S. Rutishauser, J. Meiser, C. David, M. Stampanoni, Two-dimensional ultra-small angle X-ray scattering with grating interferometry. 2014, *Applied Physics Letters*, 105(2).

A. Momose, S. Kawamoto, I.Koyama, Y. Hamaishi, K.Takai, Y. Suzuki, Demonstration of x-ray Talbot interferometry. 2003, *Japanese Journal of Applied Physics, Part 2: Letters*, 42(7 B).

A. Momose, T. Takeda, Y. Itai, K. Hirano, Phase-contrast X-ray computed tomography for observing biological soft tissues. 1996, *Nature medicine*, 2(4), pp.473–475.

A. Momose, Phase-sensitive imaging and phase tomography using X-ray interferometers. 2003, *Optics express*, 11(19), pp.2303–2314.

P. Munro, K. Ignatyev, R.D. Speller, A. Olivo, Design of a novel phase contrast X-ray imaging system for mammography. 2011 , *Physics in medicine and biology*, 55(14), pp.4169–4185.

P.R.T. Munro, C. K. Hagen, M. B. Szafraniec, and A.Olivo, A simplified approach to quantitative coded aperture X-ray phase imaging. 2013, *Optics Express*, 21(9), pp.11187–11201.

P.R.T. Munro, K. Ignatyev, R. D. Speller, and A. Olivo, Phase and absorption retrieval using incoherent X-ray sources. 2012, *Proceedings of the National Academy of Sciences*, 109(35), pp.13922–13927.

P.R.T. Munro, K. Ignatyev, R. D. Speller, and A. Olivo, The relationship between wave and geometrical optics models of coded aperture type x-ray phase contrast imaging systems. 2010, *Optics express*, 18(5), pp.4103–4117.

P.R.T. Munro, & A. Olivo, X-ray phase-contrast imaging with polychromatic sources and the concept of effective energy. 2013, *Physical Review A - Atomic, Molecular, and Optical Physics*, 87(5).

K. Nagai, A phase demodulation method for two-dimensional grating-based X-ray interferometry. 2014, *Philosophical Transactions of the Royal Society A: Mathematical, Physical and Engineering Sciences*, 372:20130034.

A. Olivo, S. E. Bohndiek, J. A. Griffiths, A. Konstantinidis, and R. D. Speller., A non-free-space propagation x-ray phase contrast imaging method sensitive to phase effects in two directions simultaneously. 2009, *Applied Physics Letters*, 94(4).

A. Olivo, F. Arfelli, G. Cantatore, R. Longo, R. H. Menk, S. Pani, M. Prest, P. Poropat, L. Rigon, G. Tromba, E. Vallazza, and E. Castelli, An innovative digital imaging set-up allowing a low-dose approach to phase contrast applications in the medical field. 2001, *Medical physics*, 28(8), pp.1610–1619.

A. Olivo, S. Gkoumas, M. Endrizzi, C.K. Hagen, M.B. Szafraniec, P.C. Diemoz, P.R.T. Munro, K. Ignatyev, B. Johnson, J. A. Horrocks, S.J. Vinnicombe, J.L. Jones, R.D. Speller, Low-dose phase contrast mammography with conventional x-ray sources. 2013, *Medical Physics*, 40(9), p.90701.

A. Olivo, & R. Speller, Experimental validation of a simple model capable of predicting the phase contrast imaging capabilities of any x-ray imaging system. 2006, *Physics in medicine and biology*, 51(12), pp.3015–3030.

A. Olivo, & R. Speller, Modelling of a novel x-ray phase contrast imaging technique based on coded apertures. 2007, *Physics in medicine and biology*, 52(22), pp.6555–6573.

O. Oltulu, Z. Zhong, M.Hasnah, M.N. Wernick, D. Chapman, Extraction of extinction, refraction and absorption properties in diffraction enhanced imaging. 2003, *Journal of Physics D: Applied Physics*, 36(17), pp.2152–2156.

Paganin, D, S.C. Mayo, T.E. Gureyev, P.R. Miller, S.W. Wilkins, Simultaneous phase and amplitude extraction from a single defocused image of a homogeneous object. 2002, *Journal of Microscopy*, 206(1), pp.33–40.

E. Pagot, P. Cloetens,S. Fiedler, A. Bravin, P. Coan, J. Baruchel, J. Härtwig, W. Thomlinson, A method to extract quantitative information in analyzer-based x-ray phase contrast imaging. 2003, *Applied Physics Letters*, 82(20), pp.3421–3423.

Peatross, J. & Ware, M., 2012. *Physics of light and Optics*, Brigham Young University. Available at: http://optics.byu.edu/BYUOpticsBook_2013.pdf.

Pelliccia, D. L. Rigon, F. Arfelli, R.H. Menk, I. Bukreeva, A. Cedola, A three-image algorithm for hard x-ray grating interferometry. 2013, *Optics express*, 21(16), pp.19401–11.

A. Peterzol, A. Olivo, L. Rigon, S. Pani, D. Dreossi, The effects of the imaging system on the validity limits of the ray-optical approach to phase contrast imaging. 2005, *Medical physics*, 32(12), pp.3617–3627.

F. Pfeiffer, T. Weitkamp, O. Bunk, C. David, Phase retrieval and differential phase-contrast imaging with low-brilliance X-ray sources. 2006, *Nature Physics*, 2(4), pp.258–261.

L. Rigon, H. Besch, F. Arfelli, R.H. Menk, G. Heitner, H. Plothow-Besch, A new DEI algorithm capable of investigating sub-pixel structures. 2003, *Journal of Physics D: Applied Physics*, 36(10A), pp.A107–A112.

L. Rigon, F. Arfelli, & R.H. Menk, Generalized diffraction enhanced imaging to retrieve absorption, refraction and scattering effects. 2007, *Journal of Physics D: Applied Physics*, 40(10), pp.3077–3089.

W.C. Röntgen, 1896. On a New Kind of Rays, *American Association for the Advancement of Science* 3(59), pp.227–231.

G. Sato, T. Kondoh, H. Itoh, S. Handa, K. Yamaguchi, T. Nakamura, K. Nagai, C. Ouchi, T. Teshima, Y. Setomoto, T. Den, Two-dimensional gratings-based phase-contrast imaging using a conventional x-ray tube. 2011, *Optics letters*, 36(18), pp.3551–3.

K. Scherer, L. Birnbacher, M. Chabior, J. Herzen, D. Mayr, S. Grandl, A. Sztrókay-Gaul, K. Hellerhoff, F. Bamberg, F. Pfeiffer, Bi-directional x-ray phase-contrast mammography. 2014, *PloS one*, 9(5), p.e93502.

A. Snigirev, I. Snigireva, V. Kohn, S. Kuznetsov, I. Schelokov, On the possibilities of x-ray phase contrast microimaging by coherent high-energy synchrotron radiation. 1995, *Review of Scientific Instruments*, 66(12), pp.5486–5492.

H.F. Talbot, LXXVI. Facts relating to optical science. 1836, No. IV. *Philosophical Magazine Series 3*, 9(56), pp.401–407. Available at: http://www.tandfonline.com/doi/abs/10.1080/14786443608649032.

A. Vincenzi, P.L. de Ruvo, P. Delogu, R. Bellazzini, A. Brez, M. Minuti, M. Pinchera,G. Spandre, Energy characterization of Pixirad-1 photon counting detector system. 2015, *Journal of Instrumentation*, 10(4), pp.C04010–C04010.

F.A. Vittoria, M. Endrizzi, P.C. Diemoz, A. Zamir, U.H. Wagner, C. Rau, I. K. Robinson, A. Olivo, X -ray absorption, phase and dark -field tomography through a beam tracking approach. 2015b, *Scientific Reports*, 5:16318.

F.A. Vittoria, P.C. Diemoz, M. Endrizzi, L. Rigon, F.C. Lopez, D. Dreossi, P.R.T. Munro, A. Olivo, Strategies for efficient and fast wave optics simulation of coded-aperture and other x-ray phase-contrast imaging methods, 2013, *Applied optics*, 52(28), pp.6940–6947.

F.A. Vittoria, G.K.N. Kallon, D. Basta, P.C. Diemoz, I.K. Robinson, A. Olivo, M. Endrizzi, Beam tracking approach for single-shot retrieval of absorption, refraction, and dark-field signals with laboratory x-ray sources. 2015a, *Applied Physics Letters*, 106(22), p.224102.

Washburn, D.B. & Johnston, R.E., Christensen's Physics of Diagnostic Radiology, 4th Edition. 1991, *Lea and Febiger*

H.H. Wen, E.E. Bennett, R. Kopace, A. F. Stein, V. Pai, Single-shot x-ray differential phase-contrast and diffraction imaging using two-dimensional transmission gratings. 2010, *Optics letters*, 35(12), pp.1932–1934.

M.N. Wernick, O. Wirjadi, D. Chapman, Z., Zhong N.P. Galatsanos, Y. Yang, J.G. Brankov, O. Oltulu, M.A. Anastasio, C. Muehleman, Multiple-image radiography. 2003, *Physics in medicine and biology*, 48(23), pp.3875–3895.

S.W. Wilkins, T.E. Gureyev, D. Gao, A. Pogany, A.W. Stevenson, Phase-contrast imaging using polychromatic hard X-rays. 1996, *Nature*, 384(6607), pp.335–338.

I. Zanette, T. Zhou, A. Burvall, U. Lundström, D. H. Larsson, M. Zdora, P. Thibault, F. Pfeiffer, H. M. Hertz, Speckle-based x-ray phase-contrast and dark-field imaging with a laboratory source. 2014, *Physical Review Letters*, 112(25), pp.1–5.

I. Zanette, T. Weitkamp, T. Donath, S. Rutishauser, C. David, Two-dimensional X-ray grating interferometer. 2010, *Physical Review Letters*, 105(24), pp.2–5.

F. Zernike, Phase contrast, a new method for the microscopic observation of transparent objects part II. 1942, *Physica*, 9(10), pp.974–986.

F. Zernike, How I discovered Phase Contrast.1955, *Advancement Of Science*, 121(3141), pp.345–349.